0830-L-02

NAS1.29/3-2:98-02

NASA Tech Briefs

National Aeronautics and
Space Administration

Electronic Components and Circuits

Electronic Systems

Physical Sciences

Materials

Computer Programs

Mechanics

Machinery

Fabrication Technology

Mathematics and Information Sciences

Life Sciences

98-02

COMPLETED

February 1998

NE 98-034707

INTRODUCTION

Tech Briefs are short announcements of new technology derived from the research and development activities of the National Aeronautics and Space Administration. These Briefs emphasize information considered likely to be transferable across industrial, regional, or disciplinary lines and are issued to encourage commercial application.

Availability of NASA Tech Briefs and TSP's

Distribution of NASA Tech Briefs, a monthly periodical publication, is limited to engineers in U.S. Industry and to other domestic technology transfer agents. Requests for individual Tech Briefs or for Technical Support Packages (TSP's) announced herein should be addressed to

NASA Center for AeroSpace Information
Technology Transfer Office
800 Elkridge Landing Rd.
Linthicum Heights, MD 21090-2934
Telephone No. (301) 621-0245

Please reference the three-letter, five-digit control number located at the end of each Tech Brief. Information on NASA's Technology Utilization Program, its documents, and services is also available at the same facility.

Technology Utilization Officers and Patent Counsels are located at NASA field installations to provide technology-transfer access to industrial users. Inquiries can be made by writing to NASA field installations listed below.

Technology Utilization Officers and Patent Counsels

Ames Research Center
Technology Utilization Officer
Mail Code 223-3
Moffett Field, CA 94035

Patent Counsel
Mail Code 200-11
Moffett Field, CA 94035

Goddard Space Flight Center
Technology Utilization Officer
Mail Code 702-1
Greenbelt, MD 20771

Patent Counsel
Mail Code 204
Greenbelt, MD 20771

Lyndon B. Johnson Space Center
Technology Utilization Officer
Mail Code IC-4
Houston, TX 77058

Patent Counsel
Mail Code AL3
Houston, TX 77058

John F. Kennedy Space Center
Technology Utilization Officer
Mail Stop PT-PMO-A
Kennedy Space Center, FL 32899

Patent Counsel
Mail Code PT-PAT
Kennedy Space Center, FL 32899

Langley Research Center
Technology Utilization Officer
Mail Stop 143
Hampton, VA 23665

Patent Counsel
Mail Code 279
Hampton, VA 23665

Lewis Research Center
Technology Utilization Officer
Mail Stop 7-3
21000 Brookpark Road
Cleveland, OH 44135

Patent Counsel
Mail Code LE-LAW
21000 Brookpark Road
Cleveland, OH 44135

Jet Propulsion Laboratory
Technology Utilization Officer
Mail Stop 156-211
4800 Oak Grove Drive
Pasadena, CA 91109

NASA Resident Office-JPL
Technology Utilization Officer
Mail Stop 180-801
4800 Oak Grove Drive
Pasadena, CA 91109

Patent Counsel
Mail Code 180-801
4800 Oak Grove Drive
Pasadena, CA 91109

George C. Marshall Space Flight Center
Technology Utilization Officer
Code AT01
Marshall Space Flight Center, AL 35812

Patent Counsel
Mail Code CC01
Marshall Space Flight Center, AL 35812

John C. Stennis Space Center
Technology Utilization Officer
Code HA-20
Stennis Space Center, MS 39529

NASA Headquarters
Technology Utilization Officer
Code CU
Washington, DC 20546

Assistant General Counsel for Patent Matters
Code GP
Washington, DC 20546

Dryden Flight Research Center
Technology Utilization Officer
M/S D21-31
Bldg. 4832 Whse 7
Lilly Dr.
Edwards, CA 93523

NASA Tech Briefs

National Aeronautics and Space Administration

February 1998
98-02

5 Electronic Components and Circuits

13 Electronic Systems

19 Physical Sciences

31 Materials

37 Computer Programs

41 Mechanics

47 Machinery

51 Mathematics and Information Sciences

59 Life Sciences

This document was prepared under the sponsorship of the National Aeronautics and Space Administration. Neither the United States Government nor any person acting on behalf of the United States Government assumes any liability resulting from the use of the information contained in this document, or warrants that such use will be free from privately owned rights.

BLANK PAGE

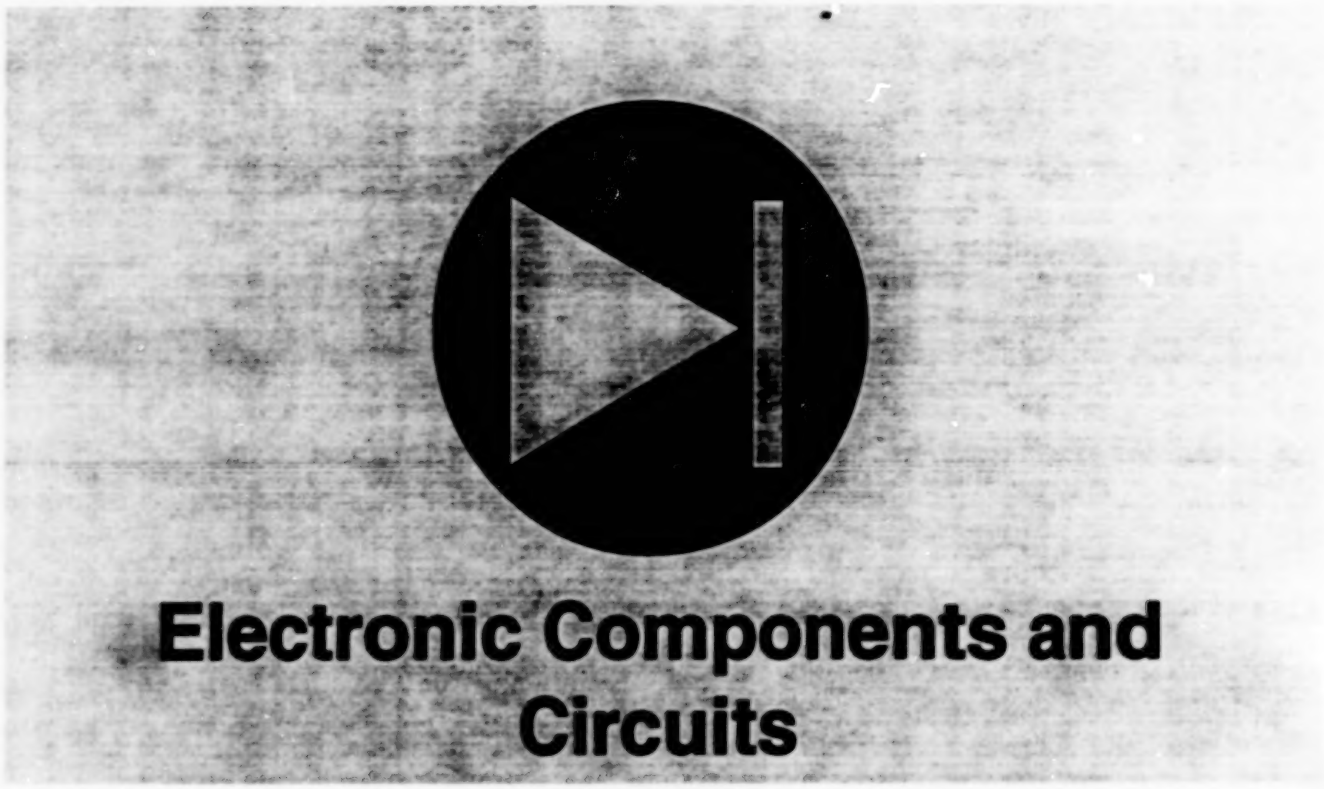

Electronic Components and Circuits

Hardware, Techniques, and Processes

7 Antiovershoot Position Control for Motors Run at Full Speed
8 Coplanar-Stripline Transition and Band-Stop Filters
9 Fabricating Diffusion-Cooled Hot-Electron-Bolometer Elements
10 Hybrid Superconductor/Semiconductor Planar Oscillators

BLANK PAGE

Antiovershoot Position Control for Motors Run at Full Speed

Innovative position controller allows the desired position damping to be reached while the motor is running at full speed.

Marshall Space Flight Center, Alabama

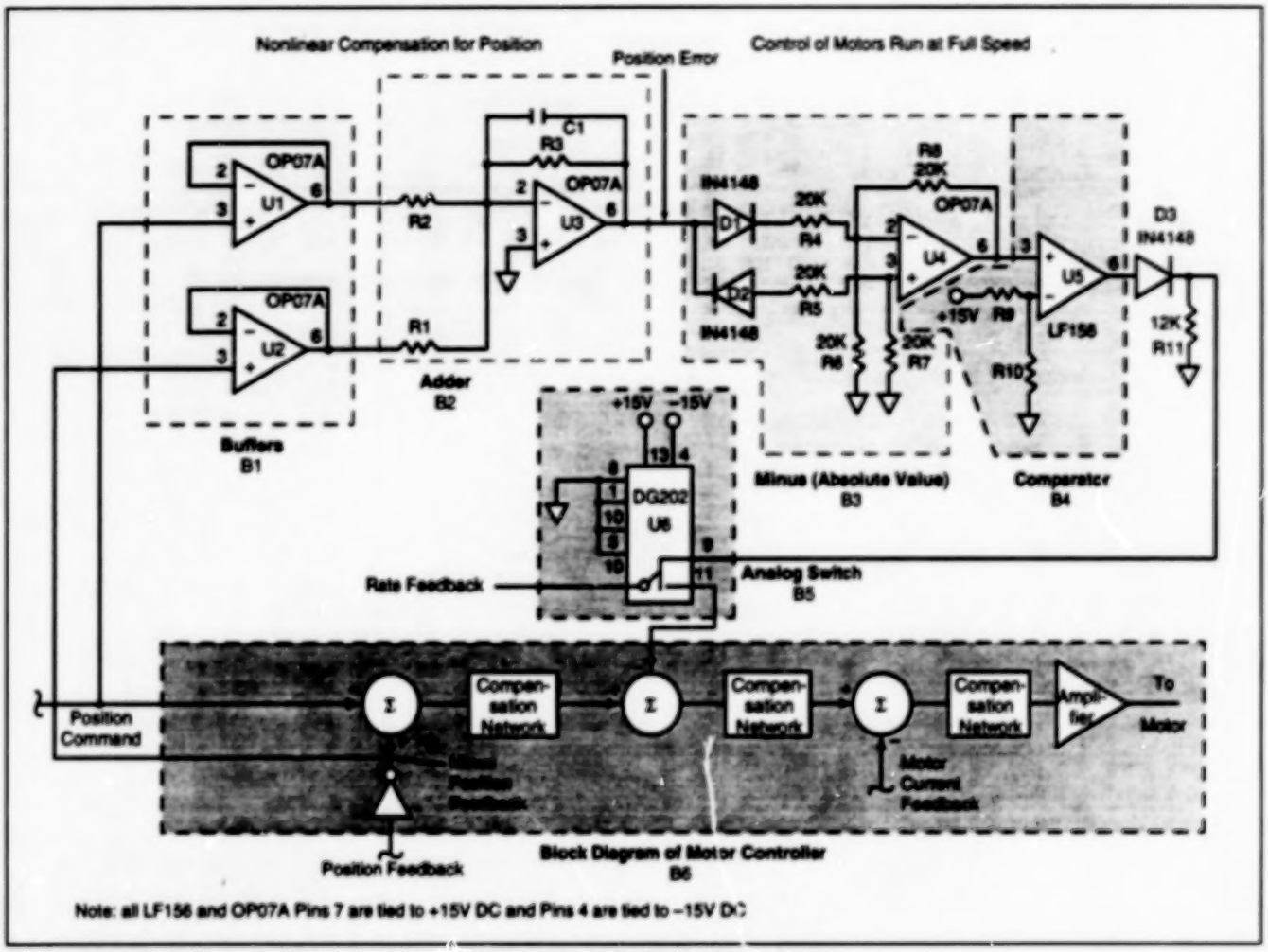

The Improved Motor Controller allows a motor to run at full speed until the final position gets close.

An improved motor controller provides a circuit that will allow a motor to run at full speed while traveling from point A to point B, and still be able to obtain the desired damping coefficient when reaching point B. Previously, a motor would overshoot its desired stopping point when running at full speed, especially in high-inertia systems. Some form of rate feedback, or lead compensation, was required to stabilize a position loop, but the motor would not run at full speed while traveling from point A to point B.

The innovators recognized this problem while working on the Electromechanical Actuator Advanced Development Program at Marshall Space Flight Center. Consequently, they developed a nonlinear motor controller that will allow the motor to obtain both the desired motor speed rate and the desired damping coefficient when reaching point B.

This motor controller concentrates on the position error of the system. Buffers are used to tie in the position command and position feedback points of the system with a high impedance input. An adder circuit simply adds the position command to the negative position feedback. The output of the adder circuit is a signal proportional to the position error.

Depending on the amplitude of the position error, the controller will take the rate feedback of the system out of the system control loop, or it will sum it into the system control loop. If the position error is too large in the comparator block, the rate feedback will be removed from the control loop. If the position error is too small, the rate feedback will be added to the system control loop. In order to achieve this, the position error is fed into a minus absolute-value circuit. This will allow the invention to work whether the position error sign is plus or minus.

The minus absolute value of the position error is then compared, using the circuit in the comparator block, to a user definable set point. This set point allows the user to select at what point the rate will be summed into the system control loop. By selecting the set point, the user determines how long the motor can run at full speed as the position mechanism travels from a given point to another commanded point. Also, by selecting the set point, the user determines when the rate will be summed into the system controller to add damping to the system control loop.

A discrete signal from the comparator block toggles between a plus and minus voltage. The diode and resistor condition the output signal of the comparator block so that it will only go from zero to a plus voltage. This signal then controls the ana-

log switch, which actually does the switching in and out of the rate feedback to the system controller.

The end result is a circuit that allows the motor to run at full speed until the final position gets close, as defined by the user. The rate feedback is then summed into the system controller to achieve the desired damping for the position loop.

This work was done by David E. Howard and Justino Montenegro of **Marshall Space Flight Center**. *Further information is contained in a TSP [see page 1].*

Inquiries concerning rights for the commercial use of this invention should be addressed to the Patent Counsel, Marshall Space Flight Center [see page 1]. Refer to MFS-31182.

Coplanar-Stripline Transition and Band-Stop Filters

Advantages include compactness and suitability for incorporation into monolithic microwave integrated circuits.

Lewis Research Center, Cleveland, Ohio

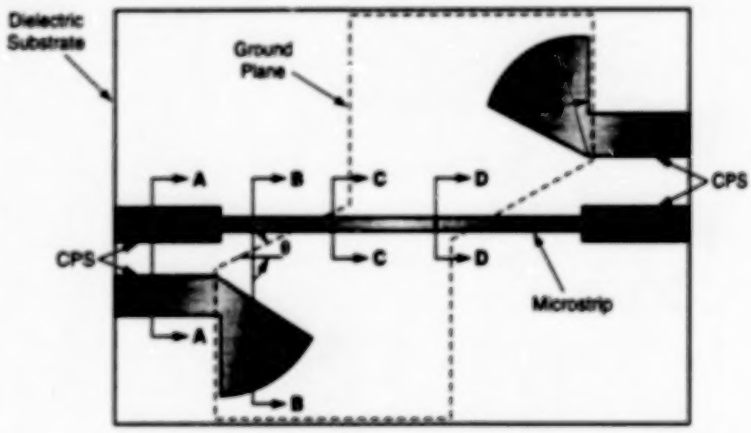

TOP VIEW OF BACK-TO-BACK CPS-TO- MICROSTRIP TRANSITIONS

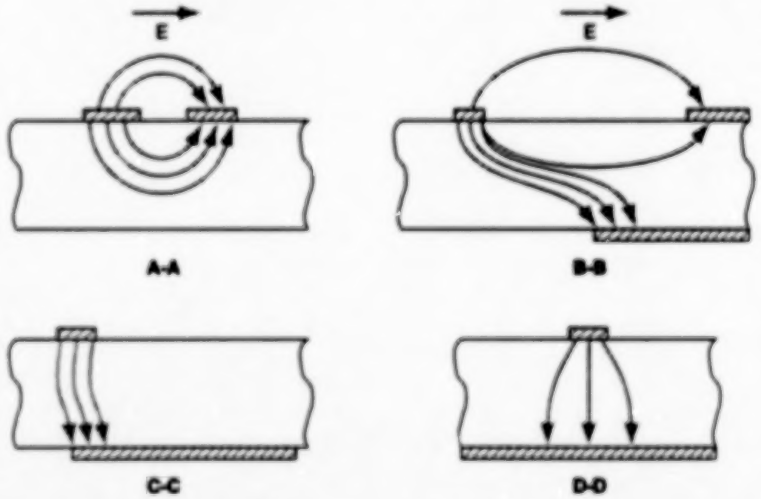

ENLARGED CROSS SECTIONS SHOWING ELECTRIC-FIELD LINES AT FOUR LOCATIONS

Figure 1. Two Back-to-Back CPS-to-Microstrip Transitions serve to couple power from a source to a load. Impedances depend on widths of conductive strips. The resonance frequency depends on *R* and *ϕ*.

Three coplanar-stripline circuits have been designed to perform coupling and filtering functions in microwave systems. These circuits could be incorporated into feed networks for microwave antennas, for example. One of the circuits comprises two back-to-back coplanar-strip-to-microstrip transitions. The other two circuits are coplanar-stripline band-stop filters. The principal advantages of these circuits over others designed to perform the same functions are compactness and suitability for integration into monolithic microwave integrated circuits.

"Coplanar stripline" ("CPS") denotes a transmission line that comprises two adjacent conductive strips on one face of a dielectric substrate. "Microstrip" denotes a transmission line that comprises a conductive strip on one face of a dielectric substrate and a patch much broader than the strip (a ground plane) covering all or at least a large portion of the opposite face of the substrate.

The back-to-back CPS-to-microstrip transitions (see Figure 1) serve to couple power from a source to a load; e.g., from a transmitter to an antenna. Proceeding inward from each end of this circuit, one of the conductive strips of the CPS terminates in a radial stub, while the other strip is extended and narrowed to form the microstrip. The radial stub exhibits a resonance, the frequency of which depends on the radius *R* and angle *ϕ*; at resonance, there is a radio-frequency short circuit between the strip and the ground plane. The characteristic impedances of the CPS and stripline portions of the circuit are matched by suitable choice of the widths of the conductive strips.

In the CPS portion of the circuit, the electric field is oriented across the gap between the strips and roughly parallel to the faces of the dielectric substrate. In the microstrip portion, the electric field is approximately perpendicular to the faces of the substrate. The angle *θ* of the edge of the ground plane provides for rotation of the electric field between the CPS and stripline orientations.

The two band-stop filters are of the spur-slot and spur-strip types (see Figure 2). The spur-slot is a resonant structure within one of two strips; it is convenient to use a spur-slot when *W* is large and *S* is small. At its resonance, the spur-slot can be modeled as a quarter-wavelength short-circuit stub in series with the transmission line. At resonance, the spur-slot thus prevents the flow

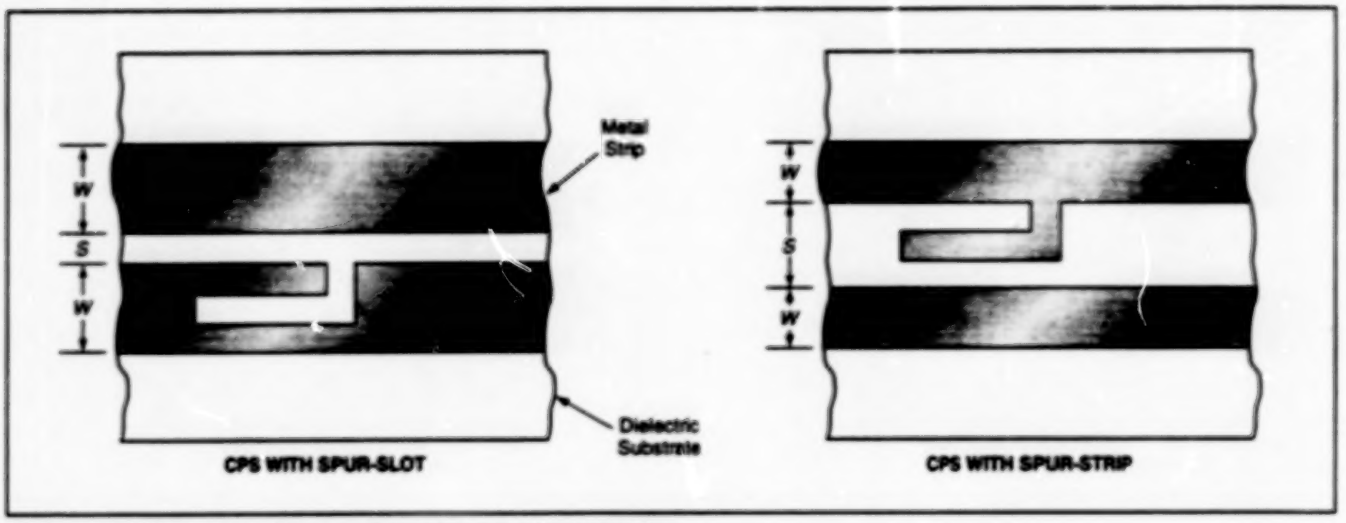

Figure 2. **CPS With a Spur-Slot or a Spur-Strip** acts a band-stop filter.

of power to the load. The spur-strip is a resonant structure between two strips; it is convenient to use a spur-strip when *W* is small and *S* is large. At its resonance, the spur-strip can be modeled as a quarter-wavelength open-circuit stub in parallel with the transmission line. Several spur-slots or spur-strips can be incorporated at intervals of a half wavelength along a transmission line to enhance the band-stop performance.

This work was done by Rainee N. Simons of NYMA, Inc., for **Lewis Research Center**. *Further information is contained in a TSP [see page 1].*

Inquiries concerning rights for the commercial use of this invention should be addressed to NASA Lewis Research Center, Commercial Technology Office, Attn: Tech Brief Patent Status, Mail Stop 7-3, 21000 Brookpark Road, Cleveland, Ohio 44135. Refer to LEW-16335.

Fabricating Diffusion-Cooled Hot-Electron-Bolometer Elements

A key feature is the use of a self-aligned etch mask.

NASA's Jet Propulsion Laboratory, Pasadena, California

Microbridges that constitute the superconducting-transition sensory elements of electron-diffusion-cooled hot-electron bolometers can now be fabricated in increased yield and quality. This improvement is made possible by a fabrication process that notably includes the use of a self-aligned mask during a critical etching step.

Some explanation of the underlying principles is necessary to give meaning to a description of the fabrication process. Electron-diffusion-cooled hot-electron bolometers are undergoing development for use as mixers that could operate at carrier and local-oscillator frequencies in the terahertz range, putting out signals at intermediate frequencies (IFs) in the gigahertz range. The most likely initial applications of such mixers would occur in radio-astronomy receivers. A prototype of the present electron-diffusion-cooled hot-electron bolometers was described in "Diffusion-Cooled Hot-Electron Bolometer Mixer" (NPO-19719), *NASA Tech Briefs*, Vol. 21, No. 1 (January 1997), page 12a.

The microbridge in a device of the present type is made from a film of niobium 10 nm thick. The length and width of the bridge are typically of the order of 100 nm (see Figure 1). The film material and dimensions are chosen to obtain the required superconducting-transition temperature (about 6 K) and to allow electron diffusion to be the dominant cooling mechanism. At the ends of the bridge, the strip of niobium widens into pads that make contact with relatively thick overlying gold pads, which define the length of the bridge and provide both heat sinking and electrical contact to external circuitry.

Figure 1. **A Niobium Microbridge** only 160 nm long by 80 nm wide connects broader niobium pads that lie under the gold contact pads.

Like other microelectronic devices, a device of this type must be fabricated in a lithographic process. The need to ensure that the niobium contact pads extend under the full areas of the gold contact pads can give rise to difficulty in lithographic alignment. The present fabrication process (see Figure 2) was developed to solve this alignment problem.

The devices are fabricated, variously, on quartz or silicon wafers, depending upon the circuits in which they are to be used. The wafers are cleaned with organic solvents, then mounted in a vacuum processing chamber on an aluminum disk that keeps them near room temperature during processing. The chamber is evacuated, the substrates are cleaned by an argon-ion beam, then the substrates are coated with niobium 10 nm thick by magnetron sputtering. Then gold is deposited by thermal evaporation to a thickness of 15 nm to prevent oxidation of the niobium during subsequent processing steps.

In the subsequent steps, device features larger than 1 μm are formed by optical lithography, and the smaller ones by electron-beam lithography. Initially, the gold-coated wafers are optically patterned with alignment marks. Then in preparation for electron-beam lithography using a bilayer-stencil technique, the wafers are coated with two layers of poly(methylmethacrylate) of different molecular weights. The bilayer-stencil technique is used because it provides smoother edges for metal lift-off than does a single-layer technique.

The width of the bridge in each device is defined in the first electron-beam-beam-lithography step. After electron-beam exposure and development, gold is deposited to a thickness of 25 nm. After lift-off, what remains of this deposit are gold mask lines 50 to 200 nm wide and several microns long.

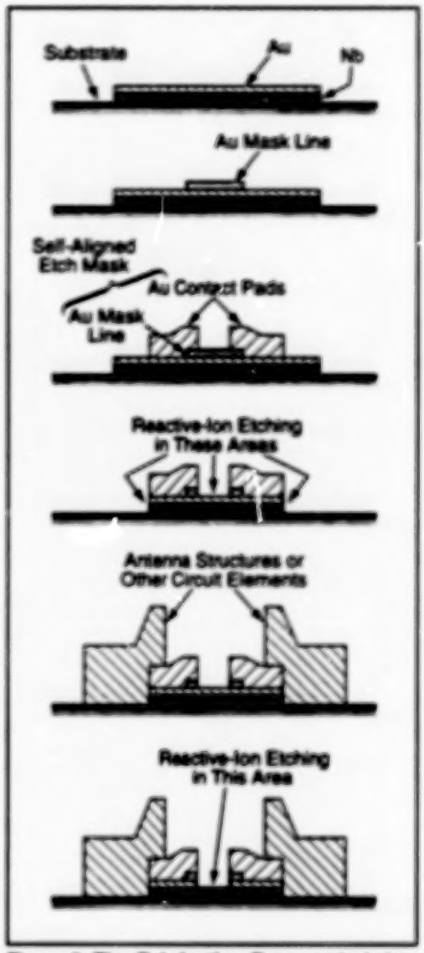

Figure 2. The Fabrication Process includes the use of a self-aligned etch mask to solve an alignment problem.

The width of the bridge is defined in the second electron-beam-lithography step. Two 110-nm-thick gold pads (destined to become the contact pads) separated by a gap 50 to 300 nm long are positioned over the ends of the gold mask line.

The resulting composite of gold pads and the mask line constitutes a self-aligned mask for use in reactive-ion etching to remove the surrounding, unmasked portion of the gold-coated niobium film to form the niobium microbridge while leaving the masked portion of the niobium film intact under the full areas of the gold pads. This etch is performed in a two-step procedure that leaves the niobium microbridge still coated with some gold.

Then by use of a combination of optical and/or electron-beam lithography depending on the specific design, gold antenna structures or other circuit elements are formed in contact with the gold contact pads, and the remaining gold coat on the microbridge is removed by reactive-ion etching. Finally, all devices thus fabricated are separated from each other by dicing the wafers.

Prototype devices for use in quasi-optical receivers for operating frequencies of 1.2 and 2.5 THz have been fabricated by this method. Tests of these devices have shown that they can be fabricated within reasonable tolerances for microbridge lengths and widths as small as 80 nm.

This work was done by Bruce Bumble and Henry LeDuc of Caltech for **NASA's Jet Propulsion Laboratory**. *Further information is contained in a TSP [see page 1].*

NPO-20023

Hybrid Superconductor/Semiconductor Planar Oscillators

Characteristics include frequency stability, low phase noise, and ability to withstand vibrations.

Lewis Research Center, Cleveland, Ohio

Hybrid high-temperature-superconductor (HTS)/semiconductor planar oscillator circuits that operate at a frequency of 8.4 GHz have been developed. In the original intended application, one of these circuits would serve as a local oscillator in a cryogenic heterodyne receiver in a spaceborne experiment on high-temperature superconductivity. The same attributes that make these circuits attractive for use aboard spacecraft could also make them attractive for use on Earth — especially in applications in which high frequency stability, low phase noise, and ability to withstand vibrations are required.

Like other planar microwave oscillators based on HTS resonators, these oscillators can be made to exhibit frequency stability almost as high as, and phase noise almost as low as, those of quartz-crystal- and dielectric-resonator-stabilized oscillators. An oscillator of the present type includes integrated circuitry that is less complex and more reliable, relative to the circuitry of quartz-crystal- and dielectric-resonator-stabilized oscillators. The resonance quality factor (popularly denoted as Q and defined as the energy stored in electromagnetic field ÷ energy dissipated in one cycle of oscillation) of an HTS resonator of the present type at a temperature of 77 K in the absence of an electrical load is typically about 10^4 — almost equal to the Q of an unloaded dielectric-resonator-stabilized oscillator; in contrast, the Q of an unloaded typical normal-metal resonator is $<10^3$.

The figure illustrates the layout of one of the hybrid HTS/semiconductor oscillators. All of the circuit elements are formed on the surface of a $LaAlO_3$ substrate. The active circuit element is a GaAs metal/semiconductor field-effect transistor (MESFET). The passive HTS circuit elements include the resonator, reactive feedback lines, transmission lines, and dc bias lines; these ele-

ments are formed by etching of a deposited HTS film of $YBa_2Cu_3O_{7-\delta}$. The MESFET is electrically connected to the HTS circuit elements by Au wires with a diameter of 0.7 mil (0.18 mm) that are thermosonically bonded in place. Layered Ag/Au contact pads are deposited at the outer ends of the bias lines. Ceramic-chip capacitors and thin-film resistors are thermosonically bonded in place to provide filtering for the bias lines.

At the time of reporting the information for this article, 20 of the oscillators had been fabricated and subjected to a number of tests, including vibration tests and assessments of the effects of variations in the fabrication process. Of the 20 oscillators, 10 were assembled into working units and their performances were measured. At a temperature of 77 K, levels of output power into a 50-Ω load ranged up to 10 dBm. During incorporation into a full cryogenic receiver, output power levels ranged from 0.0 to 3.0 dBm, with less than 50 mW of dissipation.

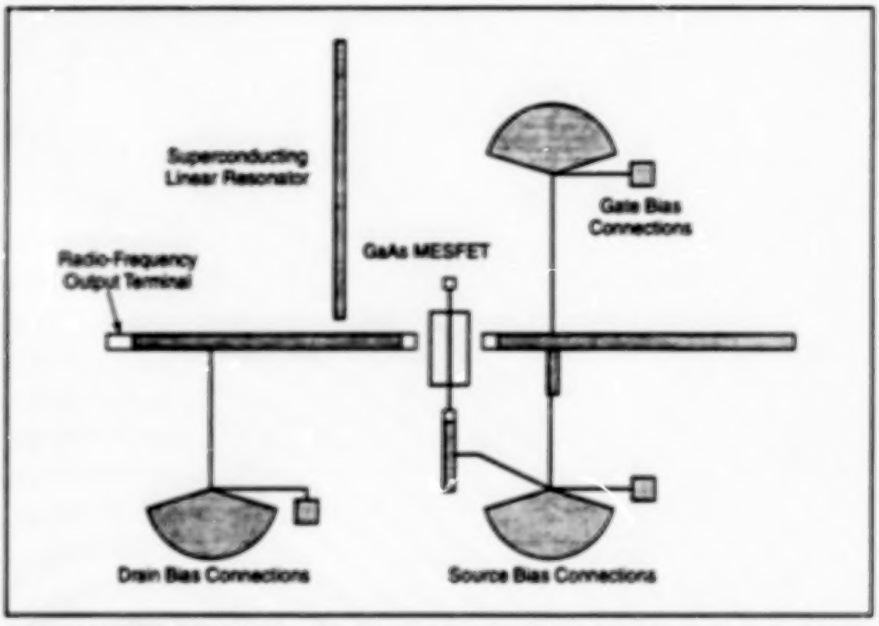

A Hybrid HTS/Semiconductor Oscillator is implemented as a planar circuit on a dielectric (lanthanum aluminate) substrate. The resonator is 173.5 mils (4.41 mm) long and 6.6 mils (0.17 mm) wide. The bias lines are 1.7 mils (0.04 mm) wide.

This work was done by F. A. Miranda, R. R. Romanofsky, and K. B. Bhasin of **Lewis Research Center** *and C. M. Chorey of NYMA, Inc. Further information is contained in a TSP [see page 1].*

Inquiries concerning rights for the commercial use of this invention should be addressed to NASA Lewis Research Center, Commercial Technology Office, Attn: Tech Brief Patent Status, Mail Stop 7–3, 21000 Brookpark Road, Cleveland, Ohio 44135. Refer to LEW-16536.

BLANK PAGE

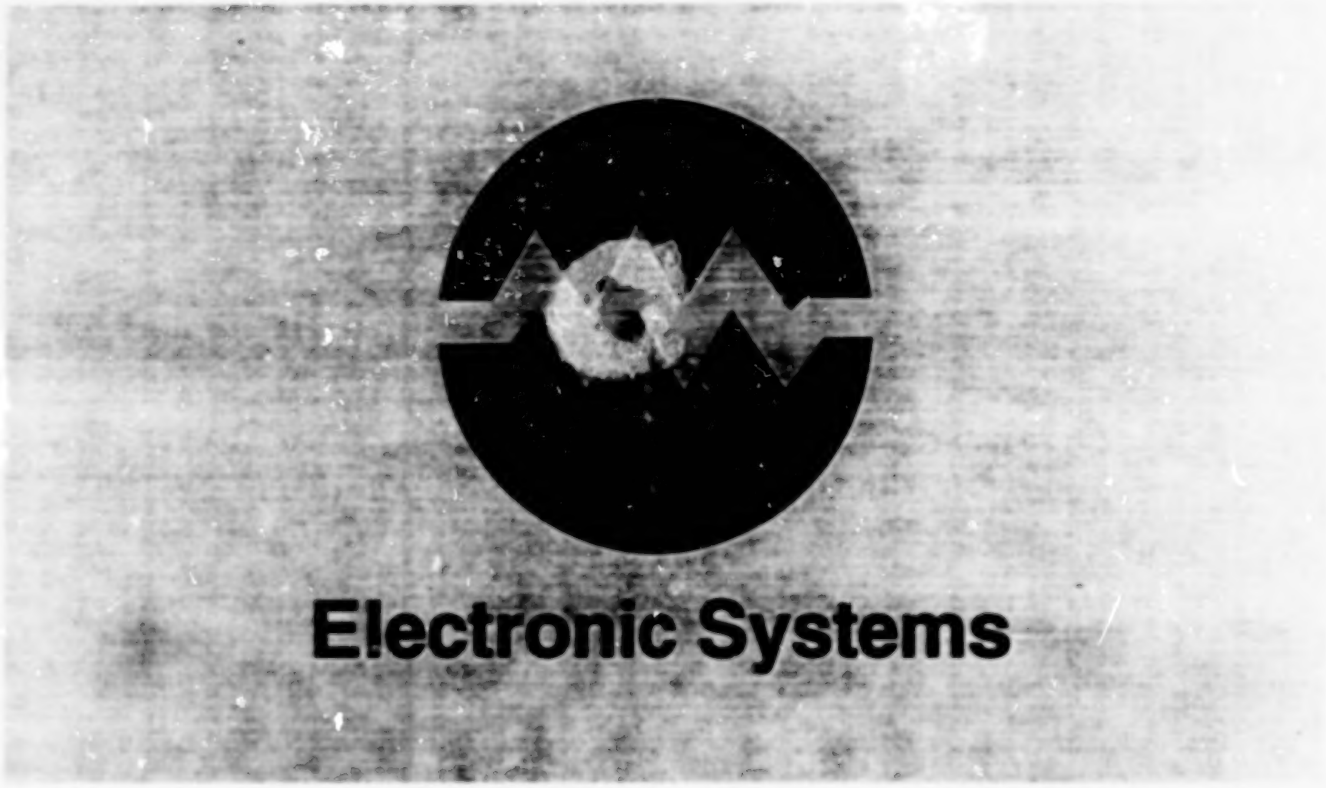

Hardware, Techniques, and Processes

15 Algorithm Estimates Doppler Shift in a Received DPSK Signal
15 ASIC for Viterbi Decoding With $2 \leq K \leq 15$ and $1/2 \geq r \geq 1/6$
16 Multimedia Operator Interface for a Health-Care Robot
17 Signaling-and-Detection Scheme for Beacon Monitoring

BLANK PAGE

Algorithm Estimates Doppler Shift in a Received DPSK Signal

Processing of delayed and undelayed versions of the signal yields the desired estimate.

NASA's Jet Propulsion Laboratory, Pasadena, California

An algorithm estimates the Doppler frequency shift in a received radio signal with square-wave-pulse binary differential-phase-shift-keyed (DPSK) modulation. [With little modification, the algorithm is also extensible to *M*-ary (where *M* is an integer > 2) DPSK modulation with pulse shapes other than square.] The algorithm was developed especially for use in processing a received K- or K_a-band signal in a ground mobile receiver in a ground-mobile/satellite communication system. There is a need for estimation of, and compensation for, large Doppler frequency shifts in such a receiver. The algorithm implements a feedforward (open-loop) estimation scheme, providing the needed Doppler estimate prior to detection and subsequent processing (see figure) for extraction of data symbols from the modulation.

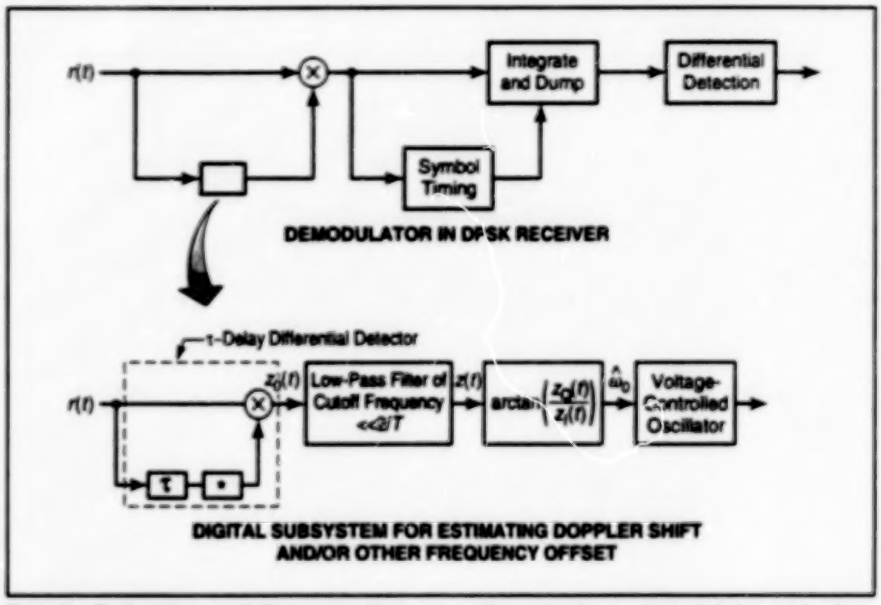

Doppler Estimation and Compensation are performed prior to demodulation and other processing.

Older closed-loop schemes for estimating and compensating for Doppler shifts do not work at Doppler shifts greater than fractions of symbol rates, nor do they work in the presence of the deep fading that often occurs in mobile operation. An older open-loop scheme is also limited to small Doppler shifts and depends on symbol synchronization. The present algorithm does not depend on symbol synchronization and performs well even at Doppler shifts well beyond the symbol rate. Furthermore, because it is a feedforward rather than a feedback algorithm, it offers at least the potential for better performance in the presence of fading.

Prior to processing via this algorithm, the input signal is mixed to baseband, then passed through a low-pass filter of cutoff frequency *B*/2 to reduce out-of-band noise. The in-phase (I) and quadrature (Q) components of the resulting input signal *r*(*t*) can be represented in complex form as

$$r(t) = s(t)\exp(-j\omega_0 t) + n(t),$$

where *t* is time; *s*(*t*) is the square-wave-pulse-shaped binary data-modulation signal with symbol period *T*; *n*(*t*) is the low-pass-filtered version of the additive white Gaussian noise, with independent I and Q components, that is received along with the signal; and ω_0 denotes the Doppler-frequency shift, which one seeks to estimate, and which is assumed to be constant during the time needed to make the estimate.

In this algorithm, *r*(*t*) is split into two paths, on one of which it is delayed by an interval τ, where $0 \le \tau < T$. The complex conjugate of the delayed signal $r(t-\tau)$ is mixed with the undelayed signal *r*(*t*) to obtain $z_0(t)$. The part of the algorithm described thus far can be characterized as implementing a τ-delay differential detector. It can be shown that provided the noise is negligible, one can estimate $\omega_0\tau$ as minus the arctangent of the ratio between the dc (zero-frequency) Q and I components of the output $z_0(t)$ of this detector. To isolate these zero-frequency I and Q components, it is necessary to filter out frequency components at the fundamental and harmonics of the symbol frequency 1/*T*; this is accomplished by low-pass-filtering $z_0(t)$ to obtain the complex dc signal *z*(*t*). The estimate $\hat{\omega}_0$ of the Doppler shift is then computed from

$$\hat{\omega}_0 = \left(-1/\tau\right)\arctan\left[z_Q(t)/z_I(t)\right],$$

where $z_Q(t)$ and $z_I(t)$ denote the Q and I components of *z*(*t*). The maximum size of the Doppler shift that can be tracked without incurring the integer-multiple-of-2π phase ambiguity is given by

$$|\hat{\omega}_0|_{max} = \pi/\tau$$

This work was done by Thomas C. Jedrey, Edgar H. Satorius, and Martin J. Agan of Caltech for **NASA's Jet Propulsion Laboratory**. *Further information is contained in a TSP [see page 1].*
NPO-19812

ASIC for Viterbi Decoding With $2 \le K \le 15$ and $1/2 \ge r \ge 1/6$

Decoding speed exceeds that of older prototypes.

NASA's Jet Propulsion Laboratory, Pasadena, California

An application-specific integrated circuit (ASIC) serves as a building block for a digital system that effects maximum-likelihood decoding of a Viterbi code (a binary convolutional error-correcting code) with a constraint length (*K*) in the range of 2 through 15 and a rate (*r*) in the range of 1/2 through 1/6. This ASIC is based on the same architecture as that of two older prototype *K* = 15, *r* = 1/6 Viterbi decoders, the first of which was reported in literature in 1988. These prototypes have func-

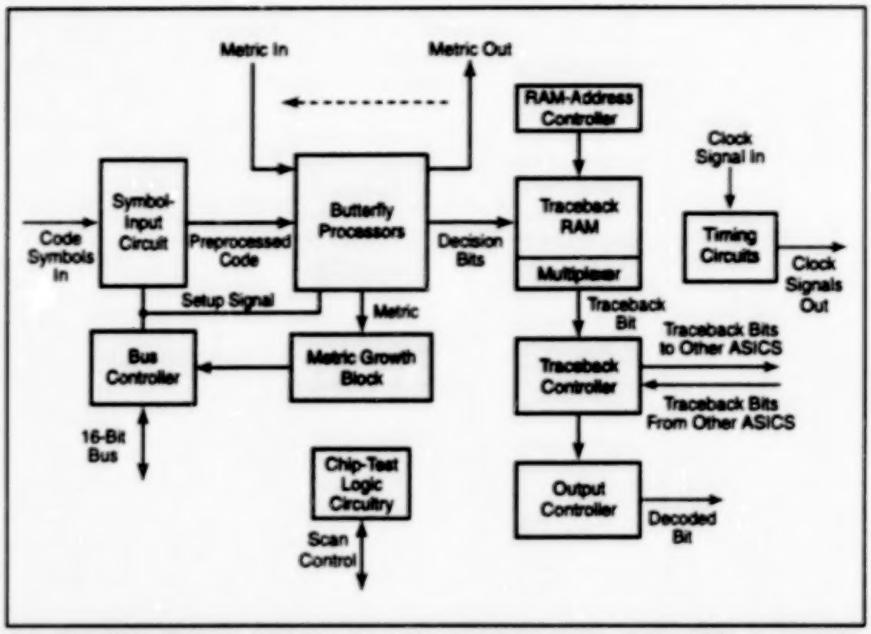

This Simplified Diagram illustrates the major functional blocks of the ASIC. A complete decoder for a $K = 15$, $r = 1/6$ Viterbi code contains 64 such ASICs.

tioned successfully in experiments, and their capabilities exceed those of state-of-the-art (K up to 7 and r at 1/2) commercial decoders as of the time of reporting the information for this article, but they have not been put into commercial production, partly because their complexities have given rise to reliability problems. Moreover, these prototypes have been limited to decoding speeds ≤ 750 kb/s.

A decoder built from multiple units of the present ASIC is capable of decoding at a speed up to 4.4 Mb/s. Other notable aspects of the decoder and its ASIC building blocks include (1) implementation of a "pipeline" scheme for traceback (reconstruction of the most likely sequence of recent code states); (2) a novel CMOS (complementary metal oxide/ semiconductor) current-logic (CMCL) input/output scheme that affords low switching currents, high immunity to noise, and fast signaling among ASICs; and (3) timing-error-detection circuitry that helps to ensure synchronization of each ASIC with an externally generated clock signal.

In global terms, decoding is performed by a traceback processor that reads a traceback random-access memory (RAM). The decoder contains 64 identical ASICs, each of which (see figure) contains 1/64 of the traceback RAM and 1/64 of other circuits that are called "butterfly processors" because a graphical representation of the arithmetic logic at each node pair has a butterflylike shape. However each ASIC contains a complete traceback processor, so that there is no problem of transferring traceback addresses among ASICs.

Code symbols enter each ASIC at the symbol-input circuit, where they are buffered and preprocessed. The preprocessed code symbols are fed to the butterfly processors, which produce metrics (measures of the likelihoods of candidate paths through sequences of code states). The metrics are fed, variously, back to the butterfly processors in the ASIC or to the butterfly processors in other ASICs. On the basis of comparisons between the metrics of the two alternative path branches that lead into each code state, the butterfly processors generate decision bits, which are transferred to the RAM. Pointers in the RAM-address controller keep track of the reading and writing locations. The traceback controller implements the traceback logic, which reads the RAM and puts out traceback bits to connect to the other ASICs. Data from the traceback controller are transferred to the output controller, which contains last-in/first-out (LIFO) memories. The output controller puts out the decoded data bit.

All registers in the ASIC are loaded initially from a 16-bit bus. The bus controller serves as the interface between the rest of the ASIC and the bus. All ASIC configurations are programmable and are set through this interface.

The ASIC includes metric accumulators (in the butterfly processors), which keep incrementing until they roll over. The metric growth block keeps track of the rate of growth in the metric accumulators to give a measure of how well the decoder is performing. A large metric-growth rate would indicate poor performance; this could occur because of a very low signal-to-noise ratio, or because of lack of synchronization of the decoder operation with the incoming code symbols.

This work was done by Gary R. Burke and William D. Whitaker of Caltech for ***NASA's Jet Propulsion Laboratory****. Further information is contained in a TSP [see page 1].*

In accordance with Public Law 96-517, the contractor has elected to retain title to this invention. Inquiries concerning rights for its commercial use should be addressed to

Technology Reporting Office
JPL
Mail Stop 122-116
4800 Oak Grove Drive
Pasadena, CA 91109
(818) 354-2240

Refer to NPO-19999, volume and number of this NASA Tech Briefs *issue, and the page number.*

Multimedia Operator Interface for a Health-Care Robot

The robot can be controlled by patients with some disabilities.

NASA's Jet Propulsion Laboratory, Pasadena, California

An operator interface is undergoing development along with other subsystems of a robot that would assist in caring for elderly and disabled patients. This development has been initiated in anticipation of an increasing need for long-term care, in both home and hospital environments, with decreasing ratios of medical personnel to patients. Robots of the type envisioned would be controllable by both medical personnel and patients with some disabilities. Typically, the robots would be used to perform routine, mostly nonmedical tasks like delivering food and retrieving articles of clothing or other objects for patients.

The prototype robot includes a battery-powered mobile platform equipped with a

color camera mounted on a pan-and-tilt head, and an array of ultrasound, infrared, and contact sensors for autonomous navigation. A fully developed robot would also include a manipulator arm. Some control functions are performed by a computer mounted on the platform; other control functions are performed by a computer at a control station, where the operator interface resides (see figure). In a fully developed robotic system of this type, the control station could be located at a patient's bedside or in a nurse's office, for example.

To accommodate the needs of patients and medical personnel and the limitations on dexterity of some patients in a variety of situations, the operator interface accepts inputs and generates outputs in a variety of media. In particular, it provides an integrated combination of voice, video, and computer graphical inputs and outputs, plus mouse and joystick inputs. The voice mode is the main command mode and is included primarily because many elderly and disabled patients would find it difficult or impossible to use the mouse and/or keyboard. The voice mode is implemented by a voice-recognition engine running commercial speech-recognition software that listens for voice input from the operator and seeks to match the operator's utterances with each of fourteen commands (e.g., stop, turn left, move forward) stored in active voice menus. When the robot receives and interprets a voice command, a speech synthesizer in the robot restates the command for confirmation.

The operator interface includes a graphical user interface that can present visual feedback in the forms of images from the video camera on the robot, images from a remote video camera (e.g., during a video conference with a physician), a graphical display of the robot on a map of the environment, or a graphical display of sonar readings of distances and directions from the robot to nearby objects. The data-entry portion of the graphical user interface includes interactive displays for using the mouse to select the voice mode, to set translational and rotational speeds of the robot, or to select the joystick to control motion. The mouse can be used to stop all motions of the robot in an emergency. The mouse can also be used to move a cursor to a target position indicated on the map graphical display and to command the robot to move to that position; when the mouse button is clicked at the target position, the robot moves toward the target, automatically avoiding obstacles along the way.

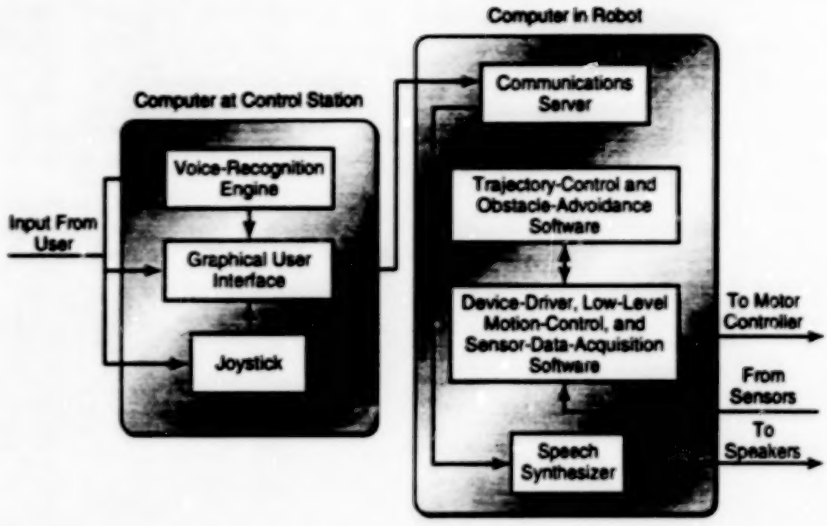

The Operator Interface resides in a computer at a control station that communicates with a computer in the robot.

This work was done by Paolo Fiorini, Homayoun Seraji, and Khaled Ali of Caltech and K. G. Engelhardt of KG Robotics for **NASA's Jet Propulsion Laboratory**. *Further information is contained in a TSP [see page 1].*
NPO-20072

Signaling-and-Detection Scheme for Beacon Monitoring

The signal level could be 10 dB below that required in a traditional BPSK scheme.

NASA's Jet Propulsion Laboratory, Pasadena, California

A signaling-and-detection scheme has been proposed for use in conjunction with the remote-monitoring concept described in "Beacon Monitoring Would Reduce Interactions With Remote Systems" (NPO-19706), *NASA Tech Briefs*, Vol. 21, No. 5 (May 1997), page 54. To recapitulate: A remote system (a spacecraft in the original intended application) would contain a semiautonomous computer-based monitoring subsystem that would analyze data acquired by onboard instrumentation and would produce a summary assessment of the status of the system. The summary assessment would be represented by one of four messages. To minimize the demand on communication resources and thereby minimize the cost of operation, the subsystem would ordinarily not transmit full telemetric data to a control station (a ground station in the original application). Instead, the subsystem would transmit one of the four messages as a radio beacon signal. Operators on the ground could decide, partly on the basis of the received beacon message, whether and when full telemetric data were needed. Full telemetric data would be transmitted from the remote system to the control station only on command by operators on the ground.

In the proposed scheme, each of the four beacon messages would be represented by a pair of subcarrier tones with unique frequency spacing. These tones would be phase-modulated onto a carrier signal with a modulation angle of 90°. The tones would be detected noncoherently at the control station. At the low data rate inherent in the four beacon messages, this scheme offers adequate performance at a signal level 10 dB below that needed for a bit-based, binary-phase-shift-keying (BPSK) scheme that is used to transmit full telemetric data. This 10-dB performance advantage could be exploited by

reducing the transmitted power at the remote station and/or using a smaller antenna to receive the signal at the control station. The larger antenna needed to receive full telemetry could thus be allocated to other tasks until there was a need to receive full telemetric data from the remote system.

The proposed scheme, and two alternative weak-signal-detection techniques that could be used in the scheme, have been tested in a laboratory, but have not yet been tested in an operational system. In both detection techniques, decision statistics are derived from incoherent sums of power spectra and compared with thresholds. In one technique, the frequency drift of the signal is modeled after evaluation of the power spectra; in the second technique, the frequency model is applied before computation of the power spectra.

This work was done by Miles K. Sue, Robert Kahn, Gabor Lanyi, Victor Vilnrotter, Marvin Simon, Ted Peng, John Caraway, and Bruce Crow of Caltech for **NASA's Jet Propulsion Laboratory**. *Further information is contained in a TSP [see page 1].*
NPO-20187

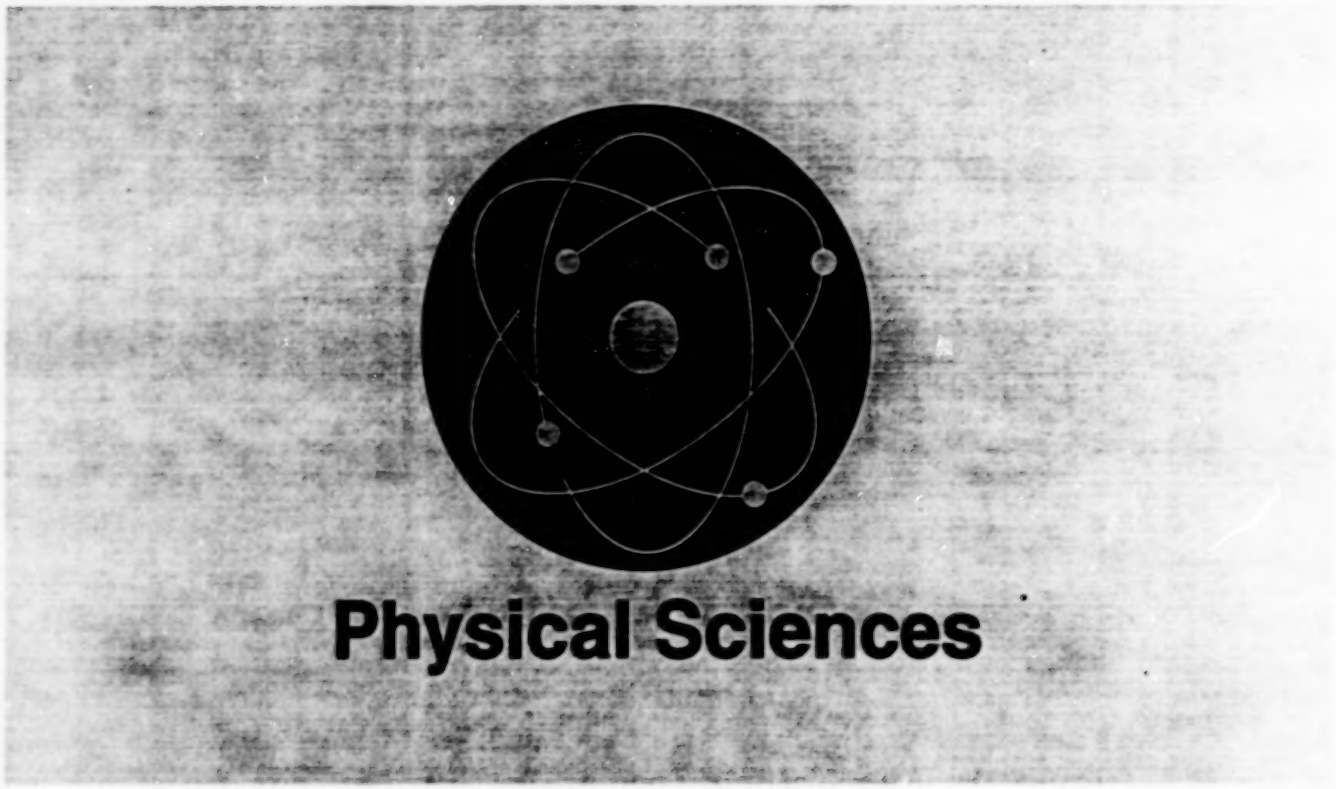

Physical Sciences

Hardware, Techniques, and Processes

21 Mathematical Model of Pyrolysis of Biomass Particles
22 Generalized Mathematical Model of Pyrolysis of Biomass
22 Mathematical Model of a Direct-Contact Pyrolysis Reactor
23 Automated Window Inspection Device
25 In Situ Interferometric Testing of a Vacuum-Chamber Window
26 Thermographic Detection of Defects in Refractory Composites
27 Oscillating-Flow Heat-Transfer and Pressure-Drop Test Rig
28 Protecting a Micromachined Accelerometer During Handling
29 Mass Analyzer With Rotating Electric Fields
30 Elevation Corrections for Absolute-Pressure Measurements

BLANK PAGE

Mathematical Model of Pyrolysis of Biomass Particles

The model qualitatively reproduces aspects of pyrolysis seen in experiments.

NASA's Jet Propulsion Laboratory, Pasadena, California

A mathematical model of a special class of solid/fluid chemical reactions has been developed for use in analyzing the pyrolysis of particles of cellulose, wood, and similar biomass materials. Although it involves some simplifying assumptions (as do all models of chemical and physical processes), this model is nevertheless sufficiently detailed to yield spatially and temporally resolved approximations of chemical compositions and temperatures of particles and of liquid and gaseous products as they evolve during the pyrolysis process.

In the model, each particle is assumed to be spherical and porous. The particle is assumed to be chemically reactive, with known volumetric reaction rates for the various chemical species present. It is assumed that the porosity (pore volume ÷ total volume) and the permeability of the particle are large enough to allow for continuous flows of gases. For these and other purposes, the detailed pore structure is not analyzed and instead, only the bulk or "effective" properties associated with porosity are represented. Unlike in some other models, conditions in the environment of the particle are not assumed to be quasi-steady. Conditions at the surface of the particle are allowed to evolve according to the equations of the model and the far-field temperature and pressure.

The model provides for the formation of solid (char), liquid (tar), and gaseous products. Both convection and diffusion of the liquid product(s) are neglected; this assumption is justified, provided that either the viscosity of the liquid substantially exceeds that of the gases or the characteristic reaction time of the liquid is much smaller than its characteristic diffusion and convection times.

The dynamics of flows of gases and of chemical reactions within the particle are represented by coupled equations for conservation of mass, momentum, and energy. For the gaseous chemical species, the equations for conservation of mass include both flow-divergence terms and source terms proportional to the products of partial densities and reaction rates. For the solid and liquid species, only the source terms are included. The reactions are assumed to be irreversible and of first order.

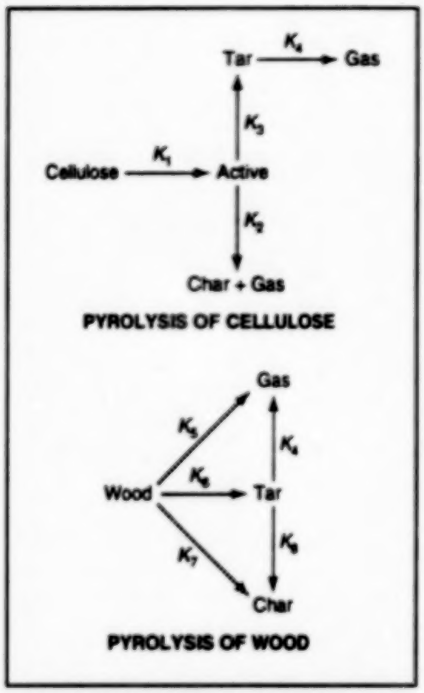

A Few Principal Chemical Reactions are included in the model of the pyrolysis of cellulose and wood. The reaction rates are calculated by the Arrhenius equation $K_i = A_i \exp(-E_i/\bar{R}T)$, where K is a reaction rate, A is a rate frequency constant, E is an activation energy, $\bar{R}$ is the universal gas constant, T is the absolute temperature, and the subscript i denotes the ith reaction path or chemical species.

For modeling conservation of energy, all species are assumed to be in local thermal equilibrium in a mixture. The partial internal energy of each chemical species is assumed to be proportional to the its partial density × its specific heat at constant volume × the local temperature. The rate of change of local internal energy is represented by a sum of (1) heat-release rates proportional to the chemical-reaction source terms, (2) conduction proportional to the local gradient of temperature × an effective thermal conductivity according to a mixture-and-porosity-based submodel, and (3) convection of heat via the flow of gaseous species.

The conservation of momentum for the gas phase is expressed by a single equation for radial flow of a compressible gas mixture through pores, with an effective molecular viscosity proportional to the porosity × the sum of mass-fraction-weighted viscosities of all gas species. The set of equations is completed by an equation of state, based on the perfect gas law, wherein the total local pressure is expressed in terms of the effective local total gas density, porosity, local temperature, and local volume fractions of the gas species.

The model was applied in a parametric study of the effects of initial reactor temperature, heating rate, porosity, and initial particle size on the char yields and conversion times in the pyrolysis of spherical biomass particles in initially quiescent superheated steam. In this study, reaction rates (see figure) were calculated from previously published data on the kinetics of chemical reactions for cellulose and wood. The equations of the model were solved numerically. The solutions qualitatively reproduced aspects of pyrolysis as observed in previous mathematical-modeling and experimental studies.

In particular, the numerical results indicated that one can reduce the production of char by decreasing the initial particle size or by increasing the reactor temperature and heating rate, but that the achievable decrease in the production of char is limited by endothermic reactions, heat capacities, and thermal diffusion. Three pyrolysis regimes were identified: (1) initial heating followed by (2) primary reaction at an effective pyrolysis temperature followed by (3) final heating. The relative durations of the regimes were found to be independent of reactor temperature and to be approximately 1/5, 3/5, and 1/5, respectively, of total conversion time. The results show that neglect of thermal and chemical-species boundary layers outside particles generally leads to overprediction of both pyrolysis rates and tar yields. Comparisons with experimental data revealed that wood-pyrolysis-kinetic data assumed in the study were not accurate.

This work was done by Josette Bellan and Richard S. Miller of Caltech for **NASA's Jet Propulsion Laboratory**. *Further information is contained in a TSP [see page 1].*

NPO-20070

Generalized Mathematical Model of Pyrolysis of Biomass

This model agrees well with experimental data.

NASA's Jet Propulsion Laboratory, Pasadena, California

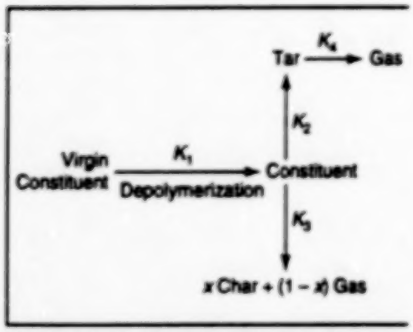

Figure 1. This Generic Reaction Scheme represents the pyrolysis of each primary constituent (cellulose, hemicellulose, or lignin). As in the model of the preceding article, each reaction is assumed to be irreversible and of first order, with a rate K_i given by the Arrhenius equation.

A generalized mathematical model has been devised for use in analyzing the pyrolysis of arbitrarily specified (but typical) biomass feedstocks at atmospheric pressure. The model represents both the microparticle (kinetically controlled) and macroparticle (diffusion-limited) types of pyrolysis.

The microparticle portion of the model is based on a superposition of the multistep chemical-reaction kinetics of the primary constituents of biomass; namely, cellulose, hemicellulose, and lignin. The submodel for each primary constituent accounts for decomposition into tar, char, and gas, with secondary decomposition of tar (see Figure 1). The formation of char is represented as taking place via competitive primary reactions of the active feedstock. The macroparticle portion of the model is constructed by coupling the foregoing kinetics, along with appropriate heats of reaction and physical properties of constituents, with the porous-particle model described in the preceding article, "Mathematical Model of Pyrolysis of Biomass Particles" (NPO-20070).

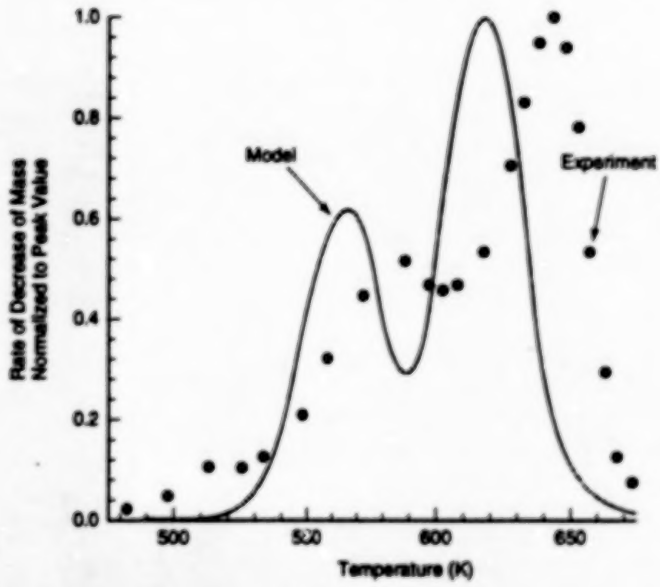

Figure 2. The Normalized Mass-Loss Rate of untreated bagasse as a function of temperature under microparticle TGA conditions at a heating rate of 10 K/min as computed by the model is compared here with data from a previous TGA experiment.

The chemical-kinetics parameters in the model were obtained from a combination of previous mathematical-modeling studies and experimental data on the pyrolysis of representative feedstocks (cellulose, lignin, and beech and maple wood). Then the model with the exact same parameters was used to predict selected aspects of the pyrolysis of different feedstocks: The predictions agreed well with data from thermogravimetric-analysis (TGA) and isothermal experiments on the pyrolysis of untreated microparticle bagasse (see Figure 2) and cherry, oak, and pine wood. Considering that the proportions of the three primary constituents vary widely in these feedstocks, the results can be interpreted as signifying that the chemical-kinetics part of the model is unexpectedly robust.

Results obtained with the macroparticle model generally agreed with the experimental data. The small deviations were attributed to differences in particle geometry between simulations and experiment, catalytic effects of mineral matter not considered in the model, and differences in properties of various feedstocks.

This work was done by Josette Bellan and Richard S. Miller of Caltech for **NASA's Jet Propulsion Laboratory**. *Further information is contained in a TSP [see page 1].*
NPO-20068

Mathematical Model of a Direct-Contact Pyrolysis Reactor

Gross features of pyrolysis phenomena relevant to designing efficient reactors can be analyzed.

NASA's Jet Propulsion Laboratory, Pasadena, California

A mathematical model has been developed for use in assessing the performances of direct-contact pyrolysis reactors used to convert particles of raw biomass materials (usually small wood chips) into char, tar, and gas. The optimal designs are here considered to be those that maximize the production of tar. In such a reactor, the particles are injected along with a flow of a hot feed gas (usually, superheated steam), into a chamber with a heated cylindrical or conical outer wall, are blown along the wall by the flow of gas, and are held against the wall by centrifugal force. Thus, the particles are heated primarily by direct conduction from the wall. Incompletely pyrolyzed particles are collected at the outlet and reinjected at

the inlet along with the hot gas and the raw feedstock.

The model features a simplified geometry (see figure) and some simplifying assumptions that, together, make it possible to numerically simulate gross features of flow and pyrolysis phenomena without excessive computation. The reactor wall is represented by a flat plate of finite length heated to a constant temperature T_{wall}. Superheated steam is injected in a turbulent flow at the left end of the wall with average lengthwise speed u_{inflow} and with a temperature T_{inflow}, which is somewhat less than T_{wall}. The particles are assumed to have simple parallelepiped shapes (to represent wood splinters).

The particles are assumed to remain in contact with the wall (with weight substituting for centrifugal force) with their long axes parallel to the flow. Incompletely pyrolyzed particles that leave the wall at the right end are reinjected at the left end. The reactor is represented as operating in a steady state by specifying rates of injection of feedstocks at various stages of pyrolysis (fresh particles and reentrained particles) and associated particle sizes.

The model includes submodels of pyrolysis of particles, turbulent boundary-layer flow, and particle trajectories. The pyrolysis submodel is the one described in the preceding article, "Generalized Mathematical Model of Pyrolysis of Plant Biomass" (NPO-20068), adapted to the present slab geometry. The flow submodel incorporates the long-time-averaged Navier-Stokes equations with a two-equation sub-submodel of turbulence and a no-slip condition on the wall; the flow submodel simulates the development of a turbulent boundary layer, within which the particles quickly become deeply embedded as they are convected downstream. In the particle-trajectory submodel, each particle is represented as moving under the combined influences of the flow (with drag forces represented by a simplified sub-submodel of flow in the immediate vicinity of the particle) and friction with the wall. These submodels are coupled through boundary conditions and conservation laws, and the resulting equations of the overall model are solved numerically.

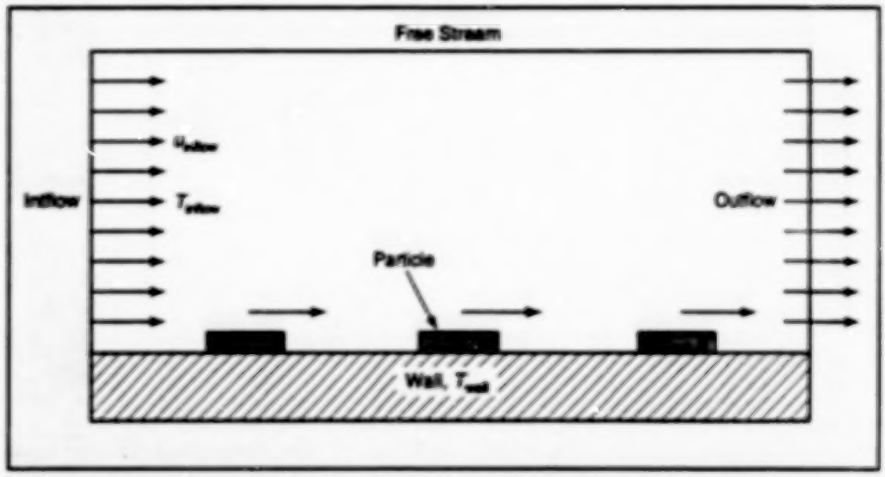

The Flat-Plate Reactor and the flow, thermal, and chemical phenomena that take place in the reactor are represented in a simplified geometry in a Cartesian coordinate system.

Calculations were performed for two-dimensional particles of different aspect ratios as well as one-dimensional particles (in the direction perpendicular to the wall), and it was found that the one-dimensional model gives a conservative estimate of both the conversion time and of the amount of tar collected. Directional effects from variations in thermal conductivity and permeability were found to be relatively small. The evolution of pyrolysis was found to be effectively uncoupled from the boundary-layer flow and to be determined primarily by T_{wall}. The foregoing plus other findings suggest that direct-contact reactors offer potential for tar-production efficiencies greater than those of noncontact and semicontact reactors. Tar yields were found to be maximized for small particles and wall temperatures of about 800 K. Ratios between tar-output and feedstock-input rates were found to be independent of injection rates under the conditions studied.

This work was done by Josette Bellan and Richard S. Miller of Caltech for **NASA's Jet Propulsion Laboratory**. *Further information is contained in a TSP [see page 1].*

NPO-20069

Automated Window Inspection Device

Both surface and subsurface flaws can be identified and located reproducibly.

John F. Kennedy Space Center, Florida

The Automated Window Inspection Device (AWID) is a prototype apparatus for computer-controlled, noncontact inspection of windows, with reproducible positioning and electronic recording of data on the locations, sizes, and depths of flaws. The AWID was developed to accelerate and facilitate (1) postflight inspections of the windows on the space shuttle for damage by micrometeorites and (2) the recording, analysis, and retrieval of records of such inspections. The AWID could also be adapted to industrial inspection of window glass prior to cutting, and to inspection of windows on aircraft and land vehicles.

The AWID includes a scanner housing on a two-dimensional (x–y) translation mechanism on a portable frame that mates with posts on the window frame for proper location with respect to the window to be inspected. The translation mechanism comprises x and y drives, each actuated by a stepping motor under computer control for automated or manual scanning. The scanner housing contains two optical inspection instruments; a polariscope for locating both surface and subsurface flaws, and a refocus microscope with focus depth adjustable by use of a third (z-axis) stepping motor for measuring the depths of selected flaws.

The polariscope can reveal otherwise invisible subsurface damage ("bruises") via the effects of subsurface stresses on polarized light. The polariscope includes an illumination and an imaging module (see figure). A lamp in the illumination module consumes a power of 3.8 W and features a nearly-square-appearing tungsten filament. A lamp lens of 6-mm diameter and 6-mm focal length projects an image of the filament onto an

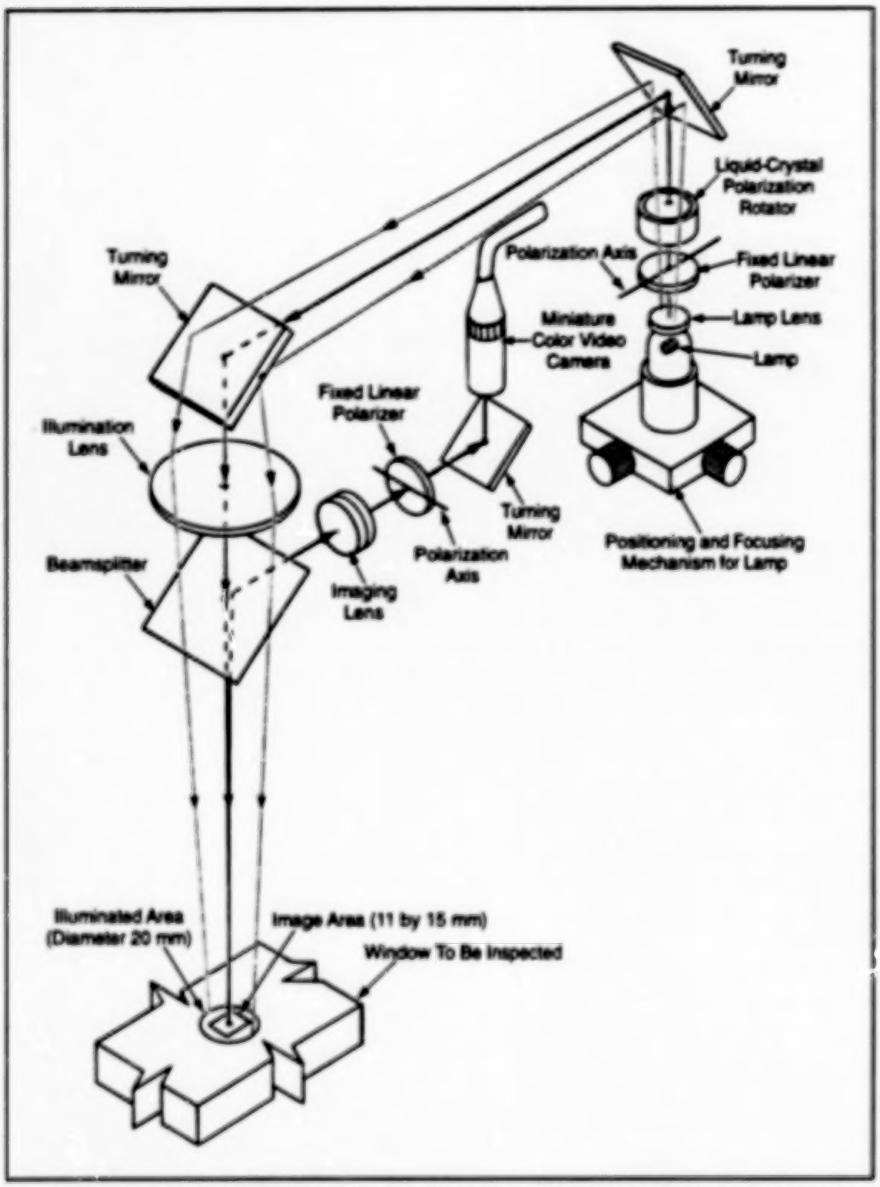

The Polariscope in the AWID includes a liquid-crystal polarization rotator that enables operation in two modes: (1) illumination and imaging polarizations parallel for detecting surface flaws, and (2) illumination and imaging polarizations orthogonal for detecting subsurface flaws.

illumination lens. The image of the filament fills the aperture of the illumination lens, providing nearly uniform illumination across the entire field. The illumination lens projects a magnified image (about 20-mm diameter) of the lamp lens onto the window.

The polariscope exploits the approximately 4 percent of the illumination that is reflected from each surface of the window. By use of a beam splitter and an imaging lens, light from an 11-by-15-mm portion of the 20-mm-diameter illuminated area is focused into a miniature color video camera. On its way to the camera, the light passes through a fixed linear polarizer. As explained below, the polariscope can operate alternately in a surface-damage-detection mode and a subsurface-damage-detection mode.

In addition to passing through the lamp lens, light from the lamp passes through a fixed linear polarizer and a liquid-crystal variable polarization rotator. The polarization axes of the two linear polarizers are orthogonal. In the surface-damage-detection mode, a square wave with a frequency of 2 kHz and an amplitude between 2 and 3 volts is applied to the polarization rotator, causing the plane of polarization of the illuminating light to be turned about 90° and thus lie approximately parallel to the polarization axis of the polarizer in front of the camera. As a result, an image of surface flaws is formed in the camera in reflected parallel-polarized light, in the same manner as in the case of ordinary unpolarized light.

For operation in the subsurface-damage-detection mode, no voltage is applied to the polarization rotator, causing the plane of polarization of the illuminating light to remain perpendicular to the polarization axis of the polarizer in front of the camera. In this mode, the illumination reflected (without change of polarization) from the front surface is polarized perpendicularly to the axis of polarization of the polarizer in front of the camera and is thus prevented from reaching the camera. However, the stress field in the interior of the window causes the polarization of light reflected from the rear surface to rotate by an amount that depends on wavelength. As a result, any subsurface damage is seen as a colored image on a darker background. The characteristic time for switching between surface and subsurface polarization modes is 30 to 50 ms.

After a scan has been performed to locate surface and subsurface flaws in *x* and *y*, the refocus microscope is used to locate flaws in *z*. The microscope is mounted in the scanner housing next to the polariscope and is accurately positioned in *x* and *y* over each flaw to be inspected. The refocus microscope has an "extend-retract" feature to prevent any interference with the polariscope during *x*-*y* scans. The microscope is equipped with miniature strain gauges, which act as limit switches to prevent damage in collisions between the microscope and other objects near or on the window undergoing inspection.

Two desktop computers are used for control, analysis, and operator interface. Dedicated image-processing circuit boards relieve the computers of much of the analysis effort.

This work was done by Matthew J. Verdier and Frederick W. Adams of **Kennedy Space Center** *and Stuart M. Gleman, Stephen W. Thayer, Carl G. Hallberg, Joseph E. Kachnic, Curtis M. Lampkin, and Terry D. Greenfield of I-NET. Further information is contained in a TSP [see page 1].*

Inquiries concerning rights for the commercial use of this invention should be addressed to the Patent Counsel, Kennedy Space Center [see page 1]. Refer to KSC-11889.

In Situ Interferometric Testing of a Vacuum-Chamber Window

Distortion is measured interferometrically with the help of a collimator.

NASA's Jet Propulsion Laboratory, Pasadena, California

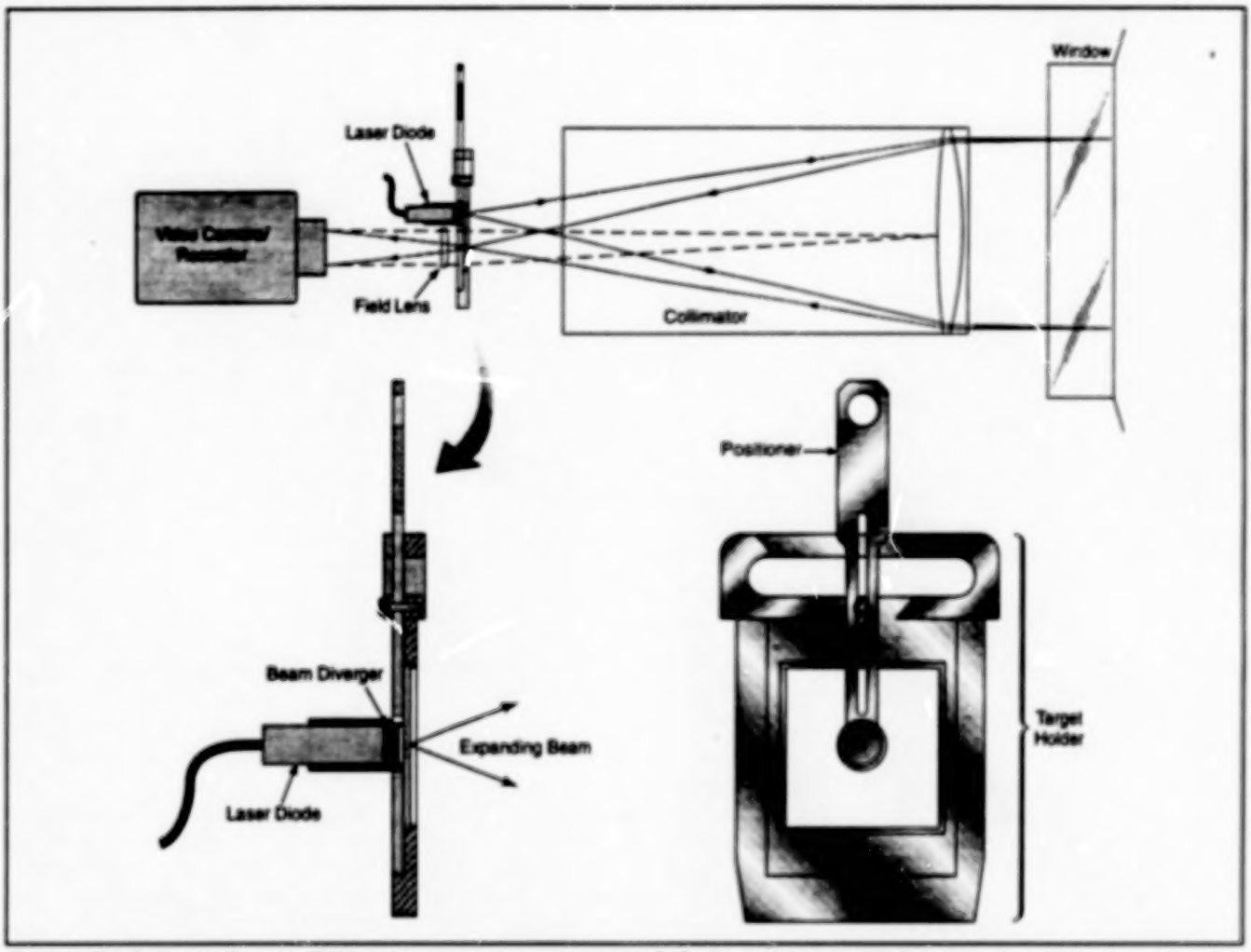

Figure 1. The Collimator Target Is Replaced by a laser-diode subassembly. **Reflections of the laser light from the surfaces of the window give rise to interference fringes indicative of the quality of the window.**

A relatively simple, direct interferometric technique has been devised for measuring the optical distortion produced by a window in a thermal vacuum chamber. The window of interest can be tested in place, under actual operating conditions. The equipment used in this technique includes a collimator, a laser diode, and a video camera/recorder.

If the window is part of a chamber in which an optical instrument is tested, then the collimator used to test the window is the same one used to test that instrument, and it is installed in the same position and orientation as in testing that instrument. The target holder of the collimator is replaced by an identical holder, on which a laser-diode assembly is mounted in place of the collimation target (see Figure 1). The laser-diode assembly comprises a laser-diode-and-beam-diverger subassembly mounted on a positioning arm, which is attached to a target cell at a spring-loaded pivot point. The laser-diode-and-beam-diverger subassembly can be positioned anywhere in the field of view of the collimator to accommodate misalignment between the optical axes of the collimator and window.

Figure 2. This Interferogram was recorded during operation of the thermal vacuum chamber at a temperature of −5 °C.

The laser beam is expanded, then collimated, then reflected from both surfaces of the window. The reflected light travels back through the collimator, which focuses this light. Provided that the wedge in the window is not too large (3 to 7 interference fringes over the working aperture would be ideal), the focused reflected light forms interference fringes of the Fizeau type; these fringes indicate directly the optical quality of the window. The interference fringes can be recorded by use of the video camera/recorder (see Figure 2). It might be necessary to use a field lens to match pupils to eliminate vignetting and enable sharp focus of the collimator pupil.

This work was done by Lawrence J. Steinle and David I. Brown of Caltech for **NASA's Jet Propulsion Laboratory**. *Further information is contained in a TSP [see page 1].*

NPO-19895

Thermographic Detection of Defects in Refractory Composites

Thresholds of detectability have been determined.

Lewis Research Center, Cleveland, Ohio

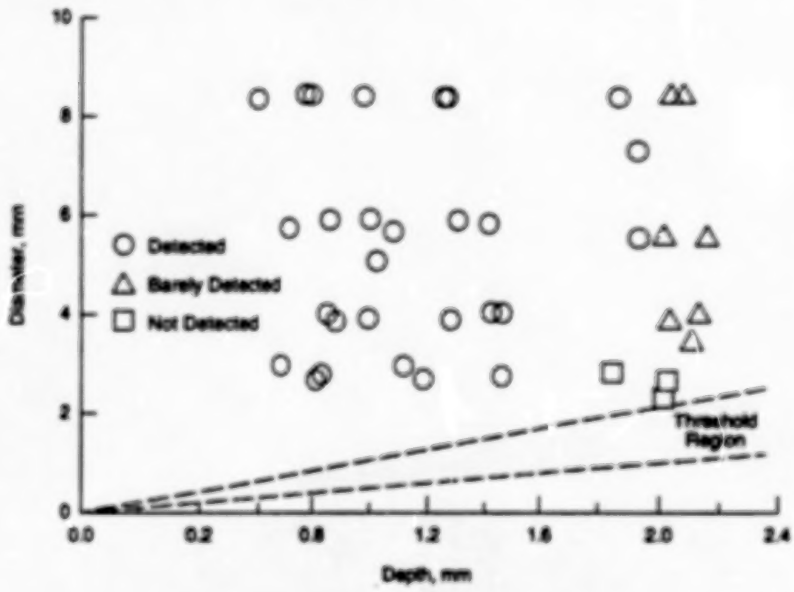

Figure 1. An Empirical Rule for the Threshold of Detectability of defects in SiC/SiC is determined by plotting a distribution of defects and indications regarding detectability by the thermographic technique used in the experiments.

Significant effort and resources are being expended to develop ceramic-matrix composite (CMC), metal-matrix composite (MMC), and polymer-matrix composite (PMC) materials for high-temperature engine components and other parts in advanced aircraft. The development of composite materials is also being pursued actively in the automobile and sporting-equipment industries, among others. A portion of the development effort involves the assessment of nondestructive-evaluation (NDE) techniques for detecting flaws in these materials. Recent advancements in infrared-camera technology and computer power have made thermographic (infrared) imaging systems worth reconsideration as reliable tools for NDE of these materials. Thermography offers the advantages of real-time inspection, no contact with samples, nonionizing radiation, capability for inspection of samples with complex shapes, variable sizes of fields of view, and portability.

An experimental study sponsored by NASA Lewis Research Center was performed to evaluate the capability afforded by a thermographic imaging technique for detection of defects in four composite materials of interest as high-temperature structural materials. The materials studied were two CMCs, one MMC, and one PMC; artificial defects in the form of flat-bottom holes with diameters from 1 to 13 mm and depths from 0.1 to 2.5 mm into specimens (2 to 3 mm thick) of these materials. In the thermographic imaging technique used, the source of heat was a pair of xenon flash lamps that faced the same side of the specimen as that observed by an infrared camera.

In the experiments, limits of detectability based on the depths and diameters of the holes were determined for each specimen material. For a SiC/SiC CMC, it was found that defects with depths ≤1.8 mm and diameters ≥2.6 mm will probably be detected (see Figure 1) by the technique used in these experiments. Similarly, it was found that for a composite of SiC fibers in a calcia/alumina/silica matrix (SiC/CAS) defects with depths ≤1.8 mm and diameters ≥1.6 mm will probably be detected; for a MMC of SiC/Ti, defects with depths ≤1.6 mm and diameters ≥3.2 mm will probably be detected; and for a PMC of graphite/polyimide, defects with depths ≤1.8 mm and diameters of about 3 to 12 mm will probably be detected. Depth appears to be the limiting variable with regard to detectability in the PMC.

As part of the study, thermographic images and observations about detectability were compared with results from ultrasonic and x-radiographic imaging to highlight the relative strengths and weaknesses of each imaging technique as applied to the composite materials studied. For example, Figure 2 shows thermographic images along with film x-radiographic and ultrasonic images for SiC/SiC specimens. The x-radiographs clearly reveal all defects. The ultrasonic pulse/echo image gives very obvious indications of most defects because of the porosity (about 15 percent) of SiC/SiC. The ultrasonic through-transmission image clearly shows all defects at shallow and intermediate depths.

Overall, this study has yielded baseline results that can be expected to enable material developers and component designers to determine whether the thermographic technique used can reveal "critical" defects. The technique is applicable to inspection of composite-material structures in any industry. Examples of materials and structures amenable to such inspection include tires, composite hulls of boats, composite frames of bicycles, and multilayer thick tapes.

This work was done by Don J. Roth of **Lewis Research Center**, *James R. Bodis of Cleveland State University, and Chip Bishop of Bales Scientific, Inc. Further information is contained in a TSP [see page 1].*

Inquiries concerning rights for the commercial use of this invention should be addressed to NASA Lewis Research Center, Commercial Technology Office, Attn: Tech Brief Patent Status, Mail Stop 7–3, 21000 Brookpark Road, Cleveland, Ohio 44135. Refer to LEW-16418.

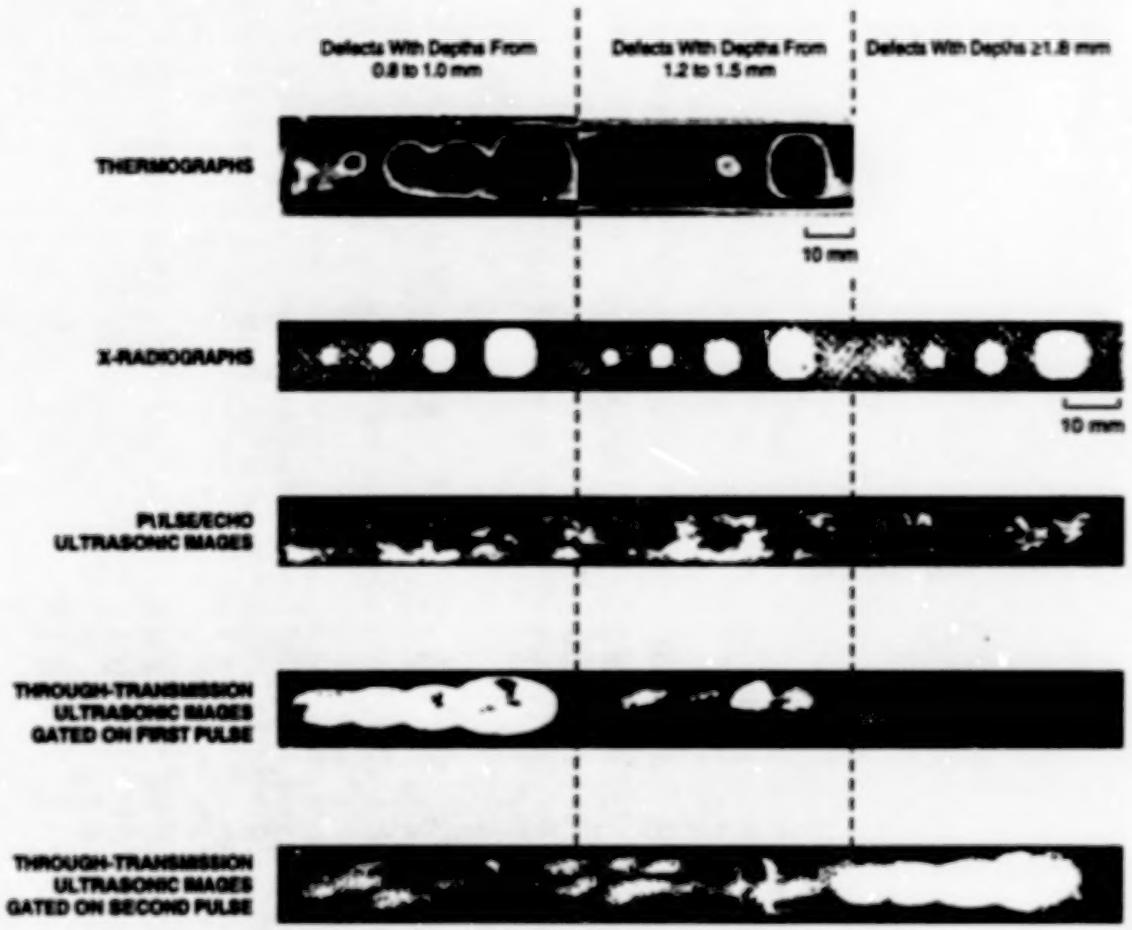
Defects With Depths From 0.8 to 1.0 mm
Defects With Depths From 1.2 to 1.5 mm
Defects With Depths ≥1.8 mm
THERMOGRAPHS
10 mm
X-RADIOGRAPHS
10 mm
PULSE/ECHO ULTRASONIC IMAGES
THROUGH-TRANSMISSION ULTRASONIC IMAGES GATED ON FIRST PULSE
THROUGH-TRANSMISSION ULTRASONIC IMAGES GATED ON SECOND PULSE

Figure 2. Images of SiC/SiC Specimens With Defects, made by several different NDE techniques, show different capabilities for revealing the defects. The through-transmission ultrasonic images have been distorted by graphical manipulation.

Oscillating-Flow Heat-Transfer and Pressure-Drop Test Rig

Test specimens are plugs of material representative of regenerator matrices of Stirling engines.

Lewis Research Center, Cleveland, Ohio

The figure illustrates an apparatus for measuring heat-transfer and pressure-drop characteristics of porous plug specimens in oscillating flows. The apparatus is built around an oscillating-flow test rig that was originally designed for pressure-drop (but not heat-transfer) measurements and has since been modified and refined. The flows and specimens are chosen to be representative of those encountered in the regenerators of Stirling engines.

The apparatus includes an assembly of a piston cylinder, cooling section, specimen holder, and heating section aligned sequentially from bottom to top along a vertical flow path. The foregoing assembly is contained in a pressure vessel to enable testing at specified elevated pressures. The oscillating flow is generated by the piston, which fits closely in the cylinder and is driven by a variable-stroke, variable-frequency linear motor.

The bottom end of the heating section opens to the top of the specimen holder, while the top end of the heater opens to a relatively large, fixed, thermally insulated buffer volume. A capillary tube vents the buffer volume to the surrounding space within the pressure vessel.

The heating section comprises a copper cylinder with drilled flow passages and with electrical band heaters clamped to its outer surface. The electrical power to the heaters is regulated by a commercial temperature controller. The cooling section is a shell-and-tube heat exchanger, with circulating water at controlled temperature serving as the coolant.

Five fine-wire thermocouples are installed on each face of a specimen. The specimen with thermocouples attached is sandwiched between flow-diffuser disks. The sandwich is installed in the specimen holder.

Because of the large volume and other aspects of the design, the pressure swing in the piston cylinder is attributable mostly to frictional pressure drop in the specimen and in the heating and cooling sections, rather than to compression effects. Therefore, the mass flow rate is very nearly sinusoidal and spatially uniform in the specimen and in the heating and cooling sections.

In its heat-transfer mode, the apparatus is used to measure the net thermal-ener-

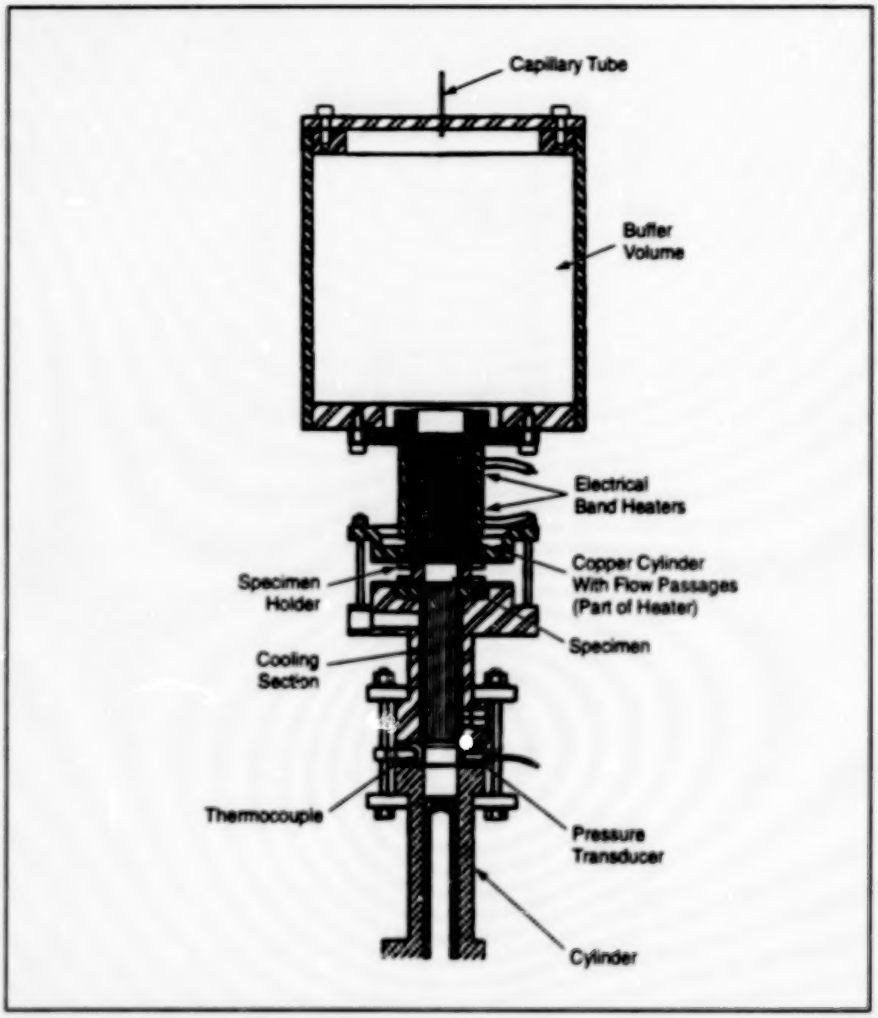

This **Oscillating-Flow Test Rig** provides for measurement of thermal and flow properties of specimens representative of regenerator matrices in Stirling engines, or of other, similar specimens of porous materials in general.

gy flux, which is the quantity of "bottom-line" importance in a Stirling engine. During operation, the piston is actuated, while the heating section is maintained at a temperature about 200 °C above that of the cooling section, giving rise to a temperature gradient in the specimen. The resulting axial conduction and imperfect heat transfer give rise to a net thermal flux along the specimen; this flux is ultimately rejected to the cooler, where it is measured. Static-conduction losses through cylinder walls and flanges and piston work due to pressure drop also contribute to cooler heat rejection, but these quantities can be calibrated out, so that it is possible to infer the thermal performance of the specimen in isolation.

Specimens tested thus far have been made of woven metal screens and metal felts, with a wide range of porosities, all representative of Stirling-engine regenerator matrices. Experiments on these specimens have yielded generic correlations for friction factors, Nusselt numbers, axial-conductivity-enhancement ratios, and overall-heat-flux ratios.

This work was done by Diane M. Chapman of **Lewis Research Center** *and D. Gedeon of Gedeon Associates and J. G. Wood of Wood Experimental. Further information is contained in a TSP [see page 1].*

Inquiries concerning rights for the commercial use of this invention should be addressed to NASA Lewis Research Center, Commercial Technology Office, Attn: Tech Brief Patent Status, Mail Stop 7–3, 21000 Brookpark Road, Cleveland, Ohio 44135. Refer to LEW-16448.

Protecting a Micromachined Accelerometer During Handling

The proof mass is clamped electrostatically.

NASA's Jet Propulsion Laboratory, Pasadena, California

A highly sensitive micromachined accelerometer that is intended to be exposed to very small accelerations during operation incorporates features for protection against much larger accelerations during handling and transport. More specifically, the accelerometer is designed to measure acceleration as small as 10^{-6} × that of normal Earth gravitation (*g*), yet can withstand accelerations as large as 200 *g* when the protective function is activated.

The accelerometer is made from four bulk micromachined silicon dice. Two of the dice are made into a square proof mass 1 cm² in area and 0.8 mm thick supported by eight folded cantilever springs, each spring being 1 cm long, 100 μm wide, and 25 μm thick. Another die contains four quadrature electrodes, plus a tip electrode that is placed near an electrode on the proof mass. The displacement of the proof mass is inferred from measurement of the quantum-mechanical-tunneling electron current between the tip electrode and an electrode on the proof mass; this tunneling-tip aspect of the design is similar to that of a scanning tunneling microscope and offers the advantage of high sensitivity (displacements as small as 10^{-3} Å can be measured). The remaining die, called the "force plate," contains a single electrode that is used to control the position of the proof mass.

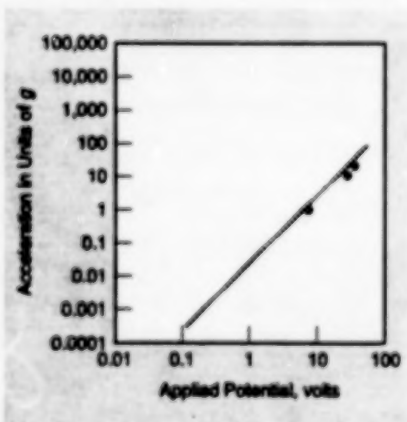

The **Acceleration That the Accelerometer Can Withstand** increases with the clamping force, which is proportional to the square of the applied potential.

The spring-and-mass and tip-electrode structures are delicate; this is an unavoidable aspect of the design necessary for

achieving the required sensitivity, but it makes these structures vulnerable to damage in the presence of large accelerations. Accordingly, during handling and transport, the single control electrode on the force plate is also used to clamp the proof mass away from the tip electrode and against the force plate. This clamping is effected by applying sufficient electrostatic potential (see figure) between the control electrode and an electrode on the proof mass to pull the proof mass into contact with the force plate. An oxide layer on the surface of the force plate prevents undesired electrical contact between the control and proof-mass electrodes.

This work was done by Frank T. Hartley of Caltech and Paul M. Zavracky of Northeastern University for **NASA's Jet Propulsion Laboratory**. *Further information is contained in a TSP [see page 1].*
NPO-19813

Mass Analyzer With Rotating Electric Fields

Orthogonal dipole electric fields would disperse incident ions according to their charge-to-mass ratio, analogous to making Lissajous figures with ions.

NASA's Jet Propulsion Laboratory, Pasadena, California

A device for measuring the distribution of masses in an atmosphere or plasma exploits the electrostatic deflection of ions in a rotating magnetic field. A magnetic field is not required. The device is simple to construct, can be made small, and is amenable to micromachining techniques such as LIGA (Lithographie-Abformung und Galvanoformung), or equivalent.

This so-called rotating-field (*rf*) analyzer transmits ions of a particular charge-to-mass ratio. One computes masses from this ratio by either knowing the charge from a separate measurement or making the usual assumption that each ion carries only one or a few units of charge. The device (see figure) consist of a rectangular parallelpiped chamber with four conducting, insulated walls to which the *rf* voltages are applied, an entrance aperture, and a detector face. Dimensions are $x_0 \times y_0 \times z_0$ with the Cartesian origin at the center of the ion-entrance aperture. Ions enter the device at a particular velocity $\mathbf{v}$, polar angle θ, and azimuthal angle ϕ [where $\mathbf{v} = \hat{\mathbf{x}}\sin\theta\cos\phi + \hat{\mathbf{y}}\sin\theta\sin\phi + \hat{\mathbf{z}}\cos\theta$]. Uniform, sinusoidally-oscillating orthogonal electric fields E_x and E_y are established in the chamber by applying corresponding voltages V_x and V_y to the electrodes (omitted from the figure for clarity). The electric fields or applied voltages are made to oscillate at the same frequency f, and 90° out of phase with each other, so that the resultant electric field rotates about the $\hat{\mathbf{z}}$ direction with frequency f. A straightforward analysis shows that, for homogeneous electric fields close to the axis, the $x(T)$, $y(T)$ position of an ion between the plates is simply given by

$$\frac{x(T)}{\lambda_x} = \cos\omega t_0 - \cos\omega(T + t_0) - \omega\sin\omega t_0 \qquad (1a)$$

$$\frac{y(T)}{\lambda_x} = \sin\omega t_0 - \sin\omega(T + t_0) - \omega\cos\omega t_0 \qquad (1b)$$

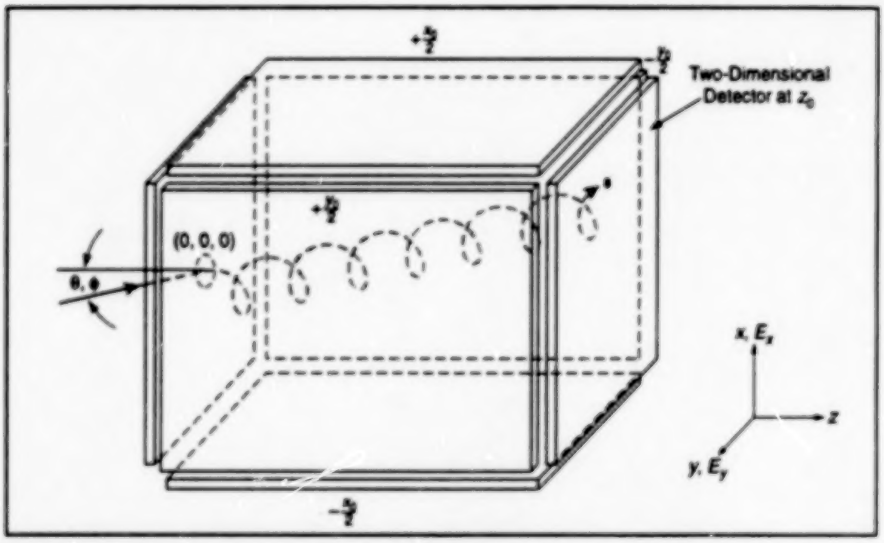

Ions Would Travel Along Spiral Trajectories under the influence of a rotating electric field until they struck a two-dimensional detector in the plane $z = z_0$.

Here, $\omega = 2\pi f$ is the angular frequency, T is the time the ion spends in the dipole fields, and t_0 is the time of arrival of the ion at the entrance aperture relative to the phase of the *rf* field. The assumption of zero velocity perpendicular to the axis has been made for simplicity. The quantities

$$\lambda_x = \frac{e}{m}\left(\frac{V_x}{\omega^2 x_0}\right) \text{ and } \lambda_x = \frac{e}{m}\left(\frac{V_y}{\omega^2 y_0}\right)$$

are scaling parameters, which describe the amplitude of ion motion between the plates. This amplitude is seen to be linearly proportional to the charge-to-mass (e/m), electric fields (V_x/x_0, V_y/y_0), and inversely proportional to ω^2. To see how the output pattern at the detector plane $z = z_0$ looks, one would first define the incident particle velocity, then "tune" the *rf* angular frequency so that $\omega T = 2\pi$ for that velocity. In this case, one can obtain the simple expression

$$\frac{x^2(T)}{\lambda_x^2} + \frac{y^2(T)}{\lambda_y^2} = 1$$

Hence, the locus of points at $z = z_0$ is a circle for each e/m. This is similar to the familiar Lissajous figures one makes with electrons and an oscilloscope. The figure could be detected by an area detector, such as a microchannel plate or a charge-coupled device. The resolution of the device, or separation between adjacent e/m, will depend on the input- aperture diameter, angular width of the incident beam, and homogeneity of the fields. Some of these effects can be obtained by taking suitable differentials of Eqs. 1a and 1b.

To confirm the behavior in Eqs. 1a and 1b, computer simulations of this device were carried out using a three-dimensional, non-space-charge limited fields-and-trajectories code. The device was also tested in the laboratory using a cell of dimensions 2 mm × 2 mm × 20 mm. Mass spectra were obtained from a commercial ion source. Since the input energies of the ions from the source were equal, but the input velocities could not be made equal, each ion

was detected by "tuning" ω to its particular velocity, then detecting its transmitted current. One could also use the device as a velocity selector by detecting only those ions with a specific **z**-component of velocity given by $v \cos \theta = z_0/T$. For this, one would pulse the ions into the cell, then gate the detector "on," after the interval T. Suggestions along these lines were reported earlier in, "Ballistic Mass and Velocity Analyzer" *NASA Tech Briefs* (NPO-19235), Vol. 20, No. 6, (June 1996) page 57.

This work was done by Steven J. Smith and Ara Chutjian of Caltech for **NASA's Jet Propulsion Laboratory**. *Further information is contained in a TSP [see page 1].*

In accordance with Public Law 96-517, the contractor has elected to retain title to this invention. Inquiries concerning rights for its commercial use should be addressed to

Technology Reporting Office
JPL
Mail Stop 122-116
4800 Oak Grove Drive
Pasadena, CA 91109
(818) 354-2240

Refer to NPO-19682, volume and number of this NASA Tech Briefs *issue, and the page number.*

Elevation Corrections for Absolute-Pressure Measurements

Potential applications include process controls and scientific experiments.

Lewis Research Center, Cleveland, Ohio

A method of correcting absolute-air-pressure measurements for small differences in the elevations of pressure taps and pressure transducers has been devised. The variation in air pressure with elevation is well documented; nevertheless, in such disciplines as process control and laboratory experimentation, it has been common practice to account for pressure differences associated only with large differences in elevation along tubes that connect pressure taps to transducers. The emergence of highly accurate multiport pressure-measurement systems, coupled with the need for increasingly accurate pressure measurements, has made it necessary to correct for pressure differences associated with elevation differences as small as a meter or so. The present method can be readily incorporated into future pressure-measurement procedures to provide the necessary corrections; it can also be used to reprocess previous measurements to increase their accuracy.

The method is based on the fact that pressure at the bottom of a measurement tube will be higher than the pressure at the top due to weight of the column of air in the tube. It is assumed that the fluid (air) is at a static equilibrium and that the temperature and the gravitational acceleration do not vary significantly over the measured height. The resulting equation for correcting a pressure reading is

$$P = P_0 e^{-(g\rho_0/P_0)y}$$

where P is the pressure at the pressure tap (the corrected or actual pressure, which one seeks), P_0 is the reading of the pressure transducer, g is the gravitational acceleration, ρ_0 is the known density of air at the known temperature and pressure P_0, and y is the difference in elevation from the transducer to the pressure tap. At 20 °C, $g = 9.8$ m/s^2, $\rho_0 = 1.205$ kg/m^3, and $P_0 = 1.01325 \times 10^5$ Pa; therefore,

$$P = P_0 e^{(-1.16546 \times 10^{-4})y}$$

The method was tested in a series of measurements in air at a temperature of 70 ± 5 °F (≈21 ± 3 °C) on two commercial pressure gauges at various pressures and elevations. After corrections for biases between the two gauges, the results (see figure) indicate that the predicted and measured variations of pressure with height agree with each other to within 0.001 psi (≈7 Pa).

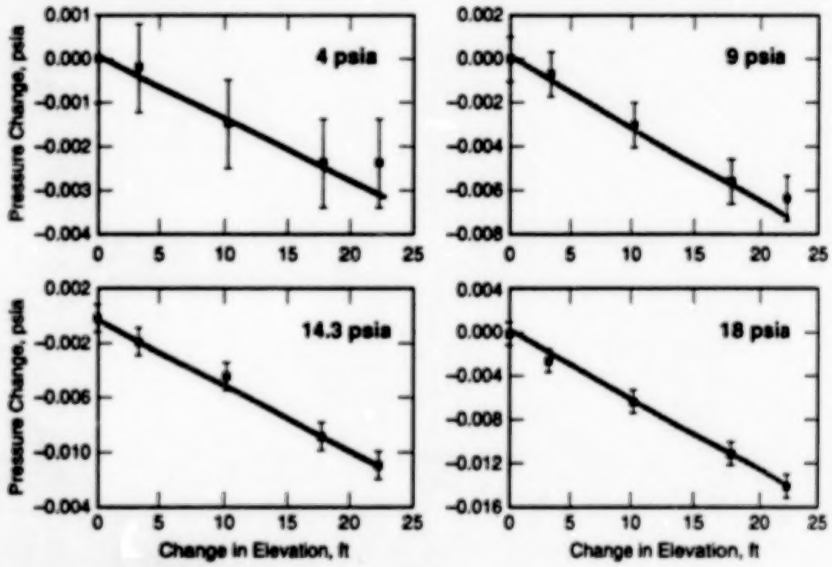

Calculated and Measured Changes of Pressure agreed with each other within the range of nonrepeatability of the pressure-gauge readings [about 0.001 psi (≈7 Pa)].

This work was done by Joseph W. Panek and Mark R. Sorrells of **Lewis Research Center**. *Further information is contained in a TSP [see page 1].*

Inquiries concerning rights for the commercial use of this invention should be addressed to NASA Lewis Research Center, Commercial Technology Office, Attn: Tech Brief Patent Status, Mail Stop 7-3, 21000 Brookpark Road, Cleveland, Ohio 44135. Refer to LEW-16499.

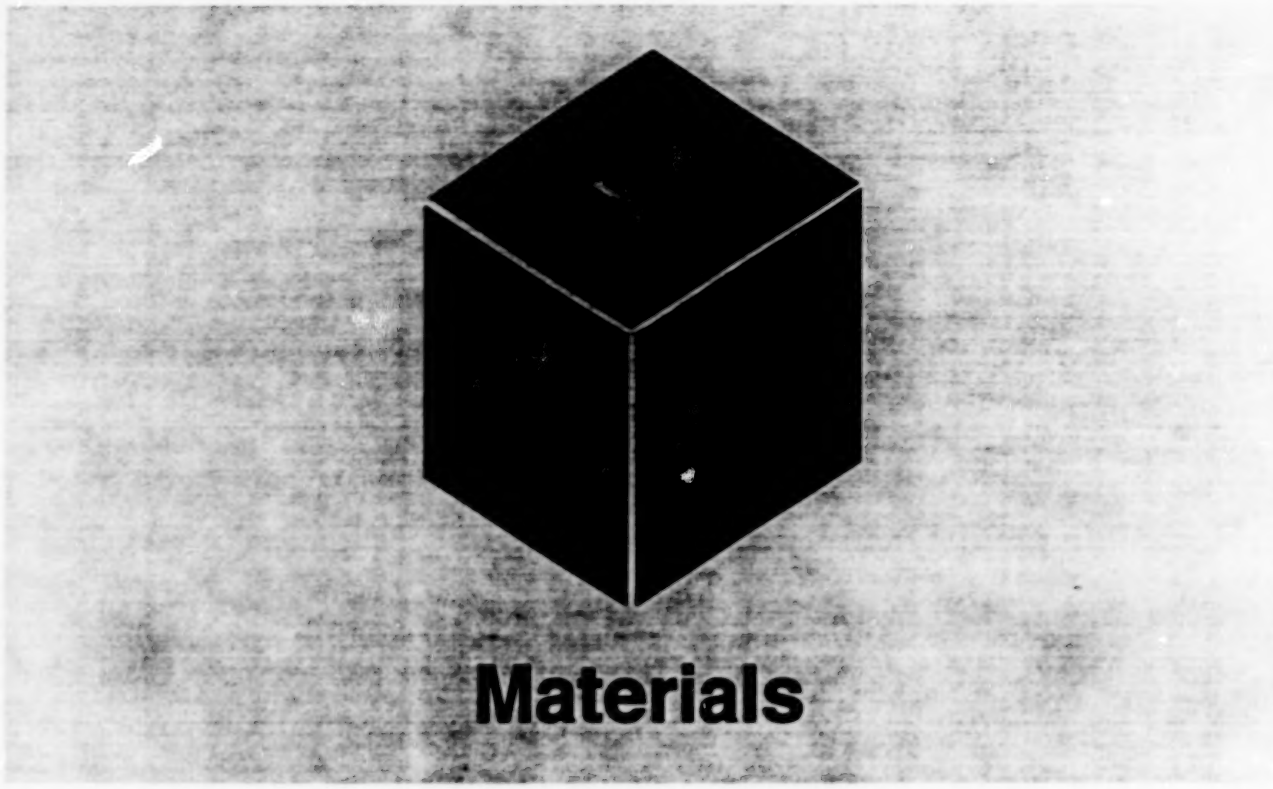

Materials

Hardware, Techniques, and Processes

33 Highly Selective Gas-Phase Etching of Silicon

33 High-Performance Thermal Insulation for a Racing Car

34 Testing Corrosion Prevention in Reinforced Concrete

Books and Reports

35 Phospha-s-Triazines and Other Compounds for Use as Additives

BLANK PAGE

Highly Selective Gas-Phase Etching of Silicon

CMOS integrated-circuit chips can be micromachined to incorporate microsensors.

NASA's Jet Propulsion Laboratory, Pasadena, California

A technique of gentle, highly selective gas-phase etching of silicon has been devised to enable the fabrication of microelectromechanical devices integrated with electronic circuits. For example, newly fabricated complementary metal oxide/semiconductor (CMOS) integrated-circuit chips can be micromachined by use of this technique to incorporate microsensors, without damaging the circuitry already present.

The technique is based on the fact that at room temperature, xenon difluoride (XeF_2) gas etches silicon preferentially to almost all other materials that are likely to be encountered in processing of semiconductor devices. Even when silicon is etched by XeF_2 to a depth of hundreds of microns, there is no appreciable etching of adjacent uncured or cured photoresist, oxide, metal, or polymeric structures with dimensions down to fractions of a micron.

Another notable advantage of gas-phase etching with XeF_2 is that unlike liquid-phase etching, it does not involve hydrodynamic forces that could damage fragile micromechanical structures like those shown in the figure. Still another advantage of etching with XeF_2 is that since it can be done at room temperature, there is no risk of the diffusion that can occur at high temperature, ruining the devices being fabricated.

At room temperature and atmospheric pressure, XeF_2 is a white solid. However, at room temperature, it sublimates at a vapor pressure of several torr (several hundred pascals). Thus, XeF_2 can easily be converted to the gas phase by placing it in a vacuum system of modest capability.

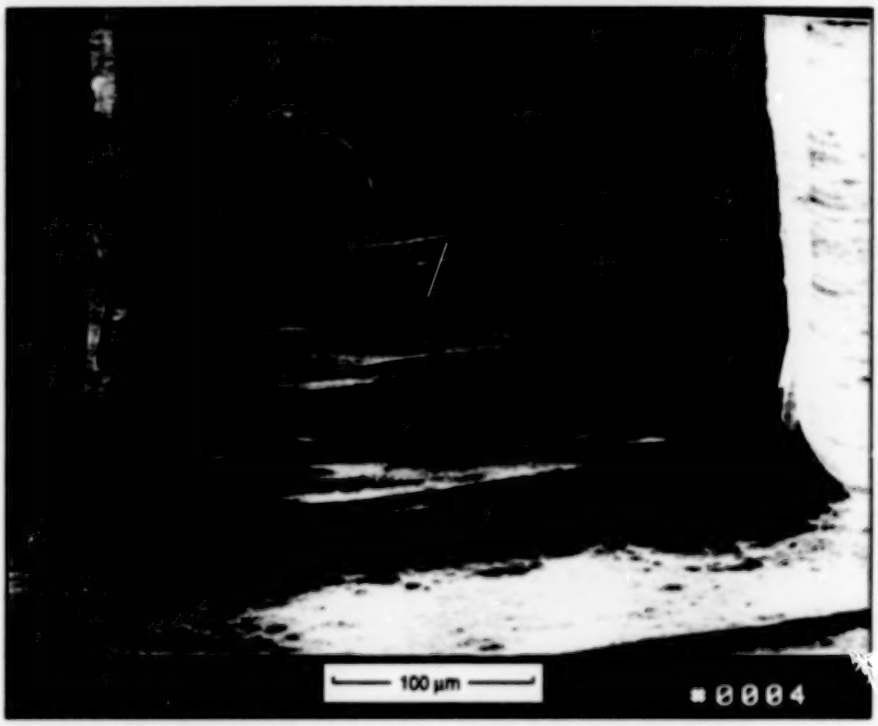

Microscopic SiO_2 Plates and Beams were fabricated in place on a silicon substrate, then suspended over a pit in the substrate by using XeF_2 gas to etch the silicon out from under them. Aluminum pads are visible at the upper right.

Etching by XeF_2 is performed in a chamber connected by valves to a vacuum pump and to a source of XeF_2. First, the chamber is pumped down to a pressure of a few millitorr (a few tenths of a pascal). Then the valve to the source of XeF_2 is opened and adjusted to maintain the pressure in the source at about 1 torr (≈ 133 Pa), so that XeF_2 gas is released at a suitable rate and concentration. Under these conditions, etching of single-crystal silicon has been observed to proceed at typical rates between 3 and 5 μm/min, and occasionally at rates as high as 10 μm/min. The etch is nearly isotropic and insensitive to the type and concentration of dopant.

This work was done by Michael H. Hecht of Caltech and Kristofer S. Pister and Ezekiel Kruglick of UCLA for **NASA's Jet Propulsion Laboratory**. *Further information is contained in a TSP [see page 1].*
NPO-19902

High-Performance Thermal Insulation for a Racing Car

Space-shuttle-type insulating blankets can protect a driver against hotspots.

John F. Kennedy Space Center, Florida

Thermal-insulation blankets developed for use aboard the space shuttle can be adapted to a racing car to protect the driver against excessive cockpit heating. [Also see an earlier article under "Mission Accomplished," *NASA Tech Briefs*, Vol. 20, No. 8 (August 1996) page 20.] Thermal protection for the driver is necessary because, unlike the passenger compartment of a conventional automobile, the cockpit of a racing car is subject to intense heating as a result of unique racing-design features.

In particular, the exhaust pipes are routed so close to the sheet metal of the floor pan and transmission tunnel that a significant portion of the heat radiated by the exhaust system (at a power density of about 12 kW/m²) enters the cockpit, and even at high speed, the airflow is so limited that the cockpit is not cooled to a comfortable or even a safe temperature. Hotspots can develop near the driver's right foot and under the driver's seat. In the absence of thermal protection, a driver can sustain localized second- or third-degree burns. Although a cooling suit can be used to protect the driver, it adds undesired complexity and weight. In addition, a malfunction in the active cooling system could result in active heating of the driver.

Space-shuttle-type insulating blankets offer effective passive thermal pro-

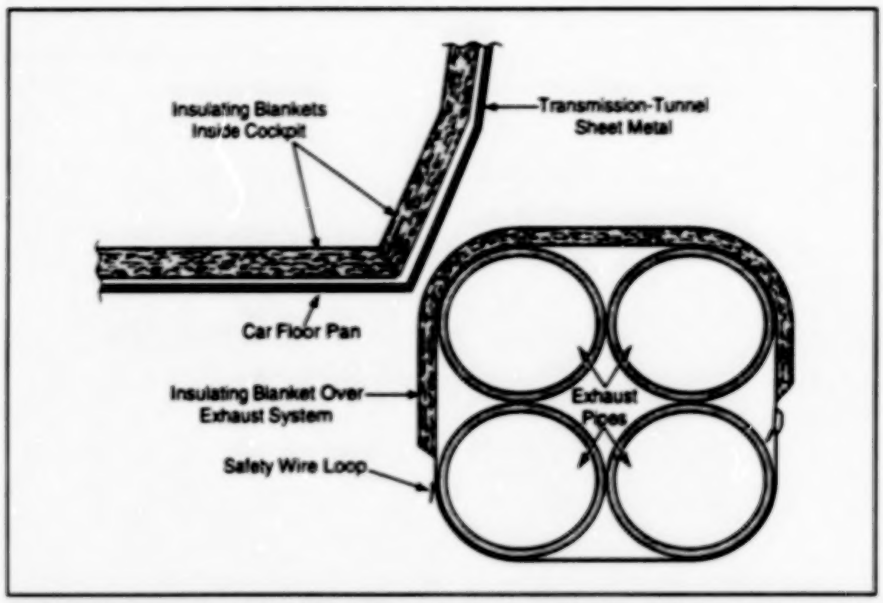

High-Performance Insulating Blankets made of spacecraft-grade materials can be used to prevent excessive transfer of heat from exhaust pipes to the interior of a racing-car cockpit.

tection, without contributing excessively to complexity or weight. The insulating blankets are of three different types: one type for installation on the exhaust and tailpipes, the other two types for installation in the cockpit. The exhaust-system blankets are made partly of a material called "advanced flexible reusable surface insulation" (AFRSI), which comprises a ceramic microfiber core between two glass-fabric face sheets quilted with a ceramic thread. The AFRSI of each blanket is covered with an outer nickel-alloy foil 0.001 in. (25 μm) thick. The foil cover is designed to increase the durability of the blanket, provide some shielding against radiation, and provide for mechanical attachment to enable safety wiring of the blanket to the exhaust-system components. The foil shell is closed along the edge of the blanket by a single fold (followed by rolling) and secured with stainless-steel staples. The single fold is designed to minimize thermal conduction while providing adequate strength. Grommets provide additional reinforcement for the seams and serve as attachment fixtures.

The blanket is contoured to the compound curves of the exhaust-system components. The entire blanket is less than 0.5 in. (1.3 cm) thick, yet acts as a highly efficient thermal-radiation shield with low thermal conduction. To prevent overheating of the exhaust and tailpipes, the blanket is installed only over the top of the exhaust system, leaving the bottom exposed to airflow. Because the blanket is made solely of metal, ceramic, and glass, it is nonflammable and does not outgas significantly during use.

The blankets of first cockpit-interior type are placed under the driver's seat and in floor areas to the left of the seat. Each blanket comprises a (1) a core of low-density, highly resilient glass-microfiber mat between 1 and 2 in. (between 2.5 and 5.1 cm) thick enclosed in (2) a radiation-barrier shell made from layers of an aluminized high-temperature-resistant film and sealed by a high-temperature-resistant adhesive tape, all enclosed in (3) a durable outer shell made of glass cloth impregnated with polytetrafluoroethylene (space-suit material).

The blankets of the second cockpit-interior type are used to insulate the transmission-tunnel/foot-well area. These blankets are made from AFRSI 0.5 in. (1.3 cm) thick, enclosed in glass cloth impregnated with polytetrafluoroethylene. AFRSI was chosen because of its ability to maintain known thickness over a range of compressive loads. The polytetrafluoroethylene-impregnated glass cloth provides durability. The blankets of both cockpit-interior types are designed to be lightweight, to provide maximum thermal insulation, to be nonflammable, and to provide additional protection to the driver in the event of a collision or fire.

This work was done by Bruce V. Lockley of **Kennedy Space Center** *and Martin J. Wilson, Jean M. Charvet, and Suzanne M. Hodge of Boeing. Further information is contained in a TSP [see page 1].*

Inquiries concerning rights for the commercial use of this invention should be addressed to the Patent Counsel, Kennedy Space Center [see page 1]. Refer to KSC-11938.

Testing Corrosion Prevention in Reinforced Concrete

An accelerated-testing method has been developed for evaluating the effectiveness of various measures taken to prevent the corrosion of steel reinforcing bars ("rebars") cast into concrete. Such measures can include chemical admixtures incorporated into the concrete, coatings, penetrants, modified concretes, new reinforcing materials, and corrosion-inhibiting chemicals that migrate after being applied. The method is an improvement of standard G 109-92 of the American Society for Testing and Materials (ASTM). In preparation for testing, concrete blocks are cast with rebars inside, along with any appropriate corrosion inhibitor(s). Holes are drilled into the blocks for measurement of electrical potentials at interior locations; other holes are drilled to promote intrusion of saltwater. During exposure of a block to a saltwater or other corrosive environment, electrical potentials are measured at rebars as well as in holes. Corrosion currents are also measured, and polarization resistances are determined. Optionally, potentials can be applied to accelerate corrosion. At the end of a test, the blocks are broken for visual examination of the rebars.

This work was done by Rupert U. Lee of **Kennedy Space Center** *and Joseph J. Curran of Dynacs Engineering Co., Inc. Further information is contained in a TSP [see page 1].*
KSC-11932

Books and Reports

Phospha-s-Triazines and Other Compounds for Use as Additives

A report describes research on selected compounds as additives to perfluoroalkylether (PFPAE) fluids that are used as synthetic lubricants for metal parts. Additives are needed to inhibit both thermo-oxidative degradation of, and corrosion of metals by, the PFPAE fluids in the presence of oxidizing atmospheres. [An earlier phase of this research was reported in "Performance of Perfluoroalkylether Lubricant System" (LEW-15603), *NASA Tech Briefs*, Vol. 19, No. 9 (September 1995), page 123.] The phase of research described in the present report included (1) synthesis of novel phospha-s-triazines, phosphate esters, and related additive compounds and (2) evaluation of these and previously available additives with respect to degradation- and corrosion-inhibiting behavior and thermal and hydrolytic stability, in an effort to develop a data base of optimum PFPAE/additive/alloy combinations. The other materials included in the study were six different alloys and four commercial PFPAEs. None of the additives tested was found to undergo hydrolysis at a temperature of 100 °C. The phosphate esters were found to be the most effective and, in particular, were fully effective in arresting the degradation of the PFPAEs in the presence of metal alloys and oxygen at temperatures up to 300 °C. In an overall rating, the additives in order of decreasing effectiveness were found to be phosphates > phosphate/diester mixture > phosphine ≥ phospha-s-triazines.

This work was done by K. J. L. Paciorek of Lubricating Specialties Co. for **Lewis Research Center**. *To obtain a copy of the report, "Phospha-s-Triazines and Related Compositions of Improved Hydrolytic and Thermal Stability," see TSP's [page 1].*

Inquiries concerning rights for the commercial use of this invention should be addressed to NASA Lewis Research Center, Commercial Technology Office, Attn: Tech Brief Patent Status, Mail Stop 7–3, 21000 Brookpark Road, Cleveland, Ohio 44135. Refer to LEW-16561.

BLANK PAGE

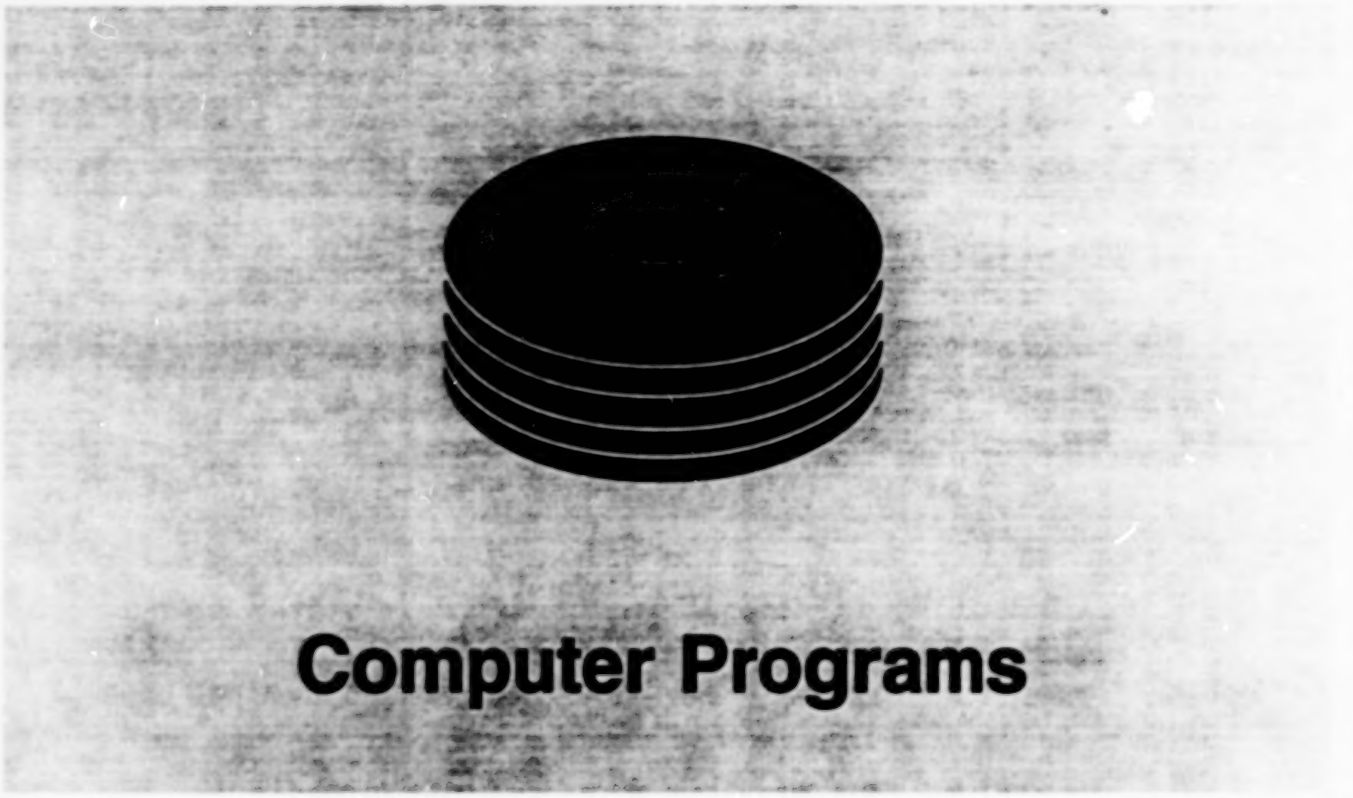

Computer Programs

Physical Sciences

39 Software for Processing SAR Images of the Polar Oceans

Mechanics

39 Program for Simulating Dynamics of Multibody Systems

Mathematics and Information Sciences

39 Software for Development of Spacecraft-Simulation Programs

39 Software for Tracking the Performance of Other Software

40 Software for Scheduling Use of Shared Resources

BLANK PAGE

Computer Programs

These programs may be obtained from COSMIC. Please contact

COSMIC®
Computer Services Annex
University of Georgia
Athens, GA 30602
Telephone No. (404) 542-3265.

Physical Sciences

Software for Processing SAR Images of the Polar Oceans

The RADARSAT/ERS-1,2 Geophysical Processor System (RGPS) is an automated system of hardware and software that processes synthetic-aperture-radar (SAR) images of ice and open water in polar oceans to generate higher-level geophysical-data products. Information in such products includes the age and thickness of ice and the onset of melting or freezing. They are all computed by algorithms contained in the RGPS software. In addition to the SAR image data themselves, meteorological fields are used in the analysis of the SAR imagery; therefore, interfaces with external meteorological sources have been established to capture meteorological data. The RGPS is intended to be installed as a subsystem of the Alaska SAR Facility (ASF), though testing of the RGPS had not yet been completed at the time of reporting the information for this article. In operation as subsystem of the ASF, the RGPS would be able to place requests for acquisition of raw SAR data and for preprocessing of those data by other hardware and software, would ingest the preprocessed data, would generate its standard data products routinely, and would deliver these products to an archive for long-term storage and distribution. In addition to the aforementioned geophysical data products generated from SAR imagery, the RGPS would also produce daily surface-pressure, wind, and temperature data on a gridded field.

This program was written by Ronald Kwok, Shirley Pang, Amy Rodgers, and Glenn Cunningham of Caltech for **NASA's Jet Propulsion Laboratory**. *No further documentation is available.*

This software is available for commercial licensing. Please contact Don Hart of the California Institute of Technology at (818) 393-3425. Refer to NPO-20021.

Mechanics

Program for Simulating Dynamics of Multibody Systems

The Dynamics Algorithms for Real-Time Simulation (DARTS) computer program solves the equations of motion of tree-topology, flexible, and/or multibody mechanical systems as diverse as molecules, mechanisms, robots, spacecraft, and ground vehicles. It has proven to be particularly useful for real-time simulation of the dynamics of spacecraft. DARTS enables the use of high-fidelity mathematical models of the dynamics of spacecraft, without sacrificing simulation speed. DARTS is based on state-of-the-art algorithms from the spatial-operator-algebra formulation for multibody dynamics. This formulation, which has been reported in a number of previous issues of *NASA Tech Briefs*, was developed expressly for modeling the dynamic behavior of complex, articulated collections of bodies (principally, multiple-link robot arms) that interact with each other in free space or in contact with other bodies in the environment. Both DARTS and the Dshell software described in the preceding article have been executed on a variety of UNIX and VxWorks platforms.

This program was written by Abhinandan Jain, Guillermo Rodriguez, and Guy K. Man of Caltech for **NASA's Jet Propulsion Laboratory**. *Further information is contained in a TSP [see page 1].*
NPO-20168

Mathematics and Information Sciences

Software for Development of Spacecraft-Simulation Programs

DARTS Shell (Dshell) is a multimission spacecraft simulator for the development, integration, and test of flight software and hardware. Dshell reduces the time and cost of developing simulation programs by enabling the development of the software in modular, reusable form and by providing a host of generic capabilities that simplify the development process and enhancing run-time usability. Dshell combines (1) the DARTS program (described in the preceding article), which is a computational engine that solves equations for the flexible dynamics of both spacecraft and nonspacecraft multibody systems with (2) libraries of mathematical models for such hardware items as actuators, sensors, motors, and encoders into (3) an integrated simulation-environment software system that can be easily configured and interfaced with flight software and hardware according to requirements for various real- and non-real-time simulations. Dshell is portable from desktop computer workstations to real-time, hardware-in-the-loop simulation environments. Dshell is in use by several of NASA's projects, including Cassini, Galileo, Mars Pathfinder, and several projects in the Flight System Testbed at NASA's Jet Propulsion Laboratory.

This program was written by Abhinandan Jain and Jeffrey Biesiadecki of Caltech for **NASA's Jet Propulsion Laboratory**. *Further information is contained in a TSP [see page 1].*
NPO-20248

Software for Tracking the Performance of Other Software

The Flight Software Memory Tracker (FMT) computer program is a collection of utility subprograms developed for use on the ground to track images of the flight software (FSW) in the computers aboard the Cassini spacecraft. [As used here, "images" signifies both (1) the memory load and updatable parameters in the spacecraft computers and (2) logically equivalent representations thereof.] FMT maintains a history of every FSW image aboard the spacecraft ("FSW image" for short), updating the ground copies of the images ("FMT images" for short) whenever the FSW images are updated. When FSW images are updated by uplink commands transmitted to the spacecraft, FMT can translate the commands into update data groups to be appended to

FMT images. FMT images can also be updated by readout from spacecraft computer-memory addresses, which readout is performed in addition to normal telemetry downlink. FMT can also generate commands to update both FSW and FMT images at a specified time. The FMT images can be evaluated at any historic time, can be queried for history and statistics, and can be processed to obtain, for example, human-readable values of parameters in engineering units. FMT, which is written in Java, can be ported to computers, with various architectures and operating systems, that are equipped with Java interpreters.

This program was written by Edwin Kan, Allan Wax, and Hal Uffelman of Caltech for **NASA's Jet Propulsion Laboratory**. *Further information is contained in a TSP [see page 1].*
NPO-20200

Software for Scheduling Use of Shared Resources

The Quick Utility for Intelligence Planning and Scheduling (QUIPS) computer program automates the scheduling of resources that must be shared among multiple tasks or groups. Designed to aid coordination of military intelligence operations at the division and brigade levels, QUIPS might also prove useful in coordinating other large-scale operations in which resources and tasks are dispensed to various locations. QUIPS generates one primary display to show all resources on a battlefield or other area of interest, the statuses of the resources, and timeliness for their availability. A graphical user interface enables the user to point and click instead of type, thereby reducing the user's workload and increasing efficiency. In the original military application, QUIPS is coupled with the Tactical Movement Analyzer (TMA) and Sensor Placement Analyzer (SPA) programs to create an end-to-end asset-management software module. TMA digests data on roads, rivers, railroads, urban areas, vegetation, and elevation to produce a picture that helps a military analyst determine the possibilities for movement by enemy and friendly forces. SPA helps in determining the most effective locations for placing a limited number of sensors, taking account of the area that could be covered by each sensor at a given location, and of effects of weather, terrain, and distance on the propagation of radio signals to and from the sensors.

This work was done by Nora Mainland, Kurt Stadsklev, and Paul Maglio of Caltech for **NASA's Jet Propulsion Laboratory**. *Further information is contained in a TSP [see page 1].*

This software is available for commercial licensing. Please contact Don Hart of the California Institute of Technology at (818) 393-3425. Refer to NPO-20207.

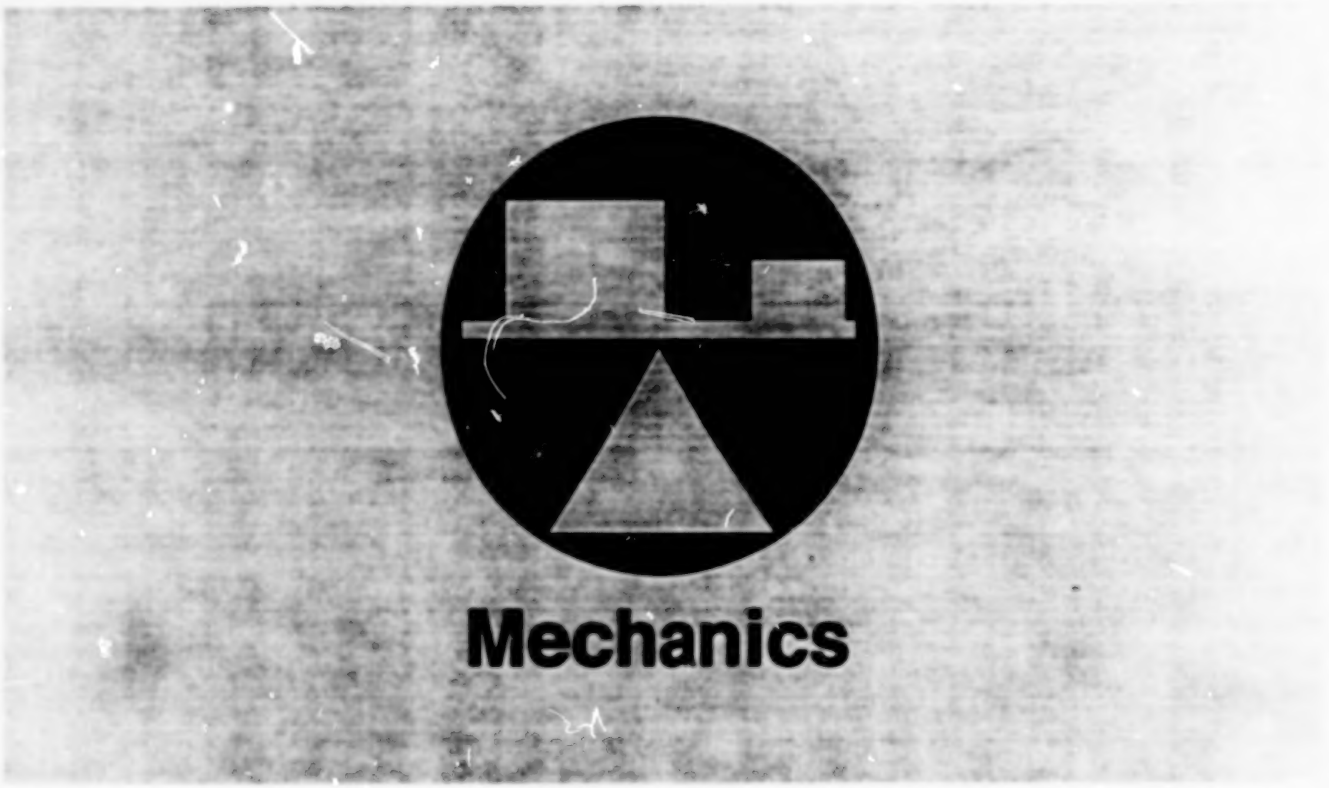

Hardware, Techniques, and Processes

43 Passive Magnetic Bearings With Ferrofluid Stabilization
44 Latch-Release Pin Puller With Shape-Memory-Alloy Actuator
45 High-Wind Masts for Meteorological Instruments
46 Self-Contained Impact-Type Damper for Bellows-Type Face Seals

BLANK PAGE

Passive Magnetic Bearings With Ferrofluid Stabilization

Sizes, weights, and power consumptions can be reduced.

Lewis Research Center, Cleveland, Ohio

Permanent-magnet rotary bearings with ferrofluid stabilization in the axial degree of freedom are undergoing development. These bearings are totally passive, yet stable in all degrees of freedom. In contrast, previously developed electromagnet and permanent-magnet bearings all exhibit instability in at least one degree of freedom, giving rise to the need for active electronic feedback and power-control circuitry. By making active control unnecessary, ferrofluid stabilization can enable reductions in the overall sizes, weights, and power consumptions of machines that contain permanent-magnet bearings. Unlike passive magnetic bearings based on superconductivity, which are restricted to operating temperatures far below room temperature, the developmental bearings are designed to function at temperatures from 0 to 50 °C.

Figure 1 contains a simplified drawing of a shaft with typical conventional permanent magnet bearings near both ends. The repulsion between like magnetic poles of the rotor and stator portions of each bearing give rise to a magnetic levitation that is stable in the radial degree of freedom but unstable in the axial degree of freedom.

Figure 1 also depicts an elementary ferrofluid stabilizer comprising a permanent magnet immersed in ferrofluid in a container. In the absence of externally applied force, the magnet seeks an equilibrium position that is approximately central in the body of ferrofluid. When the magnet is displaced from the equilibrium position, there arises a restoring force that, if not resisted, pushes the magnet back toward the equilibrium position; that is, the levitation is stable. However, in the configuration depicted here, the restoring force, and thus the load capacity, is too small to be useful. To obtain enough restoring force and load capacity for use in stabilizing a magnetic bearing along a specified axis, it is necessary to confine the ferrofluid in a restricted cavity and optimize the permanent-magnet geometry to increase the restoring force along that axis.

Figure 2 illustrates one of many possible configurations of a shaft equipped with magnetic bearings and with ferrofluid stabilizers designed to generate enough axial restoring force to counteract the axial instability of the magnetic bearings. A prototype of this configuration has been tested and found to be stable. The tests also revealed that magnetic bearings may be useful, to some extent, as vibration isolators.

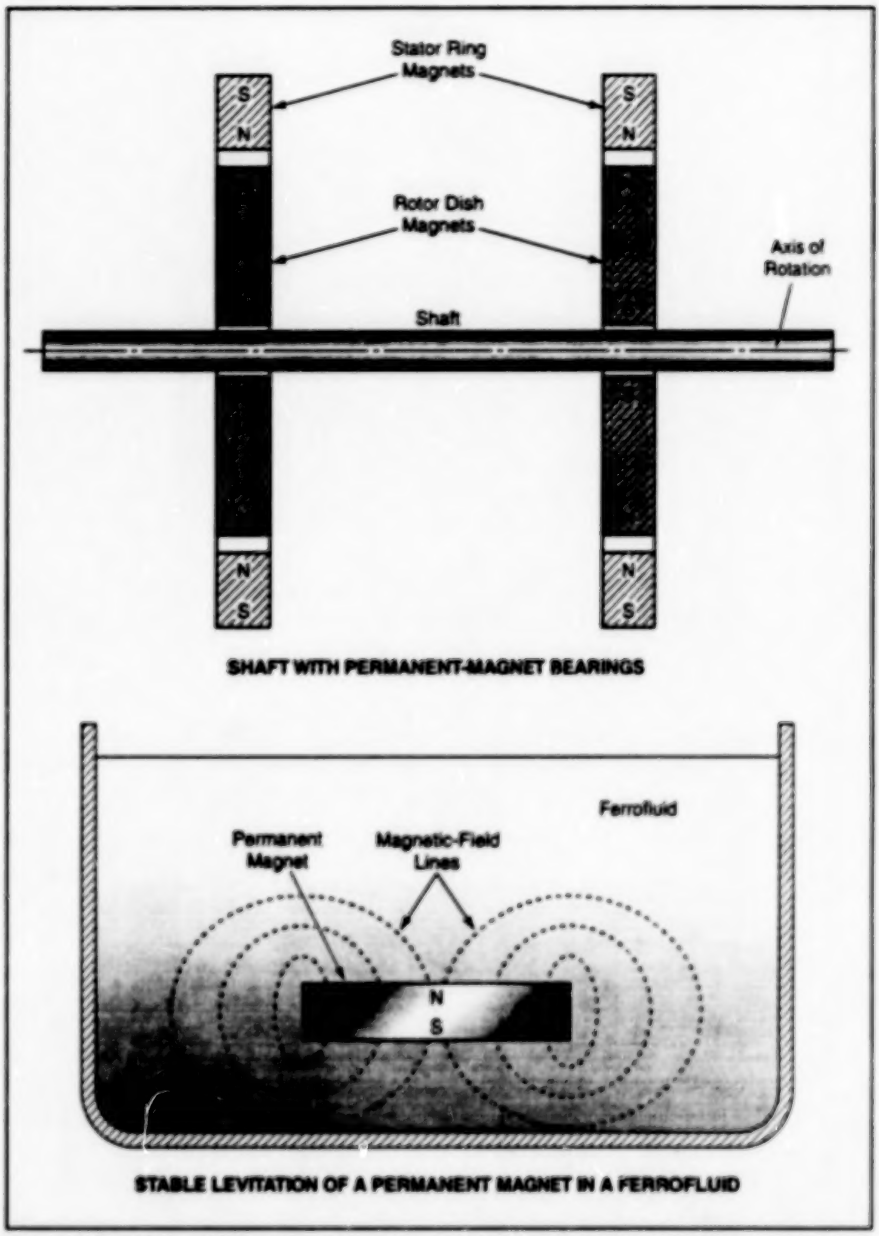

Figure 1. The Magnetic Bearings shown here provide radially stable, but axially unstable levitation. On the other hand, a permanent magnet immersed in a ferrofluid is levitated stably in three dimensions.

This work was done by Eliseo DiRusso of **Lewis Research Center** *and Ralph Jansen of Ohio Aerospace Institute. Further information is contained in a TSP [see page 1].*

Inquiries concerning rights for the commercial use of this invention should be addressed to NASA Lewis Research Center, Commercial Technology Office, Attn: Tech Brief Patent Status, Mail Stop 7–3, 21000 Brookpark Road, Cleveland, Ohio 44135. Refer to LEW-16450.

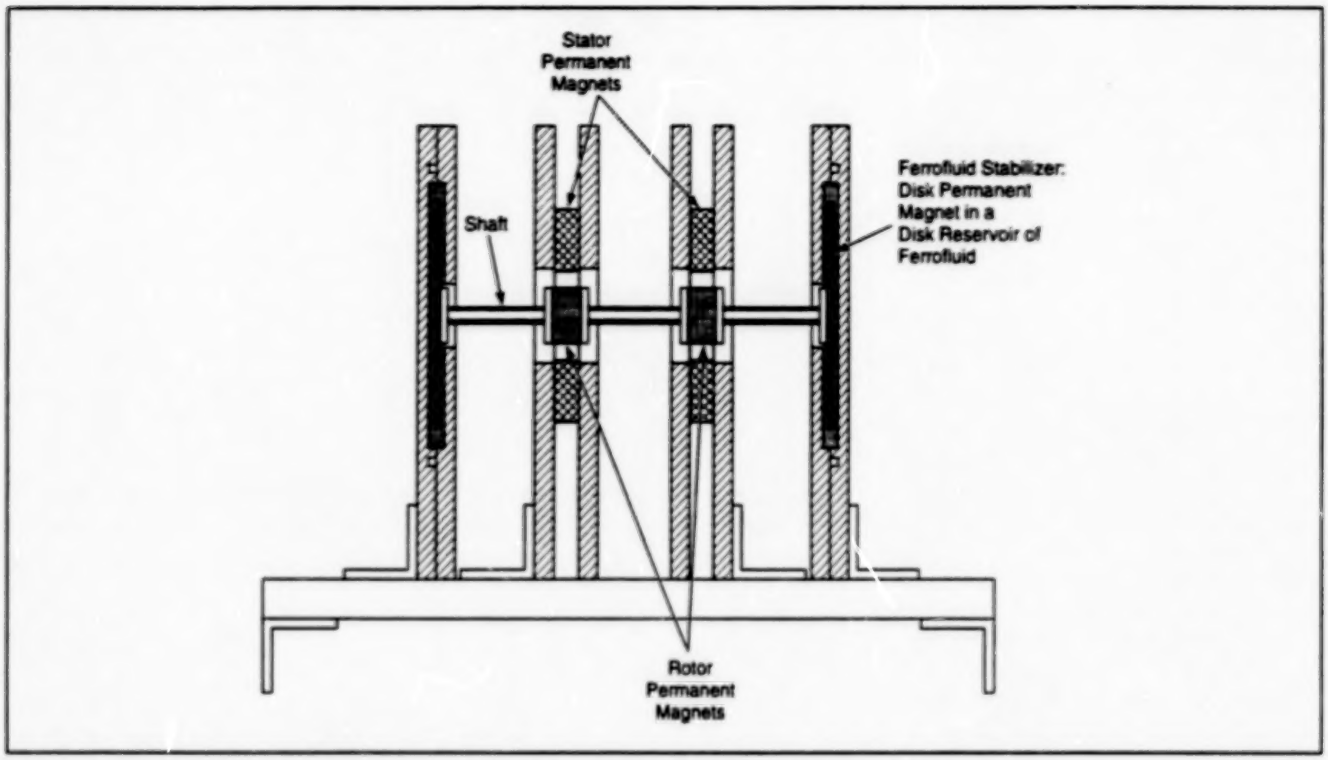

Figure 2. **A Shaft With Magnetic Bearings and Ferrofluid Stabilizers** is levitated stably in all degrees of freedom.

Latch-Release Pin Puller With Shape-Memory-Alloy Actuator

Reset can be accomplished manually or automatically by simply reextending the pin.

Lewis Research Center, Cleveland, Ohio

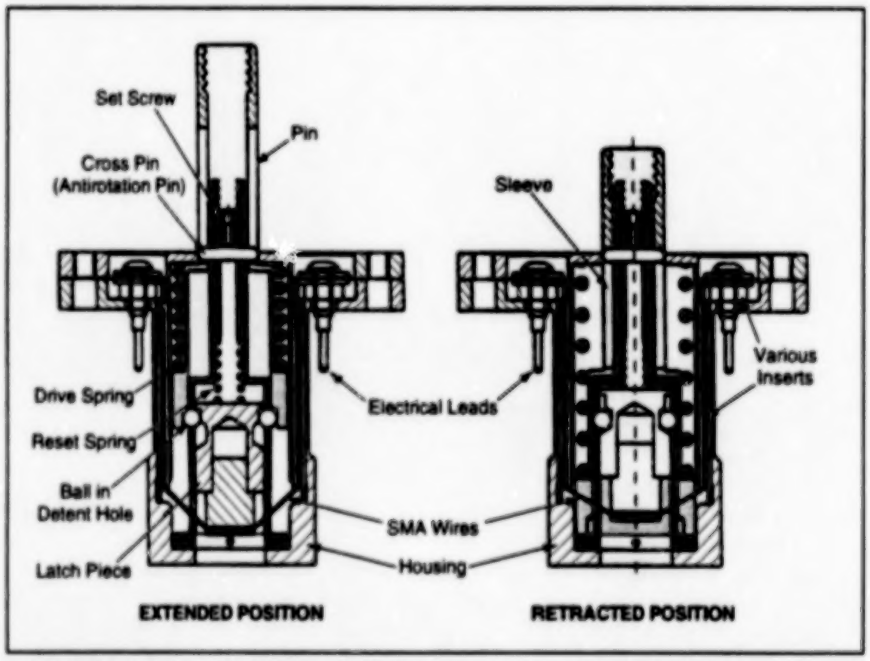

In this **SMA-Actuated Pin Puller**, the SMA wire serves as a trigger that releases potential energy stored in the driver spring.

The figure illustrates one of several related pin-puller mechanisms that harness the recovery characteristics of a shape-memory alloy (SMA). Like some other SMA-actuated mechanisms described previously in *NASA Tech Briefs*, this pin puller is suitable for use in place of a pyrotechnically actuated pin puller and can be operated under remote control to release a door and/or deploy a stowed object, for example. Unlike pyrotechnically actuated pin pullers, this and other SMA-actuated pin pullers can be reused.

The SMA component in this pin puller serves as a trigger to release potential energy stored in the driver spring. This spring biases the pin toward retraction (downward in the figure). However, under normal (nonactuation) conditions, the pin is set in the extended (uppermost) position and the ball-detent latch prevents retraction.

A component made of an SMA undergoes a pronounced deformation to a "remembered" shape when its temperature rises through a transition value, causing a transformation in its metallurgical structure from a martensitic to an austenitic phase. In this case, the SMA component is a wire, made of a nickel/titanium alloy denoted by the trade "Nitinol," that has been stretched. To initiate retraction of the pin, electric current is made to flow along the wire, thereby heating the wire above its transition temperature and causing it to shrink to its "remembered" (unstretched) length. The shrinkage of the wire pulls the

latch piece upward, against the downward bias of the reset spring. As a result, the balls are no longer forced to protrude through the detent holes. Thus, the balls no longer block the retraction of the pin.

Later, the mechanism can be reset by pulling on the pin to extend it. Provided that the SMA wire has cooled enough to recover its stretched length, the mechanism will remain reset because the reset spring biases the latch piece into its lowest position, where it forces the balls to protrude through the detent holes.

This work was done by Michael Bokaie of TiNi Alloy Co. for **Lewis Research Center**. *Further information is contained in a TSP [see page 1].*

Inquiries concerning rights for the commercial use of this invention should be addressed to NASA Lewis Research Center, Commercial Technology Office, Attn: Tech Brief Patent Status, Mail Stop 7-3, 21000 Brookpark Road, Cleveland, Ohio 44135. Refer to LEW-16511.

High-Wind Masts for Meteorological Instruments

The masts would be faired to minimize aerodynamic loading of the structures.

John F. Kennedy Space Center, Florida

Rigid, guyed masts of a proposed type for supporting meteorological instruments would be designed to withstand considerably stronger winds than those conventionally used. The proposed fairings would also help minimize perturbations of airflows and thereby minimize the contaminating effects of the masts on measurements taken by instruments mounted on the masts.

The masts would be constructed in modular sections, each 3.3 m long, that could be connected together to achieve the desired overall height. Typically, three sections would be used (see figure) to obtain the standard wind-sensor height of 10 m as specified by the World Meteorological Organization. The base of the mast would be mounted rigidly in the ground.

The main structural member in each section of a mast would be a cylindrical tube. The fairing would be a vertically finned, neutral-lift airfoil that would surround the tube. The airfoil would be free to pivot azimuthally around the tube to align itself with the wind as directed by the vertical fin section. The airfoil would pivot on bearings mounted on circular flanges at the ends of the tube. The circular flanges above each section would provide attachment points for guy wires. The flanges at the lower end of the sections could serve as bearing surfaces.

To minimize aerodynamic drag caused by vertical winds acting on the circular flanges, the size and shape of the flanges should be kept to a minimum but consistent with the need to provide clearance between the guy wires and the airfoils. The airfoil ends should be trimmed to eliminate mechanical interference with the flanges or guy wires. If there is a need for further reduction of the wind load on the entire structure, then the guy wires could also be faired with airfoils in a manner similar to that of the sections of the mast.

When a cylinder is faired with a neutral-lift airfoil which is free to pivot with the wind, the effect is equivalent to dividing the drag coefficient, diameter, or length of the cylinder by approximately a factor of 8. Conversely, it could be viewed as reducing the equivalent speed of the wind acting on the cylinder to $8^{-1/2}$ (≈1/2.8) of its actual value. This approach can result in substantial improvements of non-aerodynamically-faired conventional towers and masts, which can typically withstand winds of no more than about 125 mi/h (56 m/s). Simply by changing the structural members to self-aligning, neutral-lift airfoils, wind loads would be reduced enough to enable the structures to withstand winds up to 350 mi/h (156 m/s).

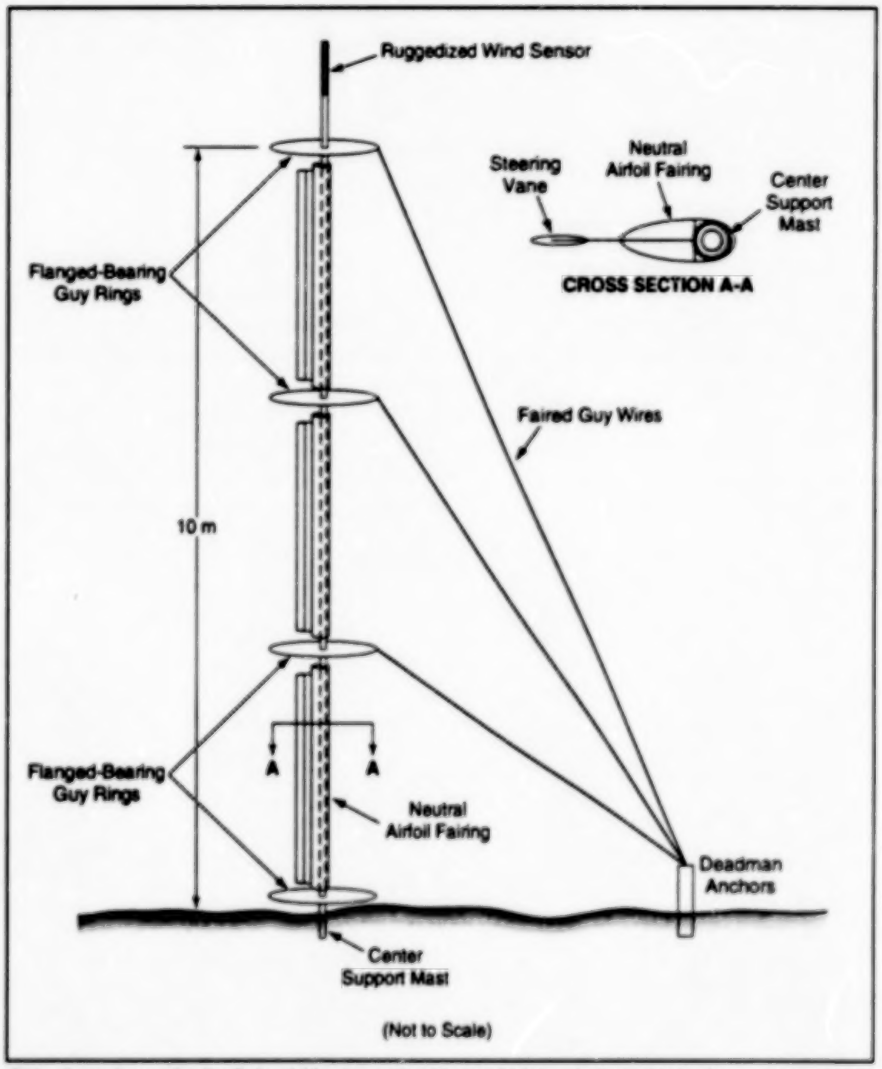

This Aerodynamically Faired Mast would withstand high winds and introduce minimal perturbations into the flow of air around the meteorological instrument(s) mounted on top.

This work was done by Jan A. Zysko of **Kennedy Space Center**. *Further information is contained in a TSP [see page 1].*

Inquiries concerning rights for the commercial use of this invention should be addressed to the Patent Counsel, Kennedy Space Center; (407) 867-6225. Refer to KSC-11741.

Self-Contained Impact-Type Damper for Bellows-Type Face Seals

This damper suppresses dynamic instability or chatter due to stick-slip phenomena and fluid vaporization.

Marshall Space Flight Center, Alabama

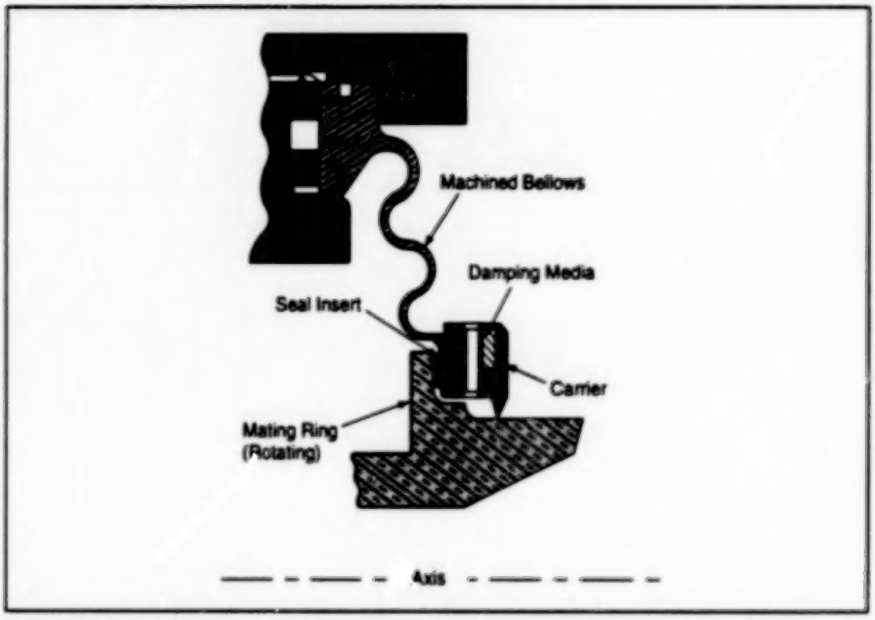

A Self-Contained Impact-Type Damper has been incorporated into an advanced bellows-type lift-off face seal in a high-pressure turbopump.

A self-contained impact-type damper for a bellows-type face seals suppresses dynamic instability or chatter. In current practice, damping in a typical seal is accomplished through rubbing contact between a ground (a stationary member) and a bellows or carrier as the seal translates. Usually, the rubbing contact occurs through a third member. This contact results in the potential for the carrier to seize, with consequent limitation of axial travel. It also makes for a complicated assembly, susceptible to assembly error.

The self-contained impact-type damper (see figure) consists of a damping medium contained in a pocket in an insert carrier. The medium consists of particles. The cavity is filled to less than its full volume with the particles, leaving some room for motion. Damping is accomplished when the particles impinge on each other and the cavity walls, absorbing energy from the carrier when it begins to vibrate.

This work was done by Richard James Kloepfer and Michael Howard Dills of UTC/Pratt & Whitney, Government Engines & Space Propulsion, for **Marshall Space Flight Center**. *Further information is contained in a TSP [see page 1].*
MFS-31188

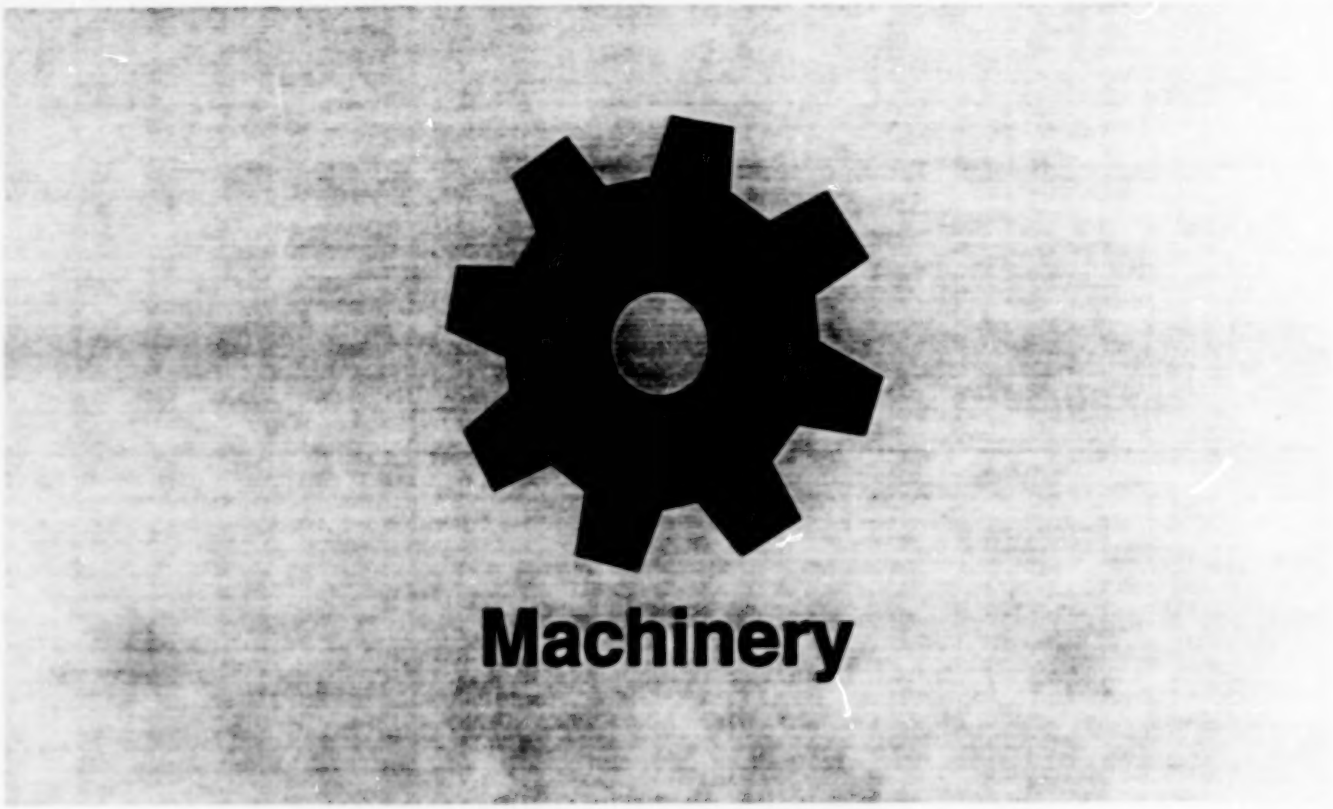

Hardware, Techniques, and Processes

49 Manipulator System for a Robotic Vehicle
49 All-Terrain Vehicle With Self-Righting and Pose Control

BLANK PAGE

Manipulator System for a Robotic Vehicle

Each manipulator arm performs multiple functions.

NASA's Jet Propulsion Laboratory, Pasadena, California

A prototype manipulator system that includes two different arms has been tentatively selected for use on a semiautonomous robotic vehicle called *Rocky 7* (see figure). [A previous version of this vehicle with a single manipulator arm was described in "High-Performance Robotic Vehicle" (NPO-19921) *NASA Tech Briefs*, Vol. 21, No. 1 (January 1997), page 67.] *Rocky 7* is the most recent one in a series of such vehicles that are candidates for use in future remotely controlled scientific exploration of the surface of Mars. In comparison with the *Sojourner* vehicle deployed on Mars from the Mars *Pathfinder* spacecraft in July 1997, *Rocky 7* would carry more scientific instrumentation and would function with greater autonomy, mobility, and capability for manipulation. The basic design of *Rocky 7* and the other vehicles in the series could also be adapted to such terrestrial uses as remote surveillance and/or manipulation in remote and/or hostile environments.

The joints in the two manipulator arms are back-driveable and feature modular, lightweight, high-torque, gearmotor-type actuators, which were described in "Actuators for Rapid Development of Prototypes of Robots" (NPO-20054), *NASA Tech Briefs*, Vol. 21, No. 3 (March 1997), page 94. Both the actuators and the arm segments are hollow; this makes it possible to use the insides of the actuators and arms as optical paths and to hold electrical wires for actuators and for scientific instruments.

Mounted on the outer end of the shorter arm are two scoops and an optical assembly. The scoops can be used to dig (to a depth of 10 cm), hold, and dump soil samples; they can also be used to grasp an instrument canister, e.g., for burying a seismometer. The total mass of the arm is 0.65 kg. The arm can carry a payload of as much as 1 kg in normal Earth gravity.

The optical assembly includes two mirrors, with a fiber-optic connection along the arm to a spectrometer housed in the vehicle chassis. The optical assembly constitutes the input optical device of the spectrometer, and is aimed by turning the arm. The optical aperture is open only when the scoops are rotated to the back-to-back position. A spectrometer-calibration target can be rotated into or out of the spectrometer field of view by rotating both scoops together through a full circle.

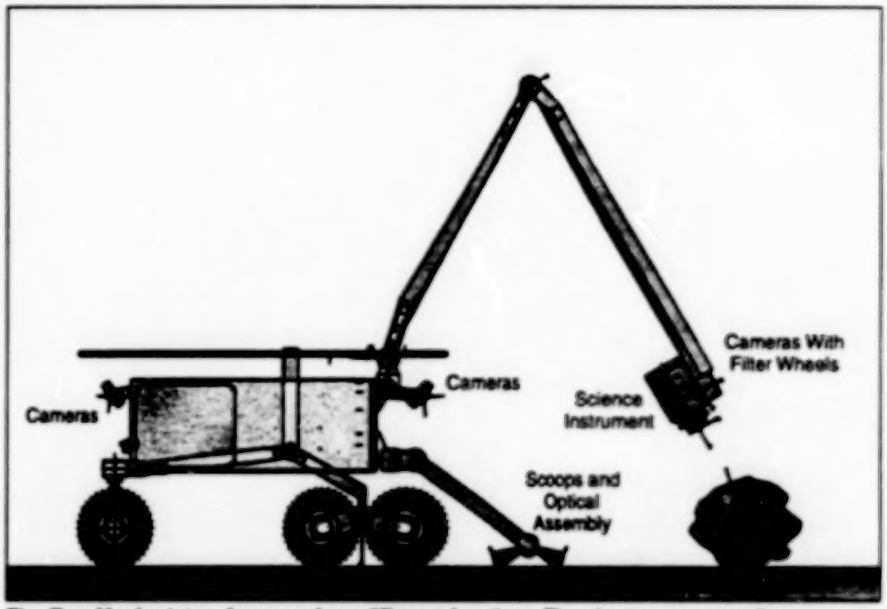

The Two Manipulator Arms perform different functions. The shorter arm can dig, grasp an object, or aim a spectrometer. The longer arm serves as a mast for stereoscopic, multispectral imaging, and as a mechanism for positioning a scientific instrument.

Mounted on the outer end of the longer arm is an integrated sensor package that contains the following: (1) two stereoscopic video cameras with counterrotating filter wheels, and (2) an instrument canister that can be outfitted with either a gimballed close-focus camera, Mössbauer spectrometer, nuclear magnetic resonance spectrometer, or other science instrument. The arm can be extended to a height of 1.4 m above ground; it can be used to rotate the cameras through a complete circle for panoramic imaging of the surrounding terrain, to position the cameras for viewing objects of scientific interest from above, or to position the cameras to inspect the vehicle. The total mass of the longer arm is 0.7 kg. The arm can carry a scientific instrument as massive as 0.5 kg in normal Earth gravity.

Both arms can be stowed compactly, without interfering with the suspension and wheel-drive mechanisms, with a solar photovoltaic panel that supplies the power for the vehicle, or with another stereoscopic camera system that is used to guide the vehicle across the terrain as well as image the activities of the arms. An onboard electronic control system is used to operate both the vehicle drive motors and the actuators in the manipulator arms; this system provides variable-rate motor control, detects errors in joint angles, prevents collisions of the arms with objects in the vicinity, controls contact of mast instruments with the target rock, analyzes images of potential digging areas to prevent futile attempts to dig in rock, and visually verifies successful manipulator operations.

This work was done by Richard Volpe, Timothy Ohm, Richard Petras, Richard Welch, J. (Bob) Balaram, and Robert Mev of Caltech for **NASA's Jet Propulsion Laboratory**. *Further information is contained in a TSP [see page 1].*

NPO-20162

All-Terrain Vehicle With Self-Righting and Pose Control

Wheels driven by gearmotors are mounted on pivoting struts.

NASA's Jet Propulsion Laboratory, Pasadena, California

A small prototype robotic all-terrain vehicle features a unique drive and suspension system that affords capabilities for self-righting, pose control, and enhanced maneuverability for passing over obstacles. The vehicle is designed for exploration of planets and asteroids, and could just as well be used on Earth to carry scientific instruments to remote, hostile, or otherwise inaccessible locations on the ground. The drive and suspension system enable the vehicle to perform such diverse maneuvers as flipping

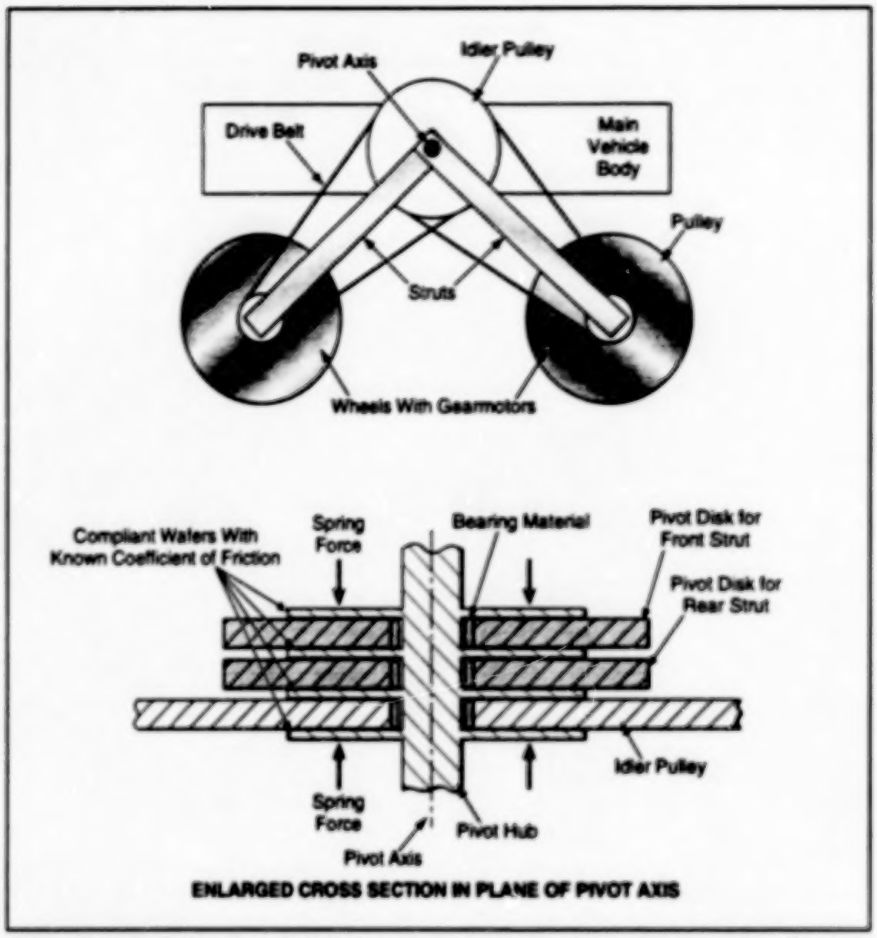

Each Wheel Is Driven by a dedicated gearmotor and is coupled to the idler pulley. The pivot assembly imposes a constant frictional torque *T*, so that it is possible to (a) turn both wheels in unison while both struts remain locked, (b) pivot one strut, or (c) pivot both struts in opposite directions by energizing the gearmotors to apply various combinations of torques *T*/2 or *T*.

itself over, traveling normal side up or upside down, orienting the main vehicle body in a specified direction in all three dimensions, or setting the main vehicle body down onto the ground, to name a few. Another maneuver enables the vehicle to overcome a common weakness of traditional all-terrain vehicles — a limitation on traction and drive force that makes it difficult or impossible to push wheels over some obstacles: This vehicle can simply lift a wheel onto the top of an obstacle.

The basic mode of operation of the vehicle can be characterized as four-wheel drive with skid steering. Each wheel is driven individually by a dedicated gearmotor. Each wheel and its gearmotor are mounted at the free end of a strut that pivots about a lateral axis through the center of gravity of the vehicle (see figure). Through pulleys or other mechanism attached to their wheels, both gearmotors on each side of the vehicle drive a single idler disk or pulley that turns about the pivot axis.

The design of the pivot assembly is crucial to the unique capabilities of this system. The idler pulley and the pivot disks of the struts are made of suitably chosen materials and spring-loaded together along the pivot axis in such a way as to resist turning with a static frictional torque *T*; in other words, it is necessary to apply a torque of *T* to rotate the idler pulley or either strut with respect to each other or the vehicle body.

During ordinary backward or forward motion along the ground, both wheels are turned in unison by their gearmotors, and the belt couplings make the idler pulley turn along with the wheels. In this operational mode, each gearmotor contributes a torque *T*/2 so that together, both gearmotors provide torque *T* to overcome the locking friction on the idler pulley. Each strut remains locked at its preset angle because the torque *T*/2 supplied by its motor is not sufficient to overcome its locking friction *T*.

If it is desired to change the angle between one strut and the main vehicle body, then the gearmotor on that strut only is energized. In general, a gearmotor acts as a brake when not energized. Since the gearmotor on the other strut is not energized and since it is coupled to the idler pulley, a torque greater than *T* would be needed to turn the idler pulley. However, as soon as the gearmotor on the strut that one desires to turn is energized, it develops enough torque (*T*) to begin pivoting the strut with respect to the vehicle body.

It is also possible to pivot both struts simultaneously in opposite directions to change the angle between them. To accomplish this, one energizes the gearmotors to apply equal and opposite torques of magnitude *T*: The net torque on the idler pulley balances out to zero, so that the idler pulley and body remain locked, while the applied torques are just sufficient to turn the struts against locking friction. If it is desired to pivot the struts through unequal angles, then the gearmotor speeds are adjusted accordingly.

The prototype vehicle has performed successfully in tests. Current and future work is focused on designing a simple hub mechanism, which is not sensitive to dust or other contamination, and on active control techniques to allow autonomous planetary rovers to take advantage of the flexibility of the mechanism.

This work was done by Brian H. Wilcox and Annette K. Nasif of Caltech for **NASA's Jet Propulsion Laboratory**. *Further information is contained in a TSP [see page 1].*

In accordance with Public Law 96-517, the contractor has elected to retain title to this invention. Inquiries concerning rights for its commercial use should be addressed to

Technology Reporting Office
JPL
Mail Stop 122-116
4800 Oak Grove Drive
Pasadena, CA 91109
(818) 354-2240

Refer to NPO-20057, volume and number of this NASA Tech Briefs *issue, and the page number.*

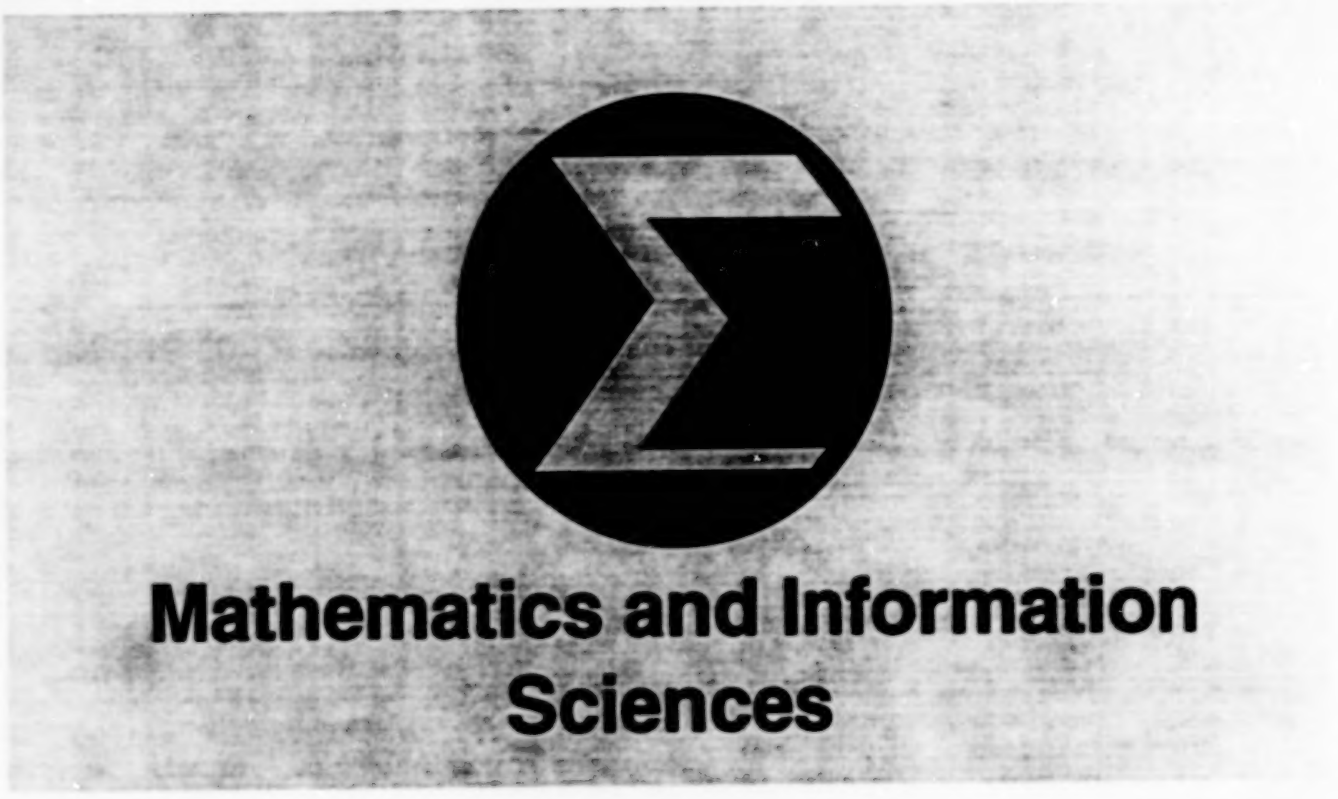

Mathematics and Information Sciences

Hardware, Techniques, and Processes

53 Consortium Benchmarking in a Competitive Environment
54 Diagnosing Helicopter Gearboxes Using Connectionist Networks
55 Software for Planning in a Hierarchical Processing Environment
55 Model for Investigating Human Factors in an Organization
57 Software for Improving Operational Processes
57 Work-Measurement and Methods-Analysis Studies of the OPF

BLANK PAGE

Consortium Benchmarking in a Competitive Environment

The best features of proven benchmarking models are combined in an innovative approach.

John F. Kennedy Space Center, Florida

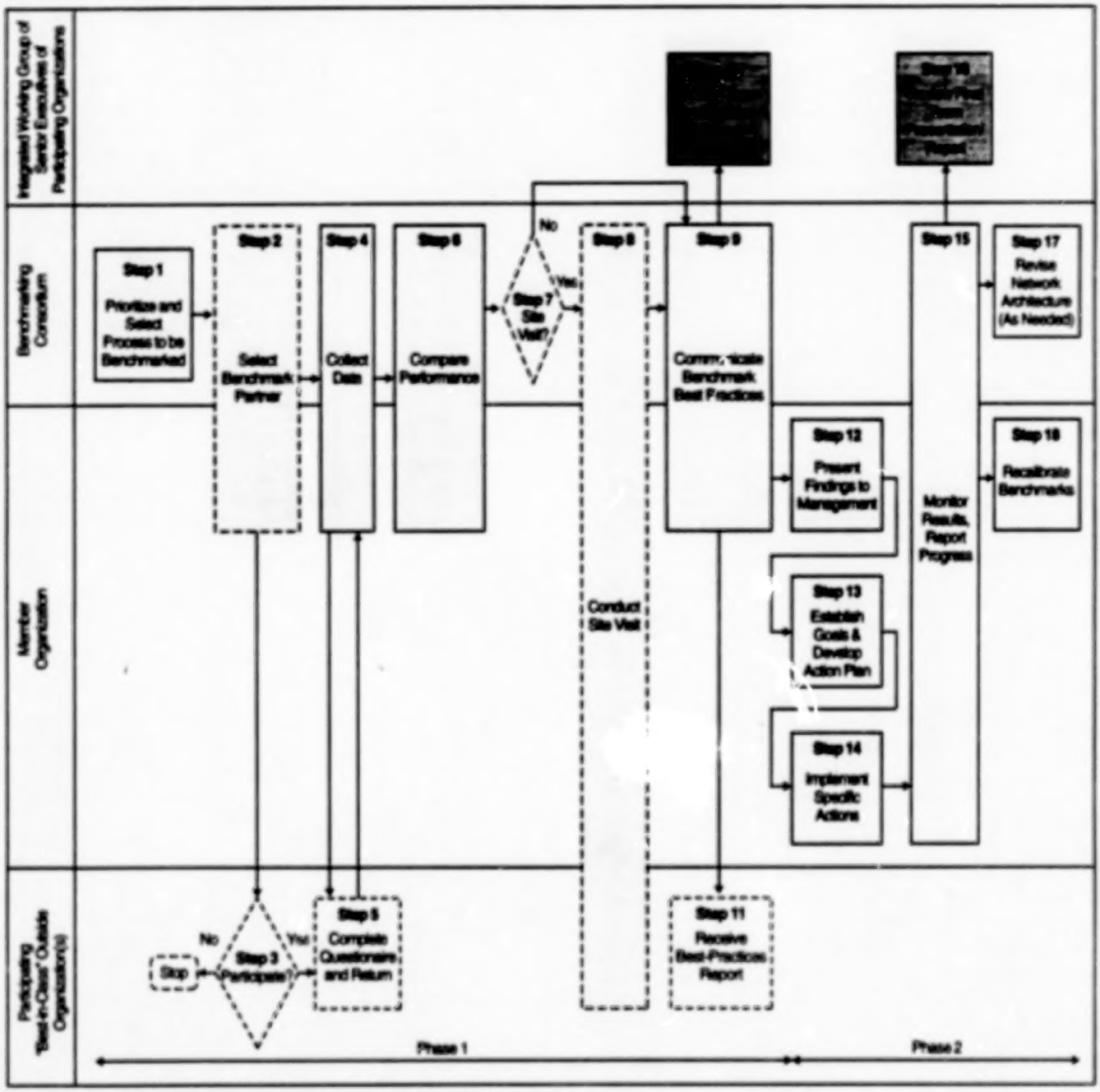

This Flow Chart depicts the steps of benchmarking according to the KBC model.

The Kennedy Benchmarking Clearinghouse (KBC) is an organization for implementing an emerging methodology called "consortium benchmarking" in a competitive business environment. The partners in the KBC include NASA Kennedy Space Center and a number of its contractors. Within the KBC, the partners are represented by professionals in quality management and related disciplines.

"Benchmarking," as used here, is a disciplined approach for comparing and measuring your processes against best-in-class organizations (in any industry), identifying the best practices that enable superior performance, and adapting those best practices within your own organization to achieve breakthrough performance improvements. Benchmarking denotes a methodology, based on principles of quality management and process improvement, for developing and using quantitative and qualitative techniques, measures, and criteria for assessing the performances of processes and organizations. This methodology encompasses intra- and/or inter-organizational standardization, as appropriate, to facilitate exchanges and comparisons of performance-assessment information among individuals and organizations, with the ultimate goal of adapting best practices and thereby improving performances.

Consortium benchmarking — benchmarking performed by a group or groups of organizations — is predicated

on collaborative, long-term partnerships for sharing the best and most effective practices of all member organizations and of innovative "best-in-class" outside organizations as well. It offers a less-costly alternative to conventional benchmarking because member organizations share the burden of benchmarking studies. Consortium benchmarking is appropriate when any or all of the following conditions occur:

- Partners have limited resources to devote to benchmarking.
- Partners have minimal experience in performing benchmarking studies.
- Partners share a technological culture and language, so that meaningful comparisons can be made quickly and easily.
- Partners share the same measurement system.
- Partners frequently use similar technologies, processes, and systems.
- Partners are located in proximity.
- Partners meet regularly or at least have already established a forum.

The KBC model for consortium benchmarking (see figure) incorporates a vision, a charter, a two-phase methodology, norms, a reporting structure, and a code of conduct. Within the KBC, processes to be examined in benchmarking studies are selected according to a consensus approach that reflects a multiple-organizational determination of needs, priorities, and objectives. The KBC has provided a foundation for continued benchmarking at Kennedy Space Center through the development of common terminology and techniques. In addition to enhancing benchmarking skills among members, the KBC has strengthened an organizational culture that values continual improvement and teamwork to achieve excellence. This unique model for consortium benchmarking is transferable to other organizations interested in accelerating business changes that can lead to large improvements in the performances of products, processes, and services.

This work was done by Tim Barth of **Kennedy Space Center**; *Cathy L. Horton of NASA Headquarters; Darcel E. Drew of the Boeing Co.; Jeannette J. Eads of EG&G Florida, Inc; Nilgun A. Leavitt of Dynacs Engineering Co., Inc.; Sara C. Morrison of United Space Alliance; and Fred A. Lockhart of Lockheed Martin. Further information is contained in a TSP* *[see page 1]*.

Inquiries concerning rights for the commercial use of this invention should be addressed to the Patent Counsel, Kennedy Space Center; (407) 867-6225. Refer to KSC-11888.

Diagnosing Helicopter Gearboxes Using Connectionist Networks

Concepts of dynamical modeling, fuzzy systems, and neural networks are brought to bear.

Lewis Research Center, Cleveland, Ohio

A method of automated diagnosis of helicopter gearboxes involves processing of selected features of digitized outputs of vibration sensors via structure-based connectionist networks (SBCNs), which are mathematical constructs that incorporate elements from the disciplines of dynamical modeling, fuzzy systems, and neural networks. Like vibration-analysis gear-diagnostic methods that have been reported previously in *NASA Tech Briefs*, the SBCN method offers a partial solution to the basic problem of using pattern-classification techniques to extract indications of specific faulty gearbox components from the outputs of accelerometers mounted at several locations on a gearbox.

In the traditional approach to diagnosis by analysis of vibrations, one relies on a combination of (1) human expertise regarding abnormal features of vibration signals and (2) information on the proximity of each vibration sensor to each component that could be faulty. The traditional approach entails difficulty in processing large numbers of both normal and abnormal signal features and in identifying abnormal features in signals contaminated with noise. The SBCN approach offers greater potential capability for coping with noise and multiple features.

In its graphical representation (see figure), an SBCN is reminiscent of a simple artificial neural network. Vibration signals to be processed in the SBCN are preprocessed via the Single Category-Based Classifier (SCBC) algorithm, which classifies signal features by comparing their values with corresponding values recorded during normal operation in the absence of faults. Some features are flagged on the basis of their degrees of abnormality. The flagged features are fed as inputs to the SBCN.

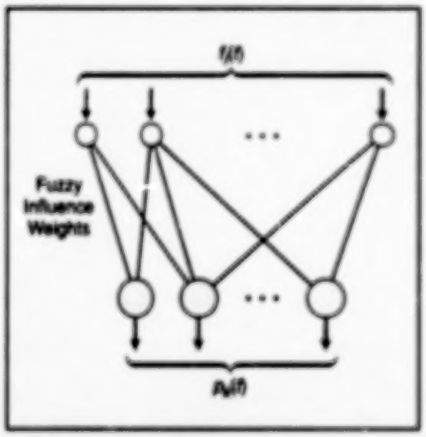

A Structure-Based Connectionist Network resembles a simple artificial neural network, but its connection weights are obtained in a different way.

The flagged features propagate through the SBCN similarly to the way in which they would propagate through a corresponding neural network. The responses of the SBCN are given by

$$p_k(t) = \sum_{i=1}^{n} f_i(t) w_{ik}$$

where $p_k(t)$ is a measure of the time-dependent index that the kth gearbox component is faulty, $f_i(t)$ is a value representative of the time-dependent flagged vibration-signal features from the ith accelerometer, and w_{ik} is a connection weight. As they would in a neural network, the connection weights embody the ranges of flagged feature values associated with various specific faults.

Unlike in a neural network, the connection weights are not established by supervised training on comprehensive sets of measurement data associated with known faults. Instead, each w_{ik} is based on the lower and upper bounds of fuzzy influences between the ith accelerometer and the kth component. The "structure-based" aspect of the SBCN arises as follows: The need for supervised training is eliminated by using knowledge of the dynamics of the gearbox structure to account for the effects of the proximity of the components and the accelerometers on the features of the vibration signals. In principle, this would involve the use of the dynamics to predict the effects of propagation of vibrations through the structure and the resulting attenuation of the

flagged signal features at every frequency of interest. In practice, exact mathematical modeling of the dynamics is impossible; instead, one uses a simplified lumped-mass mathematical model to approximate root-mean-square (rms) attenuation values that are used as average attenuation levels applicable to all frequencies. The rms values are used to assign structural influences, which are then represented by fuzzy variables.

The structural-influence fuzzy variables embody knowledge of the structure only. It is necessary to also assign featural-influence fuzzy variables, which embody knowledge of the effects of component failures on flagged signal features. Inasmuch as vibration-signal features are usually obtained at frequencies related to rotational frequencies of individual components, the effects of component faults on the features can be determined readily and used to calculate the featural-influence fuzzy variables. The structural- and featural-influence fuzzy variables are then incorporated as connection weights in the SBCN.

This work was done by Vinay B. Jammu and Kourosh Danai of The University of Massachusetts and David G. Lewicki of the Propulsion Directorate of the U.S. Army Research Laboratory for **Lewis Research Center**. *Further information is contained in a TSP [see page 1].*

Inquiries concerning rights for the commercial use of this invention should be addressed to NASA Lewis Research Center, Commercial Technology Office, Attn: Tech Brief Patent Status, Mail Stop 7–3, 21000 Brookpark Road, Cleveland, Ohio 44135. Refer to LEW-16453.

Software for Planning in a Hierarchical Processing Environment

Mathematical models predict effects of variations in process parameters.

John F. Kennedy Space Center, Florida

Decision-support software based on discrete-event simulation (DES) has been undergoing development for use in planning and scheduling work in the Orbiter Processing Facility (OPF) at Kennedy Space Center. The software is also suitable for adaptation to similar use in other facilities characterized by low-volume processing and by hierarchical processing environments with multiple subfacilities and with dependencies of tasks on resources and on the prior completion of other tasks.

DES is traditionally applied to mass-production manufacturing environments, where processing volumes are large. DES can enhance decision-support systems by providing the means for mathematical modeling of the effects of uncertainties in parameters. In DES, parameters are treated as being variable with probability distributions; this makes it possible to perform computational simulations to quantify the effects of changes in parameters upon critical outputs, before changing the parameters in a real process or system. In mass-production environments, parameters such as queue lengths and throughput rates are relevant, but in the dynamic processing environment of the OPF, different parameters become relevant.

The developmental software system includes subsystems that implement mathematical models for planning the flow of work at two levels: (1) the OPF task level and (2) the interfacility level. These models have been built by use of commercially available DES software.

The model for the OPF task level is a generic, reusable one that simulates a network of tasks. As each simulated task begins, an attempt to obtain the resources necessary to complete the task is made. If the resources cannot be obtained, the task waits. The output information provided by this model includes the amount of time each task waited for resources, amounts of resources utilized, and the total duration (and variance of duration) of a project.

The model for the interfacility level can also be characterized as a launch-processing-simulation model. This model evaluates the number of launches per year, based on expected process durations and numbers of OPF shifts available. Inasmuch as fixed "milestone" dates are available as inputs, a deviation from a planned launch date can be evaluated in the near term. The model can be used to evaluate workers' overtime needed to meet a planned launch date in the near term and the expected number of launches per year in the long term.

This work was done by JoAnn Lectta of **Kennedy Space Center** *and Robert R. Safford and Matt Archer of the University of Central Florida. Further information is contained in a TSP [see page 1].*

KSC-11936

Model for Investigating Human Factors in an Organization

Contributing causes of mishaps can be analyzed in depth.

John F. Kennedy Space Center, Florida

The Kennedy Space Center Human Factors Event Evaluation Model is a model to facilitate long-term gathering and analysis of data to investigate the effects of human factors on the operations of a complex organization. The model was developed specifically for use in comprehensive human-factors-oriented analysis of events, mishaps, and processes in space-shuttle processing at Kennedy Space Center; it can also be adapted to other organizations that function through interactions of human and equipment subsystems. The main purpose of such analysis is to understand root causes of human errors so as to be able to (1) prevent recurrences of previously observed mishaps and (2) recognize the potential for other mishaps that have not yet been observed and take proactive measures to prevent them.

The present model was developed by extension of a more generic model, called the "Team Effectiveness Leadership Model," the purpose of which was to identify system inputs needed to create high-performance work teams. The present model goes beyond the traditional approach of narrow focus on operators and tasks, providing for more in-depth analysis of causes and effects. Thus, for example, the model makes it possible to investigate the degrees to which such factors as teaming, leadership, and cultural norms could contribute to errors by well-intentioned, well-trained, experienced technicians.

The model serves as a tool to ensure that appropriate questions are asked during investigations of errors, to provide a data base containing standardized rep-

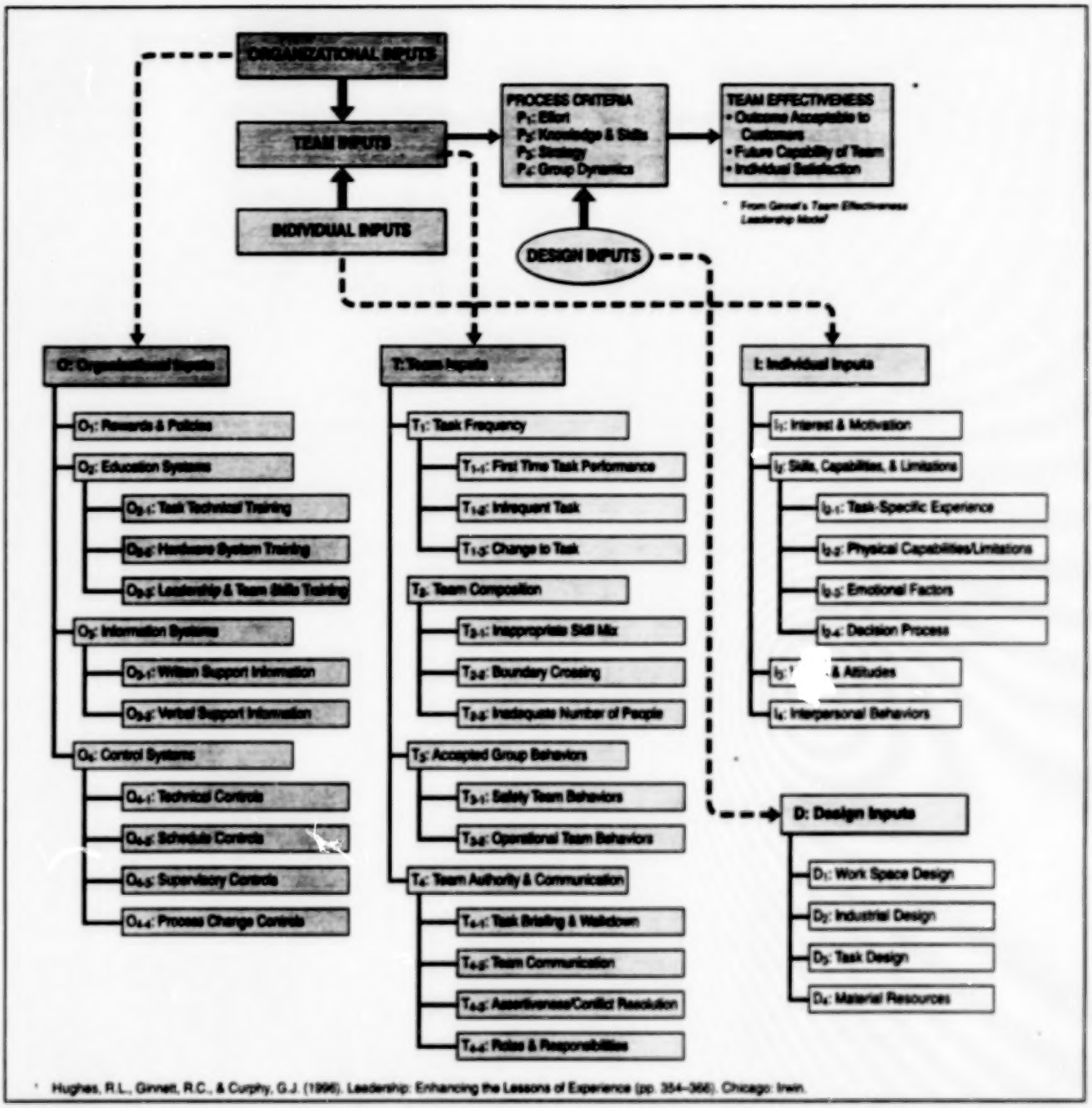

* From Gerrett's *Team Effectiveness Leadership Model*

* Hughes, R.L., Ginnett, R.C., & Curphy, G.J. (1996). Leadership: Enhancing the Lessons of Experience (pp. 354–366). Chicago: Irwin.

The **Kennedy Space Center Human Factors Event Evaluation Model** serves as a tool for acquiring and analyzing data on events that involve human errors.

resentations of events (incidents, mishaps, close calls), and to provide quantitative information as to why errors occur. The questions and the inputs to the model (that is, the answers to the questions) are divided into categories and subcategories. The main categories (see figure) are organizational inputs, team inputs, individual inputs, and design inputs. Subcategories can be added or modified, as needed, to adapt the model to applications other than space-shuttle processing at Kennedy Space Center. To ensure consistency among users, each category is delineated by narrative definitions and examples of probing questions.

Two particularly notable examples of subcategories are those pertaining to written and verbal support information. These subcategories encompass such things as specifications, company directives, and government documentation.

In applying the model to a given event, an investigative team works from top to bottom and from left to right while reviewing each category. If a category is applicable, a cause code and a brief description of the event are entered into a comprehensive data base of events. Once trends have been identified through analysis of multiple events, sources of data can be investigated to review specific problem sources. For example, if there appears to be a tendency for errors to arise in or from the verbal transmission of information, tape recordings of verbal exchanges can be audited in an attempt to identify sources of error.

This work was done by Patrick A. Simpkins, Tim S. Barth, and Jim Medina of **Kennedy Space Center** *and Donna M. Blankmann-Alexander, Mark J. Nappi, and John W. Jamba of United Space Alliance. Further information is contained in a TSP [see page 1].*
KSC-11975

Software for Improving Operational Processes

The Schedule and Cost Risk Analysis Modeling System (SCRAM) computer program identifies important sources of schedule and cost risks in an operational process. The related Process Analysis and Improvement Support System (PASS) program assists in the overall analysis and improvement of an operational process, with emphasis on identifying and eliminating causes of anomalies. SCRAM enables the construction and analysis of realistic mathematical models of schedule variables (e.g., durations of tasks) and of constraints imposed by limitations on resources. SCRAM utilizes input information in the form of historical delay data and schedule information for a process in question to derive measures of importance of classes of delays. PASS includes (1) a process-analysis module, which performs schedule and cost analyses of delays, using criticalities defined by the analyst instead of resource constraints, to identify the most important kinds of anomalies; (2) a root-cause module, which provides for quantitative and qualitative analyses of causes of anomalies; and (3) a process-improvement-evaluation module, in which the language of representation of cause-and-effect relationships from the root-cause module is used in accounting for process-improvement alternatives and criteria for making decisions.

This work was done by Robert Fung and Max Henrion of Lumina Decision Systems for **Kennedy Space Center**. *No further documentation is available.*

In accordance with Public Law 96-517, the contractor has elected to retain title to this invention. Inquiries concerning rights for its commercial use should be addressed to

Max Henrion
Lumina Decision Systems
59 North Santa Cruz Ave.
Suite Q
Los Gatos, CA 95030

Refer to KSC-11914/15, volume and number of this NASA Tech Briefs issue, and the page number.

Work-Measurement and Methods-Analysis Studies of the OPF

Two reports describe early phases of continuing studies directed toward the selection and adaptation of industrial work-measurement and methods-analysis procedures for application to the Orbiter Processing Facility (OPF) at Kennedy Space Center. These studies were prompted by a need to increase efficiency, effectiveness, and productivity in the face of budget reductions. In the work-measurement study, (1) candidate work-measurement techniques were selected on the basis of feasibility, (2) similar space-shuttle-processing tasks were grouped into clusters, (3) the candidate techniques were used to measure the times of tasks in the clusters, then (4) the technique that scored highest according to weighted quantitative criteria developed for each cluster was selected as the "best" technique for the cluster. The methods-analysis study included an ergonomic review of tools, direct observation of tasks, and examination of work instructions. Several areas for improvements in work methods were identified. A methodology for selecting cost-effective methods-analysis techniques in the OPF environment was developed.

This work was done by Amanda Mitskevich and Tim S. Barth of **Kennedy Space Center**; *Robert R. Safford, Julia Pet-Edwards, William Swart, and Kay Stanney of the University of Central Florida; and Susan Murray of Texas A&M University. To obtain copies of the reports, "A Procedure for Adaptation of Work Measurement Procedures To The Space Shuttle Ground Processing Environment" and "A Procedure for Adaptation of Industrial Methods Analysis Procedures To Space Shuttle Ground Processing At The Kennedy Space Center" see TSP's [page 1].*
KSC-11934/35

BLANK PAGE

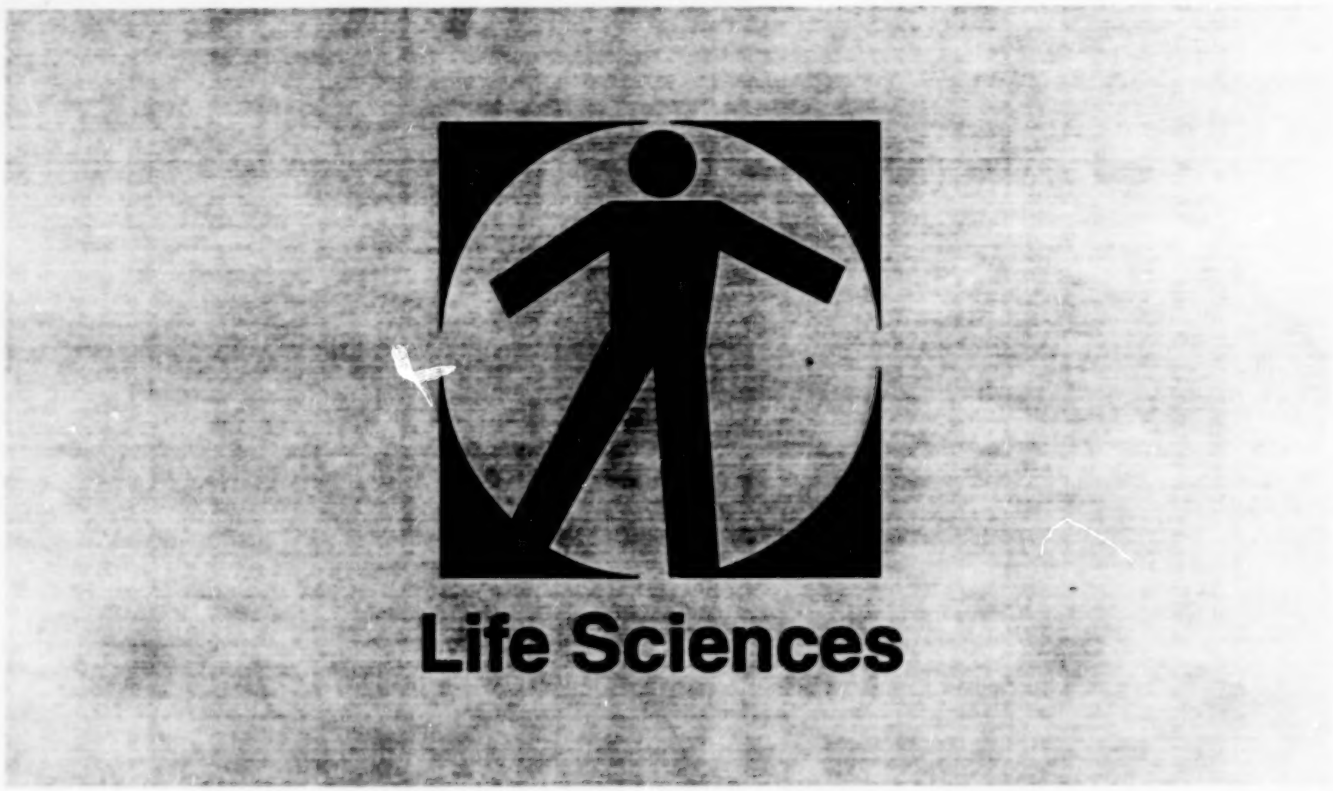

Hardware, Techniques, and Processes

61 Compact, Noncontact Fiber-Optic Probe for Diagnosis of Eye Diseases

BLANK PAGE

Compact, Noncontact Fiber-Optic Probe for Diagnosis of Eye Diseases

Probes like this one offer great potential for research and diagnosis.

Lewis Research Center, Cleveland, Ohio

A compact fiber-optic probe has been found to be useful for noncontact diagnosis of interior parts of eyes. The probe was originally developed for performing dynamic-light-scattering measurements to determine transport properties of submicron particles suspended in fluids in microgravity, and is an improved version of the probes described in "Dynamic Light Scattering With Improved Fiber-Optic Probes (LEW-15461)" *NASA Tech Briefs*, Vol. 19, No. 9 (September 1995), page 86.

The probe (see figure) includes a probe head that holds two monomode optical fibers, of which one carries light with a power of a few microwatts from a laser diode to illuminate the region to be probed. The other optical fiber carries light scattered from the probed region to an avalanche photodiode (APD) for detection. The tips of the optical fibers in the probe head are aligned with an off-axis gradient-index-of-refraction (GRIN) lens, which is positioned with a gap of up to 0.5 mm from the fiber tips to obtain a tightly focused spot in the probed region.

In operation, the probe is positioned in front of an eye to illuminate the interior and measure light back-scattered from submicron particles in the interior. Because of Brownian motion of the particles, the back-scattered light forms a rapidly changing interference pattern (dynamic light scattering) that manifests itself as fluctuations in the output of the APD. Information about the sizes of particles and other aspects of the dynamics of the scattering medium can be extracted by processing the output of the APD through an amplifier/discriminator and a digital correlator to obtain a correlation function.

The correlation function gives information about the particles in the scattering volume. This information is useful for research and diagnosis of eye diseases and other diseases with ocular manifestations. For example:

- Cholesterol and blood-sugar molecules occur in the aqueous humors of patients with heart-related diseases and diabetes, respectively.
- Protein crystallines and possibly other particles in the lens have been conjectured to play a role in cataractogenesis. Research is needed to establish the exact causes of cataracts and to develop techniques for early diagnosis and treatment.
- Changes in macromolecules in the vitreous humor can be used to identify diseases of the posterior chamber of the eye and complications of those diseases; e.g., posterior vitreous detachment and diabetic retinopathy.

Thus, further development along this line holds promise for compact fiber-optic probes as clinical ophthalmic instruments for routine use.

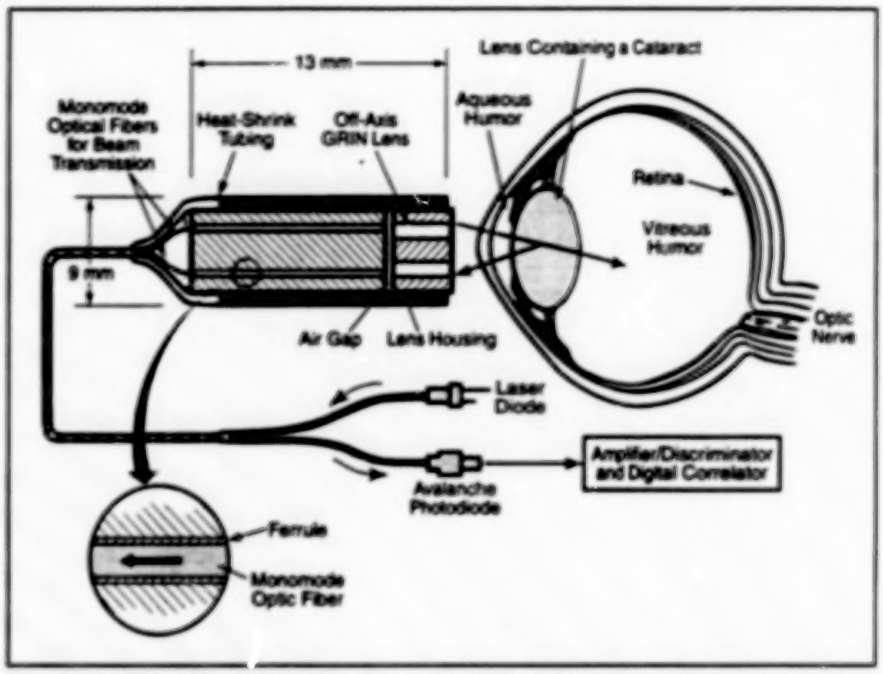

The Probe Makes No Contact with the eye. Dynamic light-scattering measurements taken with the probe yield information on submicron particles inside the eye.

This work was done by Rafat R. Ansari and Kwang I. Suh of **Lewis Research Center**. *Further information is contained in a TSP [see page 1].*

Inquiries concerning rights for the commercial use of this invention should be addressed to NASA Lewis Research Center, Commercial Technology Office, Attn: Tech Brief Patent Status, Mail Stop 7-3, 21000 Brookpark Road, Cleveland, Ohio 44135. Refer to LEW-16429.

National Aeronautics and
Space Administration

END

10\08\98